AFOSR-TR-95

G613

REPORT DOCUMENTATION PAGE

1. AGENCY USE ONLY (Leave blank)	2. REPORT DATE	3. REPORT TYPE AND DATES COVERED
	October 1, 1994	Annual Technical 9/01/94 - 8/31/94

4. TITLE AND SUBTITLE

(U) Reaction Zone Models for Vortex Simulation of Turbulent Combustion

5. FUNDING NUMBERS

PE - 61102F
PR - 2308
SA - BS
G - F49620-92-J-0445

6. AUTHOR(S)

Ahmed F. Ghoniem

7. PERFORMING ORGANIZATION NAME(S) AND ADDRESS(ES)

Massachusetts Institute of Technology
77 Massachusetts Avenue
Cambridge, MA 02139

8. PERFORMING ORGANIZATION REPORT NUMBER

DTIC SELECTED OCT.03 1995 B

9. SPONSORING/MONITORING AGENCY NAME(S) AND ADDRESS(ES)

AFOSR/NA
110 Duncan Avenue, Suite B115
Bolling AFB DC 20332-0001

10. SPONSORING/MONITORING AGENCY REPORT NUMBER

19951002 028

11. SUPPLEMENTARY NOTES

12a. DISTRIBUTION/AVAILABILITY STATEMENT

Approved for public release; distribution is
unlimited

12b. DISTRIBUTION CODE

13. ABSTRACT (Maximum 200 words)

During the course of the second year, we pursued the development of a reaction zone model which can be used in the numerical simulation of turbulent combustion. We focused our attention on the high Reynolds number, high Damkohler number case in which the reaction zone thickness is much smaller than the thickness of the small scales of turbulence. Furthermore, we treated the case in which the entire flame thickness, including both the convection-diffusion zone and the reaction zone, is smaller or equal to the small scale of turbulence. Accordingly, we developed on unsteady strained, multistep chemistry and diffusion thin flame model which is based on the fundamental equations governing the convection-diffusion-reaction balance within the flame structure, while assuming that the strain rate remains constant within the flame. Moreover, we compared the results of a computation of an exothermic, finite rate kinetics model of a reacting shear layer with those obtained using an infinite rate kinetics case. This comparison established the fact that the impact of heat release on the flow, mixing and dynamics can be obtained using a thin flame model. In the coming year, we will focus on linking the thin flame, finite rate chemistry model to the flow simulation code and develop the proper set of boundary conditions of the flame model in order to expand its regime of applicability.

14. SUBJECT TERMS

Turbulent Combustion, Numerical Simulation, Vortex Methods, Combustion Models.

15. NUMBER OF PAGES

96

16. PRICE CODE

17. SECURITY CLASSIFICATION OF REPORT	18. SECURITY CLASSIFICATION OF THIS PAGE	19. SECURITY CLASSIFICATION OF ABSTRACT	20. LIMITATION OF ABSTRACT
Unclassified	Unclassified	Unclassified	UL

SECOND ANNUAL TECHNICAL PROGRESS REPORT
ON

REACTION ZONE MODELS FOR VORTEX SIMULATION
OF TURBULENT COMBUSTION

(AFOSR Grant # F49620-92-J-0445DEF)

Principal Investigator: Ahmed F. Ghoniem

Department of Mechanical Engineering
Massachusetts Institute of Technology
Cambridge, MA 02139

SUMMARY

During the course of the second year, we pursued the development of a reaction zone model which can be used in the numerical simulation of turbulent combustion. We focused our attention on the high Reynolds number, high Damkohler number case in which the reaction zone thickness is much smaller than the thickness of the small scales of turbulence. Furthermore, we treated the case in which the entire flame thickness, including both the convection-diffusion zone and the reaction zone, is smaller or equal to the small scale of turbulence. Accordingly, we developed an unsteady strained, multistep chemistry and diffusion thin flame model which is based on the fundamental equations governing the convection-diffusion-reaction balance within the flame structure, while assuming that the strain rate remains constant within the flame. Moreover, we compared the results of a computation of an exothermic, finite rate kinetics model of a reacting shear layer with those obtained using an infinite rate kinetics case. This comparison established the fact that the impact of heat release on the flow, mixing and dynamics can be obtained using a thin flame model. In the coming year, we will focus on linking the thin flame, finite rate chemistry model to the flow simulation code and develop the proper set of boundary conditions of the flame model in order to expand its regime of applicability.

1

I. OBJECTIVES

The objectives of this work are:

(1) To develop a computational framework for the simulation of turbulent combustion phenomena by deriving equations which govern the flow and combustion in different, physically-distinct regions in the domain. This formulation is independent of the numerical method, or methods, used to integrate these equations and hence will have applications beyond vortex simulations;

(2) To develop fundamentally based flame structure models using the equations obtained in (1) where flow-combustion interactions are represented by the effect of the time-dependent strain rate exerted by the outer flow on the flame structure. One important aspect of these models will be the incorporation of multistep chemical kinetics algorithms to accurately capture flow combustion interactions when it is dominated by radical concentration and diffusion;

(3) To develop subscale fundamentally based models which can be used to obtain large eddy simulations using vortex methods. Subscale models, in this case, will be obtained through the application of the renormalization group theory to the equations governing vorticity stretching and tilting on scales lower than numerically resolvable scales. The application of RNG in physical vorticity space is motivated by our solutions which show that the properties of vortex lines at the small scales follow closely the RNG predictions.

(4) To modify the transport element method; a Lagrangian scheme which we developed to simulate reacting species transport, to act as a "coupling" algorithm between the solutions obtained for the outer flow and the inner flow.

The developed methodology will be applied to study mixing and combustion in reacting shear flow at high Reynolds numbers. Effect of strong density variations, high heat release rates at elevated Damkohler numbers, and high Mach numbers will also be investigated.

II.   PERSONNEL

During the period of 1993-1994, funding was used to support the work of the following students:

(1)   Marios Soteriou, partially supported by funds from this contract as a post doctor.

(2)   Van Luu, a Ph.D. student working on distributed reaction zone combustion model.

(3)   Constantin Petrov , a Ph.D. student working on the thin flame detailed chemistry and diffusion combustion model.

III.   <u>WORK STATUS</u>

Overview:

The objectives of this program are to develop a reaction zone model, or several reaction zone models applicable under different turbulent combustion interaction regimes, and implement one or several of these models within a framework which is aimed at the accurate and efficient simulation of turbulent combustion. Since most often, the results of these simulations are intended to predict the volumetric burning rate, combustion stability, and emission of minor species (NO_x, CO and HC), it is important that the simulation includes a representation of the detailed fluid dynamics and mixing, the dynamic impact of heat release on the flow dynamics, and most significantly the detailed chemical kinetics and transport models necessary to evaluate the rate of reaction and the concentration of minor species. The plan of our research has thus been organized around addressing these issues in detail.

The flow simulation approach has been developed and tested before. We have demonstrated that using vortex methods, we can capture the large and small scale structures of a turbulent flow (at least in an unconfined shear flow environment). The development of a reaction zone model for high Reynolds number, high Damkohler number turbulent combustion is described in detail in Section III.I and Appendix 1. The model is based on the notion that in this regime, the entire flame structure thickness is less than or equal to the small scales of turbulence and thus the impact of turbulence on the combustion process can be expressed in terms of an

3

unsteady strain rate acting on the plane of the flame. This model, while treating a single flame, is capable of accounting for the interaction between neighboring flames as well. The model has been expanded to allow the implementation of a detailed chemical kinetics mechanism and the differential diffusion of heat and different species.

In the coming year, we will focus on the implementation of this model into the vortex simulation of the reacting shear layer. In preparation for this step, we performed a comparison between a vortex simulation of the same flow using direct simulation of the combustion process, i.e., without imposing any assumptions on the flame structure or its interactions with the flow, and a simulation in which the chemistry was assuming to occur infinitely fast. The comparison showed that while the thin flame model simplifies the computations significantly, it is still capable of capturing the essential dynamics of heat release and how it affects the flow and mixing. The comparison between the results describing shear layer dynamics using a thin flame model and those using direct simulation of the flame structure are described in Sections III.2 and III.3.1 and in more detail in Appendices II and III. Finally, a detailed analysis of the vorticity dynamics of a reacting shear layer with high rates of heat release and finite rate, although fast kinetics, is presented in Sections III.3 and Appendix III.

III.1   Development of an Unsteady Strained, Complex Chemistry and Transport Flame Model
         for Turbulent Combustion Simulation

We have developed an unsteady strained flame model with detailed chemical kinetics and molecular transport. The model can be used independently to study the response of a flame to external unsteady flows or as a combustion submodel in a turbulent combustion simulation. As a model of the reaction zone structure in a turbulent combustion simulation, it is applicable under conditions of high Reynolds number and high Damkohler number where the combined convection-diffusion and reaction zones is smaller than or equal to the small scales of the flows. This is the regime that has commonly been known as the flamelet regime. Our approach differs from the classical flamelet regime in two significant aspects:

(1)   we treat the problem as being unsteady since it has been shown that the flame response to a time dependent strain is most instantaneous; and,

(2)   the coupling between the flow and the flame structure is described in terms of the boundary conditions imposed by the flow across the flame thickness as well as the strain, i.e., we do not consider the flame as a reaction zone in a simple stagnation point flow.

As described in detail in Appendix I, the formulation of the model is based on the unsteady strained laminar flame equations, while maintaining the strain rate constant throughout the flame structure. Following a series of mathematical transformations, the equations governing the flame structure are reduced to a set of reaction-diffusion equations which are much easier to integrate than the original equations using a distribution of points that adapt to the time dependent flame structures. The model accommodates an arbitrary chemical kinetic algorithm using an interface similar to that adopted in CHEMKIN. Results show that the model predictions agree very well with those obtained from the detailed solution of the strained flame equations, while taking a small fraction of the computer time.

During the coming year we will work on coupling this model with the flow simulation code, develop the proper boundary conditions and interface tracking algorithms necessary to ensure the coupling, and use this approach to simulate turbulent combustion in a shear layer.

III.2   Effect of Exothermicity and Forcing on the Dynamics of Reacting Shear Flow: Infinite Chemistry Case

In this work, the effects of combustion heat release on a spatially-developing, high Reynolds number, non-premixed, reacting shear-layer have been investigated under both forced and unforced inlet conditions using the results of two-dimensional numerical simulations. In this work, combustion is modeled using an infinite reaction speed model. The numerical solution is obtained using the Lagrangian transport-element method. Results indicate that in an unforced flow, heat release decreases the size of the mixing region and the amount of product formed over most of the domain via: (i) a delay of the onset of the flow instability and (ii) a reduction in the overall spinning and an apparent suppression of the interactions of the eddies. With external forcing, which promotes early

5

destabilization of the layer, similar trends of mixing and combustion reduction are experienced, as manifested by reduced eddy spinning, which keeps the eddy major axis aligned with the flow direction, and alteration of the eddy pairing interaction to tearing of smaller eddies by their larger neighbors. Volumetric (area) expansion weakens the vorticity field and is responsible for delaying the onset of the instability in the unforced case, the reduction of the spinning of the eddies in both cases and the alignment of the major axis of the downstream larger eddy with the flow direction in the forced case. The suppression of eddy pairing is attributed to the presence of baroclinic vorticity generation. These results were confirmed by a simulation in which the infinite chemistry assumption was relaxed and it has been established, as a result, that the dynamic effects of heat release can be captured using a thin flame model (see Section III.3 and Appendix III). The detail of this work are described in Appendix II.

III.3 Vorticity Dynamics of a Reacting Shear Layer with Finite Rate Kinetics

The effects of combustion on the vorticity dynamics of a low-Mach number, forced, spatially-developing, high Reynolds number, reacting-shear layer have been investigated using the results of a two-dimensional simulation. Here the chemical reaction is modeled by single-step, irreversible, Arrhenius kinetics with high Damkohler number, moderate Karlovitz number and significant heat release. The numerical solution is obtained using the Lagrangian transport-element method. Results indicate that a fast exothermic reaction, with the concomitant density variation, modifies the shape, size, speed and orientation of the large-scale vortical structures and their downstream interactions, leading to an overall reduction of the cross-stream growth of the mixing region. These changes are traced to the two primary mechanisms by which density variation due to heat release modifies vorticity: volumetric expansion and baroclinic generation. It is shown that the weakening of the vorticity due to volumetric expansion diminishes the cross-stream mixing zone by aligning the eddy major axis with the flow direction. Baroclinic vorticity generation, on the other hand, is responsible for the formation of a band of positive vorticity on the outer perimeter of the large eddies, whose vorticity is predominantly negative, which inhibits entrainment and alters the eddy interaction mechanism from pairing of adjacent eddies to tearing of smaller eddies by their larger neighbors.

Both mechanisms contribute to the acceleration of the eddies in the streamwise direction. The detail of this study are described in Appendix III.

IV. PUBLICATIONS DURING 1993-1994.

1. Soteriou, M.C. and Ghoniem, A.F., "Numerical Study of Exothermic Combustion in a Mixing Layer Using Finite and Infinite Reaction Rate Models, *14th ICDERS*, Coimbra, Portugal, 1993, submitted for publication in *Combustion Science and Technology*.

2. Soteriou, M.C. and Ghoniem, A.F., "Vortex-Transport Element Simulation of the Exothermically Reacting Spacially Developing Shear Layer," *Second U.S. National Congress on Computational Mechanics,* Washington, D.C., August 1993, submitted for publication in *Dynamics of Exothermicity*, ed. Ray Brown, Gordon and Breach.

3. Petrov, C. and Ghoniem, A. F., "Unsteady Thin Flames as Models of Turbulence-Combustion Interactions," presented at the AIAA *32nd Aerospace Sciences Meeting*, Reno, NV, January 1994, AIAA-94-0776, submitted for publication in *Combustion and Flame*.

4. Soteriou, M.C. and Ghoniem, A.F., "Dynamics of Reacting Shear Flows; Effects of Exothermicity and Forcing," presented at the AIAA *32nd Aerospace Sciences Meeting*, Reno, NV, January 1994, AIAA-94-0777, submitted for publication at *AIAA Journal*.

5. Soteriou, M.C. and Ghoniem, A.F., "The Vorticity Dynamics of an Exothermic, spatially-developing Forced, Reacting Shear-Layer," presented at the *25th International Symposium* on Combustion, University of California, Irvine, CA, 1994, to appear in the Symposium Proceedings.

V.   SEMINARS AND LECTURES DELIVERED DURING 1992-1993

1.   Johns Hopkins, Baltimore, MD, 1994

2.   Ford Motor Company, Dearborn, MI, 1994

3.   General Electric Aircraft Engine, Cincinnati, OH, 1994.

VI.   INTERACTIONS WITH INDUSTRIAL AND GOVERNMENT LABORATORIES DURING 1992-1993.

1.   General Electric Corporate Research and Development Center, with Dr. Sanjay Correa and Dr. Hukam Mongia.

2.   Altex Technologies, Los Gatos (small R&D Business), with Drs. M. Namazian and J. Kelly.

3.   Ford Motor Company, with Dr. Chris Kent and Dr. Gary Strumulo

4.   Aerodyne Research, Inc., with Dr. David Stickler.

APPENDIX I

REPORT

Development of an Unsteady Strained Flame Model with Multi-Step Chemical Kinetics Mechanism

Constantin A. Petrov
Reacting Gas Dynamics Computational Lab
Massachusetts Institute of Technology

CONTENTS

NOMENCLATURE

ρ - the mixture density,

$\vec{v} = (u, v)$ - the total velocity of fluid,

$\vec{V} = (U, V)$ - the inviscid irrotational velocity component,

$\vec{v_c} = (u_c, v_c)$:- the combustion generated velocity,

Y_k - the mass fraction of species k,

X_k - the mole fraction of species k,

$[X_k]$ - the molar concentration of species k,

D_k -the mixture averaged diffusion coefficient of species k,

$\dot{\omega}_k$ - the production rate of species k,

W_k - the molecular weight of species k,

c_p - the constant pressure specific heat of mixture, mass units,

$c_{p, k}$ - the constant pressure specific heat of species k, mass units,

$K+1$ -the total number of chemical species,

T - the thermodynamic temperature,

p - the pressure,

λ - the thermal conductivity of mixture,

R_u - the universal gas constant,

W_{mix} - the molecular weight of mixture,

H_k - the enthalpy of species p, molar units,

V_k - the diffusion velocity,

V_{cor} - the correction velocity,

$k_{T, k}$ - the thermal diffusion coefficient of species k,

(x, y, t) - physical coordinates,

$(\tilde{y}, \tilde{t})$ - coordinates of the first transformed domain,

$(\xi, \bar{\tau})$ - computational coordinates,

$\varepsilon(t)$ - the strain rate,

$L_{e, k}$ - the Lewis number of species k,

α - the thermal diffusivity of mixture,

A_i - the pre-exponential constant of reaction i,

$E_{a, i}$ - the activation energy of reaction i,

β_i - the temperature exponent of reaction i,

$\dot{q}_i$ - the rate-of-progress variable of reaction i,

$k_{f, i}, k_{r, i}$ -the forward and reverse constants of reaction i,

$K_{c, i}$ - the equilibrium constant of reaction i, concentration units,

2

θ- the non-dimensional temperature,

α_{ki} - third-body coefficient of species k in reaction i,

v'_{ki} - the stoichiometric coefficient of species k in reaction i

p_{atm}- the pressure of one atmosphere,

SUBSCRIPTS

u- unburnt mixture,

b- burnt mixture,

scl- scale value,

*- reference value,

k- species number,

i- chemical reaction number,

n- time layer number,

mix- mixture.

1.1 Formulation

The flow configuration of the model is depicted in figure 1. The flame is located in the stagnation point flow produced by two counter-flowing planar jets of reactants and products. The x- and y-axes are directed parallel and perpendicular to the flame, respectively. The flame is, in general, unsteady, i.e. its location and burning velocity change with time. The objectives of the present model are to investigate the transient dynamics of the flame in response to sudden and periodic changes in the strain rate, and to develop a combustion submodel for high Damkohler number turbulent combustion simulation.

Applying the boundary layer approximation, in which diffusion along the boundary layer, taken here to be the x-axis, is negligibly small, we can write the equations governing the dynamics of flame as follows:

$$\frac{\partial \rho}{\partial t} + \frac{\partial (\rho u)}{\partial x} + \frac{\partial (\rho v)}{\partial y} = 0 ,\tag{1.1}$$

$$\rho \frac{\partial Y_k}{\partial t} + \rho u \frac{\partial Y_k}{\partial x} + \rho v \frac{\partial Y_k}{\partial y} = - \frac{\partial}{\partial y}(\rho Y_k V_k) + \dot{\omega}_k W_k, \text{ for } k = 0, K \tag{1.2}$$

$$\rho c_p \left(\frac{\partial T}{\partial t} + u \frac{\partial T}{\partial x} + v \frac{\partial T}{\partial y} \right) = \frac{\partial}{\partial y}\left(\lambda \frac{\partial T}{\partial y} \right) - \sum_{k=0}^{K} \rho Y_k V_k c_{p,k} \frac{\partial T}{\partial y} - \sum_{k=0}^{K} \dot{\omega}_k H_k , \tag{1.3}$$

$$p = \rho \frac{R_u}{W_{mix}} T , \tag{1.4}$$

$$\rho \frac{\partial u}{\partial t} + \rho u \frac{\partial u}{\partial x} + \rho v \frac{\partial u}{\partial y} = - \frac{\partial p}{\partial x}, \tag{1.5}$$

where ρ is the mixture density; u and v are the velocities of fluid in the x and y directions, respectively; Y_k is the mass fraction of species k; D_k is the mixture averaged diffusion coefficient of species k; $\dot{\omega}_k$ is the production rate of species k; W_k is the molecular weight of species k; c_p and $c_{p,k}$ are the constant pressure specific heats of mixture and species k; (K+1) is the total number of chemical species; T and p are the thermodynamic temperature and pressure, respectively; λ is the thermal conductivity of the mixture; R_u is the universal gas constant; W_{mix} is the molecular weight of the

mixture; H_k is the enthalpy of species k in molar units; and the diffusion velocity V_k is defined as follows:

$$V_k = - \frac{D_k}{X_k} \frac{\partial X_k}{\partial y} + V_{cor} + \frac{D_k k_{T,k}}{X_k} \frac{1}{T} \frac{\partial T}{\partial y} , \; for \; k = 0, K \qquad (1.5)$$

where V_{cor} is the correction velocity introduced in order to satisfy the identity $\sum_{k=0}^{K} Y_k V_k = 0$; $k_{T, k}$ is the thermal diffusion coefficient. In the following, we neglect the thermal diffusion velocity (the last term of (1.5)) and the correction velocity. As it was shown in [2], this simplification does not significantly affect the results. In the above equations, we neglected the diffusion terms in the x-momentum equation, the heat diffusion terms in the heat and mass transport equations, and the dissipation term in the energy equation.

Along the stagnation streamline $x = 0$, and due to symmetry :

$$u = 0 \; , \; \frac{\partial}{\partial x} = 0.$$

leading to the following simplifications of equations (1.1-5):

$$\frac{\partial \rho}{\partial t} + \rho \; \frac{\partial u}{\partial x} + \frac{\partial (\rho v)}{\partial y} = 0 \qquad (1.6)$$

$$\rho \; \frac{\partial Y_k}{\partial t} + \rho v \; \frac{\partial Y_k}{\partial y} = \frac{\partial}{\partial y} \left(\frac{\rho D_k}{W_{mix}} \frac{\partial (W_{mix} Y_k)}{\partial y} \right) + \dot{\omega}_k W_k, k = 0, K \quad (1.7)$$

$$\rho \, c_p \frac{\partial T}{\partial t} + \rho \, c_p v \; \frac{\partial T}{\partial y} = \frac{\partial}{\partial y} \left(\lambda \frac{\partial T}{\partial y} \right) - \sum_{k=0}^{K} \rho Y_k V_k c_{p,k} \; \frac{\partial T}{\partial y} - \sum_{k=0}^{K} \dot{\omega}_k H_k \quad (1.8)$$

$$p = \rho \; \frac{R_u}{W_{mix}} T \qquad (1.9)$$

while x-momentum equation (1.5) is identically equal to zero. The boundary conditions for equations (1.6-8) are:

$$y = -\infty : \; Y_k = Y_{k,b} , \; T = T_b , \; \partial T / \partial y = 0 \qquad (1.10)$$

$$y = +\infty : \; Y_k = Y_{k,u} , \; T = T_u \qquad (1.11)$$

5

where the subscripts u and b denote the values on the unburnt and burnt side, respectively. The boundary conditions for the velocity field will be discussed later. Although along the stagnation streamline $u = 0$, the $\frac{\partial u}{\partial x}$ term of equation (1.6) does not vanish. Since the boundary conditions for Y_k and T are independent of x, it can be demonstrated [1] that the flame structure near the stagnation streamline is similar to that described by equations (1.6-9). Thus, the simplified system of equations (1.6-9) is able to predict the structure of the flame in the vicinity of the stagnation streamline. One more simplification of the problem can be made. The energy equation (1.8) contains a term of the form

$$\sum_{k=0}^{K} \rho Y_k V_k c_{p,k} \, \frac{\partial T}{\partial y}.$$

Smooke [2] showed that this term can be safely neglected virtually for all important configurations of strained and unstrained flame. Eliminating this term, we can rewrite equation (1.11) as follows:

$$\rho \, c_p \, (\frac{\partial T}{\partial t} + v \, \frac{\partial T}{\partial y}) = \frac{\partial}{\partial y} \left(\lambda \, \frac{\partial T}{\partial y} \right) - \sum_{k=0}^{K} \dot{\omega}_k H_k \tag{1.12}$$

In this study we solve the system of equations (1.6-12) with boundary conditions (1.10-11). First, we decompose the velocity field into two components: (1) $\vec{V} = (U, V)$, and (2) $\vec{v_c} = (u_c, v_c)$:

$$\vec{v} = \vec{V} + \vec{v_c} \tag{1.13}$$

where $\vec{v}$ is the total velocity, $\vec{v_c}$ is the combustion generated velocity, and $\vec{V}$ is the externally imposed velocity which satisfies the following incompressible continuity equation:

$$\frac{\partial U}{\partial x} + \frac{\partial V}{\partial y} = 0 \tag{1.14}$$

The idea behind this decomposition is as follows. Any vector $\vec{v}$ can be represented as a sum of two vectors. The vector $\vec{V}$ provides the velocity field far away from the flame. The vector $\vec{v_c}$ accounts for the change in velocity induced by the variation in density

6

within the reaction zone. It should be noted that, in contrast to seemingly similar models, our model does not employ the decomposition of the velocity field into a mean and a disturbance components since, in the reaction zone, both velocity components might be of the same order of magnitude. Nowhere in the model is the assumption $|\vec{V}| >> |\vec{v_c}|$ used. Substituting equation (1.13) into continuity equation (1.6), we obtain:

$$\frac{\partial \rho}{\partial t} + \rho \frac{\partial U}{\partial x} + \rho \frac{\partial u_c}{\partial x} + \rho \frac{\partial V}{\partial y} + \rho \frac{\partial v_c}{\partial y} + (V + v_c) \frac{\partial \rho}{\partial y} = 0 \tag{1.15}$$

Using equation (1.14) and assuming that on the stagnation streamline $\partial u_c / \partial x = 0$, we get:

$$\frac{\partial \rho}{\partial t} + \frac{\partial (\rho v_c)}{\partial y} + V \frac{\partial \rho}{\partial y} = 0 \tag{1.16}$$

Substitution the velocity decomposition in equation (1.13) into equations (1.7) and (1.12) yields:

$$\rho \frac{\partial Y_k}{\partial t} + \rho (V + v_c) \frac{\partial Y_k}{\partial y} = \frac{\partial}{\partial y} \left(\frac{\rho D_k}{W_{mix}} \frac{\partial (W_{mix} Y_k)}{\partial y} \right) + \dot{\omega}_k W_k, k = 0, K \tag{1.17}$$

$$\rho c_p \frac{\partial T}{\partial t} + \rho c_p (V + v_c) \frac{\partial T}{\partial y} = \frac{\partial}{\partial y} \left(\lambda \frac{\partial T}{\partial y} \right) - \sum_{k=0}^{K} \dot{\omega}_k H_k \tag{1.18}$$

The purpose of the introduction of the velocity decomposition is to apply a number of transformations which can substantially simplify the solution of equations (1.17-18). If the externally imposed inviscid irrotational velocity field $\vec{V}$ is specified as

$$\vec{V} = (\varepsilon (t) x, -\varepsilon (t) y) \tag{1.19}$$

where ε is the strain rate, then the following transformation [3]

$$\tilde{y} = exp \left(\int_0^t \varepsilon(t') \, dt' \right) y \equiv B(t) y, \quad \tilde{t} = t \tag{1.20}$$

eliminates the $V \partial / \partial y$ operators from equations (1.16-18). The physical idea behind this transformation is to translate the system of equations into a reference frame locally moving with the velocity induced by the constant density stagnation point flow $\vec{V}$. The part of the convective operator related to this velocity component is naturally eliminated

7

in this reference frame. Consider the following operator $\partial/\partial t + V \partial/\partial y$ in equations (1.16-18). Using the chain rule of differentiation and equations (1.20), we get:

$$\frac{\partial}{\partial y} = \frac{\partial \tilde{y}}{\partial y} \frac{\partial}{\partial \tilde{y}} + \frac{\partial \tilde{t}}{\partial y} \frac{\partial}{\partial \tilde{t}} = B(t) \frac{\partial}{\partial \tilde{y}}$$

$$\frac{\partial}{\partial t} = \frac{\partial \tilde{y}}{\partial t} \frac{\partial}{\partial \tilde{y}} + \frac{\partial \tilde{t}}{\partial t} \frac{\partial}{\partial \tilde{t}} = \varepsilon B(t) y \frac{\partial}{\partial \tilde{y}} + \frac{\partial}{\partial \tilde{t}}$$

Taking these equations into account, the operator in the $(\tilde{y}, \tilde{t})$ domain can be written as:

$$\partial/\partial t + V \partial/\partial y = \varepsilon B(t) y \frac{\partial}{\partial \tilde{y}} + \frac{\partial}{\partial \tilde{t}} + (-\varepsilon y) B(t) \frac{\partial}{\partial \tilde{y}} = \frac{\partial}{\partial \tilde{t}}$$

Here we used expression (1.19) for the externally imposed constant density velocity field $\vec{V}$. Following the application of the transformation in equation (1.20), the governing equations take the form:

$$\frac{\partial \rho}{\partial \tilde{t}} + B \frac{\partial (\rho v_c)}{\partial \tilde{y}} = 0, \tag{1.21}$$

$$\rho \frac{\partial Y_k}{\partial \tilde{t}} + \rho v_c B \frac{\partial Y_k}{\partial \tilde{y}} = B^2 \frac{\partial}{\partial \tilde{y}} \left(\frac{\rho D_k}{W_{mix}} \frac{\partial (W_{mix} Y_k)}{\partial \tilde{y}} \right) + \dot{\omega}_k W_k, k = 0, K \tag{1.22}$$

$$\rho c_p \frac{\partial T}{\partial \tilde{t}} + \rho c_p v_c B \frac{\partial T}{\partial \tilde{y}} = B^2 \frac{\partial}{\partial \tilde{y}} \left(\lambda \frac{\partial T}{\partial \tilde{y}} \right) - \sum_{k=0}^{K} \dot{\omega}_k H_k \tag{1.23}$$

The combustion generated velocity $\vec{v_c}$ is eliminated by applying another (Howarth) transformation to equations (1.21-23):

$$\xi = \int_0^{\tilde{y}} \bar{\rho} \, d\tilde{y}' \ , \quad \tau = \tilde{t} \ , \tag{1.24}$$

where the overbar denotes the density normalized by its value on the reactants side, ρ_u. The transformation implies that:

$$\frac{\partial}{\partial \tilde{y}} = \overline{\rho} \frac{\partial}{\partial \xi} \tag{1.25}$$

$$\frac{\partial}{\partial \tilde{t}} = \int_0^{\tilde{y}} \left(\frac{\partial \overline{\rho}}{\partial \tilde{t}} \right) d\tilde{y}' \frac{\partial}{\partial \xi} + \frac{\partial}{\partial \tau} \tag{1.26}$$

To apply this transformation, we divide the continuity equation by ρ_u and integrate:

$$\int_{\tilde{y}}^{\tilde{y}} \frac{\partial \overline{\rho}}{\partial \tilde{t}} d\tilde{y}' + B \, \overline{\rho}(\tilde{y}) \, v_c(\tilde{y}) - B \, \overline{\rho}(0) \, v_c(0) = 0 \tag{1.27}$$

At the stagnation point $y = 0$ the total velocity must be zero. This requirement imposes the following boundary condition $v_c(0) = 0$ and equation (1.27) is reduced to:

$$\int_{\tilde{y}}^{\tilde{y}} \frac{\partial \overline{\rho}}{\partial \tilde{t}} d\tilde{y}' = - B \, \overline{\rho}(\tilde{y}) \, v_c(\tilde{y}) \tag{1.28}$$

Mapping equations (1.22-23) onto the (ξ, τ) domain and using the chain rule, expressions (1.25-26) and equation (1.28), we get:

$$\rho \, \frac{\partial Y_k}{\partial \tau} = B^2 \overline{\rho} \frac{\partial}{\partial \xi} \left(\frac{\rho D_k}{W_{mix}} \overline{\rho} \frac{\partial (W_{mix} Y_k)}{\partial \xi} \right) + \dot{\omega}_k W_k \ \ for \ k = 0, K \tag{1.29}$$

$$\rho \, c_p \frac{\partial T}{\partial \tau} = B^2 \, \overline{\rho} \frac{\partial}{\partial \xi} \left(\lambda \, \overline{\rho} \frac{\partial T}{\partial \xi} \right) - \sum_{k=0}^{K} \dot{\omega}_k H_k \tag{1.30}$$

Finally, equations (1.29-30) are non-dimensionalized using the length scale based on the thermal diffusion length, i.e. $y_{scl} = \sqrt{\alpha_u \, t_{scl}}$, where α_u is the thermal diffusivity coefficient of the mixture on the reactants side, $t_{scl} = \alpha_u / S_u^2$, and S_u is the unstrained flame burning velocity . Introducing the non-dimensional temperature, $\theta = (T - T_u) / (T_b - T_u)$, we get:

9

$$\rho \, \frac{\partial Y_k}{\partial \bar{\tau}} = B^2 \bar{\rho} \, \frac{1}{\alpha_u} \frac{\partial}{\partial \bar{\xi}} \left(\frac{\rho D_k}{W_{mix}} \, \bar{\rho} \, \frac{\partial (W_{mix} Y_k)}{\partial \bar{\xi}} \right) + t_{scl} \, \dot{\omega}_k \, W_k \quad for \; k = 0, K \quad , \quad (1.31)$$

$$\rho \, c_p \frac{\partial \theta}{\partial \bar{\tau}} = B^2 \, \bar{\rho} \, \frac{1}{\alpha_u} \frac{\partial}{\partial \bar{\xi}} \left(\lambda \, \bar{\rho} \, \frac{\partial \theta}{\partial \bar{\xi}} \right) - \frac{t_{scl}}{(T_b - T_u)} \sum_{k=0}^{K} \dot{\omega}_k \, H_k, \qquad (1.32)$$

where $\bar{\xi} = \xi / y_{scl}$, and $\bar{\tau} = \tau / t_{scl}$, and the boundary conditions are (1.10-11). These equations will be further modified after we consider the transport model in the next section.

1.2. Transport Model

In this section we discuss the evaluation of the transport coefficients λ and D_k, $k = 1, K$. We used the SANDIA Transport [4] and Premixed Flame [5] codes to study the variation of these parameters with temperature. The results of this investigation for the Lewis numbers $L_{e,k} = \lambda / (\rho \, c_p \, D_k)$ of all species in the stoichiometric, atmospheric pressure, methane/ air flame are presented in figures 2a-c. We employed the "starting" chemical kinetics mechanism used by Rogg [7]. From the figure it is clear that the Lewis numbers of all species are almost constant with temperature. These results are in agreement with these obtained e.g. in [2] where the following constant values of the Lewis numbers were used:

Species	Lewis Number
CH_4	0.97
O_2	1.11
H_2O	0.83
CO_2	1.39
H	0.18
O	0.70
OH	0.73
HO_2	1.10
H_2	0.30
CO	1.10
H_2O_2	1.12
HCO	1.27
CH_2O	1.28
CH_3	1.00
CH_3O	1.30

$$N_2 \ldots\ldots\ldots\ldots\ldots\ldots 1.00$$

The same *constant* values were used in our simulations.

In figure 3 the thermal conductivity coefficient λ is plotted as a function of temperature. The coefficient is obtained using three different methods: (1) The assumption $\lambda \rho = const = \lambda_u \rho_u$; (2) the Smooke correlation $\lambda = 2.58 \ 10^{-4} c_p \ (T/\ T_u)^r$ (CGS units), $r = 0.7$; (3) the SANDIA Transport code [4]. Methods (2) and (3) produce virtually identical results over the entire range of temperature, while method (1) overpredicts λ by 23 % in the flame zone. The reason for this overprediction can be seen in figure 4 where the product $\lambda \rho$ is plotted as a function of temperature. In the flame zone (1200 - 2200 K) the product is almost constant and the approximation works fairly well, but in the lower temperature range (T < 1000 K) the product increases from 2.5 at T = 1000 K to 3.0 at T = 300 K. The only advantage of $\lambda \rho = const = \lambda_u \rho_u$ approximation is that it helps to reduce the governing equations to a particular simple form. As we will see later, the application of this approximation leads to an overprediction of the laminar burning velocity by 10 %. If one wants to use this approximation, the best results would be obtained if $\lambda \rho$ is taken equal not to $\lambda_u \rho_u$ but to some intermediary value, say, 2.5 $g \ erg \ / \ sec \ -cm^4 -K$. In the following we used the Smooke correlation (2) to calculate the thermal conductivity coefficient λ.

Using the assumption of constant Lewis number, $L_{e, k} = \lambda/ (\rho \ c_p \ D_k) = const$, and the Smooke correlation $\lambda = 2.58 \ 10^{-4} c_p \ (T/\ T_u)^r$, we rewrite the diffusion terms in the governing equations (1.31-32). For the mass fraction equation:

$$\rho D_k \overline{\rho} = \frac{\lambda}{c_p L_{e,k}} \frac{\rho}{\rho_u} = \frac{1}{L_{e,k}} \frac{\lambda}{\lambda_u} \frac{c_{p,u}}{c_p} \frac{\rho}{\rho_u} \frac{\lambda_u}{c_{p,u}} = \frac{1}{L_{e,k}} \frac{\lambda}{\lambda_u} \frac{c_{p,u}}{c_p} \rho \ \alpha_u \ , \qquad (1.33)$$

where we used the definition of the thermal diffusivity coefficient, $\alpha_u = \dfrac{\lambda_u}{\rho_u \ c_{p,u}}$. For the energy equation:

$$\lambda \overline{\rho} = \lambda \frac{\rho}{\rho_u} = \lambda_u \frac{\lambda}{\lambda_u} \frac{\rho}{\rho_u} \frac{c_{p,u}}{c_{p,u}} = \alpha_u \rho \ c_{p,u} \frac{\lambda}{\lambda_u} \qquad (1.34)$$

Using the Smooke correlation and the equation of state, we evaluate:

$$\frac{\lambda}{\lambda_u} \frac{c_{p,u}}{c_p} = \left[\frac{T}{T_u}\right]^r , \qquad \frac{\lambda}{\lambda_u} = \frac{c_p}{c_{p,u}} \left[\frac{T}{T_u}\right]^r \qquad \frac{\rho}{\rho_u} = \frac{W_{mix}}{W_{mix, u}} \frac{T_u}{T} \qquad (1.35)$$

11

Dividing equations (1.31-32) by ρ and $\rho\ c_p$, respectively, and using equations (1.35), we obtain:

$$\frac{\partial Y_k}{\partial \bar{\tau}} = \frac{B^2}{L_{e,k}} \frac{\partial}{\partial \bar{\xi}} \left(\left[\frac{T}{T_u}\right]^{r-1} \frac{\partial}{\partial \bar{\xi}} \left(\frac{W_{mix}}{W_{mix,u}} Y_k\right) \right) + \frac{t_{scl} \dot{\omega}_k W_k}{\rho} \quad for\ k=0, K \quad (1.36)$$

$$\frac{\partial \theta}{\partial \bar{\tau}} = B^2 \ \frac{1}{c_p} \frac{\partial}{\partial \bar{\xi}} \left(c_p \left[\frac{T}{T_u}\right]^{r-1} \frac{W_{mix}}{W_{mix,u}} \frac{\partial \theta}{\partial \bar{\xi}} \right) - \frac{t_{scl}}{\rho\, c_p(\, T_b - T_u)} \sum_{k=0}^{K} \dot{\omega}_k H_k \quad (1.37)$$

with boundary conditions (1.10-1.11).

1.3 The Standard-State Thermodynamic Properties

The standard-state thermodynamic properties of species k are given in terms of the polynomial fits to the specific heats at constant pressure:

$$\frac{C_{p,k}}{R_u} = a_{0,k} + a_{1,k} T + a_{2,k} T^2 + a_{3,k} T^3 + a_{4,k} T^4 \quad (1.38)$$

$$\frac{H_k}{R_u T} = \frac{1}{R_u T} \int_0^T C_{p,k} dT\ ' = \quad (1.39)$$
$$a_{1,k} + a_{2,k} T/2 + a_{3,k} T^2/3 + a_{4,k} T^3/4 + a_{5,k} T^4/5 + a_{6,k}/T$$

$$\frac{S_k}{R_u} = \frac{1}{R_u} \int_0^T \frac{C_{p,k}}{T} dT\ ' = \quad (1.40)$$
$$a_{1,k} \ln T + a_{2,k} T + a_{3,k} T^2/2 + a_{4,k} T^3/3 + a_{5,k} T^4/4 + a_{7,k}$$

where the thermodynamic properties are given in molar units. Coefficients $a_{j,k}$ are taken from the SANDIA thermal data base and contained in the "thermdat" file. The format of a typical entry in the file is as follows:

CH3
 0.02844051E+02 0.06137974E-01 -0.0223034E-04 0.03785161E-08 -0.0245215E-12

12

0.16437809E+05 0.05452697E+02 0.02430442E+02 0.11124099E-01 -0.0168022E-03
0.16218288E-07 -0.0586495E-10 0.16423781E+05 0.06789794E+02 15.04
1.0e-00   0.0

The name of a species is written on the first line of the entry ; The next seven numbers represent the coefficients $a_{j,k}, j = 1, ..., 7$ for the low temperature range $0 < T < 1000 K$. The following seven numbers are the coefficients $a_{j,k}$ for the high temperature range $1000 < T < 5000 K$; the next number is the molecular weight of the species in g/ mole, followed by the Lewis number of the species, and, finally, the thermal diffusion coefficient $k_{T,k}$. This structure of the thermal data base is very close to that in [6]. The only difference is the addition of the molecular weight, the Lewis number and the thermal diffusion ratio. Once the thermodynamic properties are calculated using equations (1.38-40), the properties of the mixture for the given mass fraction vector $\{Y_0, Y_1, ..., Y_K\}^T$ and temperature T are evaluated using the following expressions:

$$c_p = \sum_{k=0}^{K} C_{p,k} \ Y_k / W_k \qquad (1.41)$$

$$W_{mix} = \left[\sum_{k=0}^{K} Y_k / W_k \right]^{-1} \qquad (1.42)$$

$$\rho = \frac{p \, W_{mix}}{R_u \, T} \qquad (1.43)$$

where c_p is the specific heat of mixture in the mass units.

13

1.4 Chemical Kinetics Mechanism

In the model the following mechanism of 18 elementary reactions and 13 reacting species was used to describe the methane oxidation [7]:

```
SPECIES :
    CH4 CH3 CH2O HCO CO2  CO
    H2  H  O2  O  OH  HO2 H2O N2 #
```

CH4+H=>CH3+H2	; 2.2E4	3.0	8527.7
CH4+OH=>CH3+H2O	; 1.6E6	2.1	2452.2
CH3+O=>CH2O+H	; 7.0E13	0.0	0.0
CH2O+H=>HCO+H2	; 2.5E13	0.0	40003.3
CH2O+OH=>HCO+H2O	; 3.0E13	0.0	1199.8
HCO+H=>CO+H2	; 2.0E14	0.0	0.0
HCO+M=>CO+H+M	; 7.14E14	0.0	16811.7
HCO+O2=>CO+HO2	; 3.0E12	0.0	0.0
CO+OH=>CO2+H	; 4.4E6	1.5	-740.9
CO2+H=>CO+OH	; 1.6E14	0.0	26338.4
H+O2=>OH+O	; 1.2E17	-0.91	16532.0
OH+O=>H+O2	; 1.8E13	0.0	0.0
O+H2=>OH+H	; 1.5E7	2.0	7564.5
OH+H=>O+H2	; 6.7E6	2.0	5573.6
OH+H2=>H2O+H	; 1.0E8	1.6	3303.0
H+H2O=>OH+H2	; 4.6E8	1.6	18601.8
2*OH=>H2O+O	; 1.5E9	1.14	0.0
H2O+O=>2*OH	; 1.5E10	1.14	17282.5
H+O2+M=>HO2+M	; 2.0E18	-0.8	0.0
HO2+M=>H+O2+M	; 2.77E18	-0.8	46701.7
H+OH+M=>H2O+M	; 2.15E22	-2.0	0.0
H2O+M=>H+OH+M	; 3.87E23	-2.0	119397.7
HO2+H=>2*OH	; 1.5E14	0.0	1001.4
HO2+H=>H2+O2	; 2.5E13	0.0	690.7
HO2+OH=>H2O+O2	; 2.0E13	0.0	0.0

The mechanism is capable of predicting with reasonable accuracy the burning velocity and the profiles of temperature and species mass fraction in lean to stoichiometric flames. The file "methmech", which contains the chemical kinetics mechanism, is read by an interpreter function before the calculations starts. The format of the file is as follows:

  * the first line of the file contains the word "SPECIES" followed by the list of species participating in the scheme. The names of the species in the list are separated by a blank space. The order in which the species appear in the list is the order in which the species data will be written in the chemical kinetics data base. The list of the species is closed by a symbol "#".

* next lines of the file describe the chemical kinetics equations. A chemical kinetics equation must contain the species names given in the list. The left-hand side and the right-hand side of the chemical kinetics equation are separated by a symbol "=" in the case of a reversible reaction, or by a symbol "=>" in the case of an irreversible reaction. By default the code assumes that the stoichiometric coefficient of the species in a given reaction is unity; in the opposite case, the stoichiometric coefficient is equal to the number in front of the species symbol. The chemical kinetics reaction line is closed by a symbol ";".

* the three numbers, following the chemical kinetics equation, are: the pre-exponential constant A_i; the temperature exponent β_i; and the activation energy $E_{a,k}$ of reaction i. The reaction i line is closed by a blank symbol.

* if a chemical kinetics equation contains symbol "M", it means that the reaction rate is enhanced by third bodies. The values of the third body efficiencies for particular species are specified separately for each reaction mechanism considered.

Following [6], we write a reaction equation in the general symbolic form:

$$\sum_{k=0}^{K} v'_{ki} \, \chi_k = \sum_{k=0}^{K} v''_{ki} \, \chi_k \tag{1.44}$$

where v'_{ki} is the stoichiometric coefficient of species k in reaction i. The production rate of species k in all I reactions of the specified reaction mechanism is given by :

$$\dot{\omega}_k = \sum_{i=0}^{I} (v''_{ki} - v'_{ki}) \, \dot{q}_i \tag{1.45}$$

where $\dot{q}_i$ is the rate-of-progress variable equal to:

$$\dot{q}_i = k_{f,i} \prod_{k=0}^{K} [X_k]^{v'_{ki}} - k_{r,i} \prod_{k=0}^{K} [X_k]^{v''_{ki}} \tag{1.46}$$

In this expression $[X_k]$ is the molar concentration of species k : $[X_k] = \rho \, Y_k / W_k$; the forward rate constant $k_{f,i}$ of reaction i is calculated as

$$k_{f,i} = A_i \, T^{\beta_i} \, exp \, (- E_{a,i} / R_u T) \tag{1.47}$$

The coefficients A_i, β_i and $E_{a,\,i}$ in this expression are provided by the input "methmech" file. If the chemical reaction i is irreversible, then the reverse rate constant $k_{r,\,i}$ is equal to zero. If the reaction is reversible, the equilibrium constant is evaluated first:

$$K_{c,\,i} = \left(\frac{p_{atm}}{R_u T}\right)^{\sum_{k=0}^{K} (v''_{ki} - v'_{ki})} exp\left(\sum_{k=0}^{K} (v''_{ki} - v'_{ki}) \left[\frac{S_k}{R_u} - \frac{H_k}{R_u T}\right]\right) \tag{1.48}$$

where p_{atm} is the pressure of 1 atmosphere. In the next step, the reverse rate constant $k_{r,\,i}$ is calculated:

$$k_{r,\,i} = k_{f,\,i} / K_{c,\,i} \tag{1.49}$$

If a reaction contains the "third body" M, the rate-of-progress expression (1.46) is multiplied by

$$M_i = \sum_{k=0}^{K} \alpha_{ki} \, [X_k]$$

By default the code presumes that α_{ki} of species k in reaction i is equal to zero. If for some species α_{ki} is not equal to zero, it has to be specified in the code. For our reaction mechanism the values of the third body efficiencies are [7]:

$$\alpha_{H,\,i} = 1 \qquad \alpha_{H_2,\,i} = 1 \qquad \alpha_{O_2,\,i} = 0.4 \quad \alpha_{H_2O,\,i} = 6.5 \qquad \alpha_{CO,\,i} = 0.75$$

$$\alpha_{CO_2,\,i} = 1.5 \qquad \alpha_{CH_4,\,i} = 6.54 \qquad \alpha_{N_2,\,i} = 0.4 \tag{1.50}$$

These values are the same for every reaction with third bodies.

In the numerical solution of equations (1.36-37) we need to evaluate the derivatives:

$$\partial \dot{\omega}_k / \partial \theta \qquad \text{and} \qquad \partial \dot{\omega}_k / \partial Y_j$$

The derivation of these derivatives is a tedious procedure and we will give only the final expressions:

$$\frac{\partial \dot{\omega}_k}{\partial Y_j} = \sum_{i=0}^{I} (v''_{ki} - v'_{ki}) \left[M_i \, k_{f,\,i} \, \frac{\partial \Pi_{f,\,i}}{\partial Y_j} - M_i \, k_{r,\,i} \, \frac{\partial \Pi_{r,\,i}}{\partial Y_j} + \frac{\dot{q}_i}{M_i} \frac{\rho \, \alpha_{j,\,i}}{W_j}\right] \tag{1.51}$$

$$\frac{\partial \dot{\omega}_k}{\partial T} = \sum_{i=0}^{I} (v_{ki}'' - v_{ki}') \left(\dot{q}_i - \frac{k_{f,i} \Pi_{f,i} M_i}{T} \sum_{m=0}^{M_i} v_{mi}' + \frac{k_{r,i} \Pi_{r,i} M_i}{T} \sum_{l=0}^{L_k} v_{li}'' \right. \qquad (1.52)$$

$$\left. - k_{r,i} \Pi_{r,i} M_i \sum_{l=0}^{L_i} (v_{li}'' - v_{li}') \left(\frac{H_l}{R_u T^2} - \frac{1}{T} \right) \right) - \frac{\dot{\omega}_k}{T}$$

where

$$\frac{\partial \Pi_{f,i}}{\partial Y_j} = \Pi_{f,i} \left\{ \frac{v_{ji}'}{Y_j} - \frac{W_{mix}}{W_j} \sum_{n=0}^{N_i} v_{ni}' \right\} \qquad \frac{\partial \Pi_{r,i}}{\partial Y_j} = \Pi_{r,i} \left\{ \frac{v_{ji}''}{Y_j} - \frac{W_{mix}}{W_j} \sum_{n=0}^{N_i} v_{ni}'' \right\}$$

$$\Pi_{f,i} = \prod_{l=0}^{L_i} [X_l]^{v_{li}'} \qquad \Pi_{r,i} = \prod_{l=0}^{L_i} [X_l]^{v_{li}''}$$

and $\sum_{l=0}^{L_i} v_{li}''$ is the sum of all stoichiometric coefficients on the right-hand-side of equation i.

2.1 Numerical Solution

The numerical solution of equations (1.36-37) with boundary condition (1.10-11) is obtained using a Crank-Nicholson finite-difference scheme with an implicit approximation of the source term to maintain stability:

$$\frac{\theta_i^{n+1} - \theta_i^n}{\Delta \tau} = \frac{1}{2} \left(RHS_i^{n+1} + RHS_i^n \right), \qquad (2.1)$$

where $\Delta \tau$ is the non-dimensional time step, RHS is the notation for the right-hand-side of equation (1.37), the upper index denotes the time level, and the lower index is the grid point number in $(\bar{\xi}, \bar{\tau})$ domain. The scheme is illustrated by the finite-difference approximation of equation (1.37). The derivations for equation (1.36) are similar.

At time level n+1, the non-dimensional source term of equation (1.37):

17

$$\overline{\dot{\Omega}} \equiv \frac{t_{scl}}{\rho \, c_p \, (T_b - T_u)} \sum_{k=0}^{K} \dot{\omega}_k \, H_k \tag{2.2}$$

is approximated by:

$$\overline{\dot{\Omega}}_i^{n+1} \cong \overline{\dot{\Omega}}_i^{n} + (\partial \overline{\dot{\Omega}}/\partial \tau)_i^{n} \, d\tau \approx \overline{\dot{\Omega}}_i^{n} + (\partial \overline{\dot{\Omega}}/\partial \theta)_i^{n} \, d\theta \cong \overline{\dot{\Omega}}_i^{n} + (\partial \overline{\dot{\Omega}}/\partial \theta)_i^{n} \, (\theta_i^{n+1} - \theta_i^{n}),$$

where derivatives $(\partial \overline{\dot{\Omega}}/\partial \overline{Y})_j^{n}$ were neglected since they are, as it was shown in [1], much smaller than $(\partial \overline{\dot{\Omega}}/\partial \theta)_i^{n}$. The finite-difference approximation of equation (1.37) is:

$$\frac{\theta_i^{n+1} - \theta_i^{n}}{\Delta \tau} = \frac{1}{2} \Big\{ \Big(\frac{B^2}{c_p} \frac{\partial}{\partial \overline{\xi}} (\, cf \, \frac{\partial \theta}{\partial \overline{\xi}}) \Big)_i^{n+1} + \overline{\dot{\Omega}}_i^{n} + (\partial \overline{\dot{\Omega}}/\partial \theta)_i^{n} \, (\theta_i^{n+1} - \theta_i^{n}) + \\ \Big(\frac{B^2}{c_p} \frac{\partial}{\partial \overline{\xi}} (\, cf \, \frac{\partial \theta}{\partial \overline{\xi}}) \Big)_i^{n} + \overline{\dot{\Omega}}_i^{n} \Big\} \tag{2.3}$$

where the following notation was introduced:

$$cf \equiv c_p \Big(\frac{T}{T_u} \Big)^{r-1} \frac{W_{mix}}{W_{mix,u}} \tag{2.4}$$

The diffusion term in equation (2.3) at time layer n is approximated as follows:

$$\Big(\frac{B^2}{c_p} \frac{\partial}{\partial \overline{\xi}} (\, cf \, \frac{\partial \theta}{\partial \overline{\xi}}) \Big)_i^{n} = \Big(\frac{B^2}{c_p} \Big)_i^{n} \frac{2}{\overline{\xi}_{i+1}^{n} - \overline{\xi}_{i-1}^{n}} \Big\{ cf_{i+1/2} \frac{\theta_{i+1}^{n} - \theta_i^{n}}{\overline{\xi}_{i+1}^{n} - \overline{\xi}_i^{n}} - cf_{i-1/2} \frac{\theta_i^{n} - \theta_{i-1}^{n}}{\overline{\xi}_i^{n} - \overline{\xi}_{i-1}^{n}} \Big\} \tag{2.5}$$

where $\quad cf_{i+1/2} \equiv (\, cf_{i+1} + cf_i) / 2 \qquad cf_{i-1/2} \equiv (\, cf_i + cf_{i-1}) / 2$

The term at time layer n+1 is approximated in a similar fashion. The derivative $(\partial \overline{\dot{\Omega}}/\partial \theta)_i^{n}$ is equal to

$$(\partial \overline{\dot{\Omega}}/\partial \theta)_i^{n} = \frac{t_s}{(c_p)_i^{n}} \Big\{ \sum_{k=0}^{K} H_{k,i}^{n} \Big(\frac{\partial}{\partial T} \frac{\dot{\omega}_k}{\rho} \Big)_i^{n} + \sum_{k=0}^{K} (C_{p,k})_i^{n} \Big(\frac{\dot{\omega}_k}{\rho} \Big)_i^{n} - \Big(\frac{1}{c_p} \frac{\partial c_p}{\partial T} \Big)_i^{n} \sum_{k=0}^{K} \Big(\frac{\dot{\omega}_k}{\rho} H_k \Big)_i^{n} \Big\}$$

18

The finite-difference representation of the mass fraction equation (1.36) is obtained in a similar way. The finite-difference equations are solved by a Thomas tridiagonal matrix inversion algorithm.

The grid in the computational domain $(\bar{\tau}, \bar{\xi})$ is nonuniform. It is adapted in such a way that the regions of high gradients and large variations of the dependent variables $Y_0, Y_1, ..., Y_K, \theta$ are continuously resolved. Each time step, for every mass fraction and temperature profile, the following criteria are verified:

$$|f_{i+1} - f_i| < \alpha \, |max \, (f) - min(f)|$$

$$\left| \left(\partial f / \partial \bar{\xi} \right)_{i+1} - \left(\partial f / \partial \bar{\xi} \right)_i \right| < \beta \, \left| max \left(\partial f / \partial \bar{\xi} \right) - min \left(\partial f / \partial \bar{\xi} \right) \right| \tag{2.6}$$

where α and β are the adaptation tolerance parameters of the order of 0.1; f_i and $\left(\partial f / \partial \bar{\xi} \right)_i$ are the values of a dependent variable and its derivative at grid point i. If criteria (2.6) are not satisfied at grid point i, a new grid point is introduced half way between the points $i+1$ and i. The values of mass fractions and temperature at that midpoint are calculated as the average values:

$$f_{i+1/2} = (f_{i+1} + f_i) / 2$$

It can be demonstrated that this kind of interpolation provides the second order of accuracy.

At the onset of every time step the thermal thickness of the flame is compared with the distance from the flame to the upstream and downstream boundaries of the computational domain. If either of these distances is smaller than two flame thicknesses, the computational domain is regridded by removing every second grid point from the mass fraction and temperature profiles and adding them to the boundaries of the domain with the space step equal to the mean mesh size of the "old" grid. The values of the mass fractions and the temperature at the added mesh points are taken to be equal to the boundary values of the "old" mesh. Hence, the zero-gradient boundary conditions are naturally satisfied for the new mesh. The total number of mesh points is not changed by the regridding procedure. Each time step, the physical coordinate y_i is recalculated in such a way that the stagnation point, $y_i = 0$, remains fixed.

The time step of the calculations is the minimum of the characteristic time scales of species production:

$$t_{scl, k} \equiv [X_{k, max}] / max \{\dot{\omega}_k\} / 3 \tag{2.7}$$

where $max \{\dot{\omega}_k\}$ is the maximum of the production rate of species k and $[X_{k, max}]/$ is the molar concentration of species k at this maximum; and the computational time scale based on a Courant criterion:

$$t_{scl, Courant} \equiv min \{\Delta \overline{\xi}\}^2 exp(-2 K_a \overline{\tau}), \tag{2.8}$$

i.e.

$$d\tau = min \{t_{scl, 0}, t_{scl, 1}, t_{scl, 2}, ..., t_{scl, K}, t_{scl, Courant} / number \} \tag{2.9}$$

where the *number* is specified in the keyword input file "input1". We found that in most of our runs the Courant time scale is the smallest and actually determines the time step of the calculations. Equation (2.8) shows that the Courant time step is an exponentially decreasing function of time. For highly strained flames (large K_a), the time step decreases rapidly with time, exponentially slowing down the calculation. A way to solve this problem is to regrid the computational domain (increase $min \{\Delta \overline{\xi}\}^2$) whenever the time step becomes exceedingly small.

3.1 The Structure of the Code

The structure of the Unsteady Strained Flame Code is shown in Table 1. The code uses the freely-propagating premixed flame mass fraction and temperature profiles generated by the SANDIA Premixed Flame Code [5] as initial profiles for the solution of the unsteady strained flame problem. Both the SANDIA code and our code employ the same chemical kinetics mechanism. The initial conditions are written in the file "raw.dat" using the following format:

- number of species NSP +3, number of grid points NG, pressure, the mass flux
- grid points positions, in cm
- solution matrix:

$$Y(0, 0)\ Y(1, 1) ... Y(NSP, 0)\quad T(0)\quad \text{flow rate (0)}$$
$$Y(0, 1)\ Y(0, 1) ... Y(NSP, 1)\quad T(1)\quad \text{flow rate (1)}$$

....

where $Y(k,i)$ denotes the mass fraction of species p at grid point i. Reaction description and thermal data base file formats were described in detail earlier in sections 1.4 and 1.3, respectively. The reaction description file is read by an interpreter function "input". This function is used to set up three data bases: (1) the thermal data base *spc*; (2) the reaction data base *reaction*; and (3) the species data base *elmnt_dat*. The data bases are organized as global structures. Hence, each entry in a data base can be "seen" by any function of the code. Three data input files "thermdat", "methmech", and "raw.dat" are read by the functions "therm_dat", "input", and "init_prfls", respectively. The functions are located in the library functions file "flmlib2.c". This file contains the functions dealing with the calculation of the chemical kinetics and thermodynamics related data, the source terms and their derivatives. At each time level, for a given solution vector $\{\vec{x},\ \vec{Y},\ T\}^T$, the functions in the "flmlib2.c" file calculate:

$$H_k,\ S_k,\ C_{p,\,k},\ c_p,\ W_{mix},\ \rho,\ k_{f,\,i},\ k_{r,\,i},\ K_{c,\,i}\qquad,\ \dot{q}_i,\ \dot{\omega}_k$$

$$\sum_{k=0}^{K}\ \dot{\omega}_k\,H_k,\ [X_k],\ \partial\dot{\omega}_k/\,\partial\theta,\ \partial\dot{\omega}_k/\,\partial Y_j,\ \overline{\partial\dot{\Omega}_k}/\,\partial Y_k,\ \overline{\partial\dot{\Omega}}/\,\partial\theta,$$

$$(3.1)$$

where index k denotes the species number in species data base *elmnt_dat*. The module "flmlib2.c" is general and can be used in any other program dealing with a complex chemical kinetics mechanism. The pre-calculated arrays (3.1) are stored as the global memory class elements which makes them "visible" to all functions of the code. File "flmainS.c" is the flame code itself. It is supplied by the pre-calculated arrays (3.1) and "propagates" the mass fractions and temperature profiles in time. It contains the subroutines dealing with:

- the calculation of the Thomas tri-diagonal inversion coefficients,
- the adaptation of the grid,
- the regridding of the computational domain,
- output,
- transformations from the computational to physical domain,
- the calculation of the variable time step,
- inversion.

First, the flame code "flmainS.c" reads the keyword input file "input1" which has the following format:
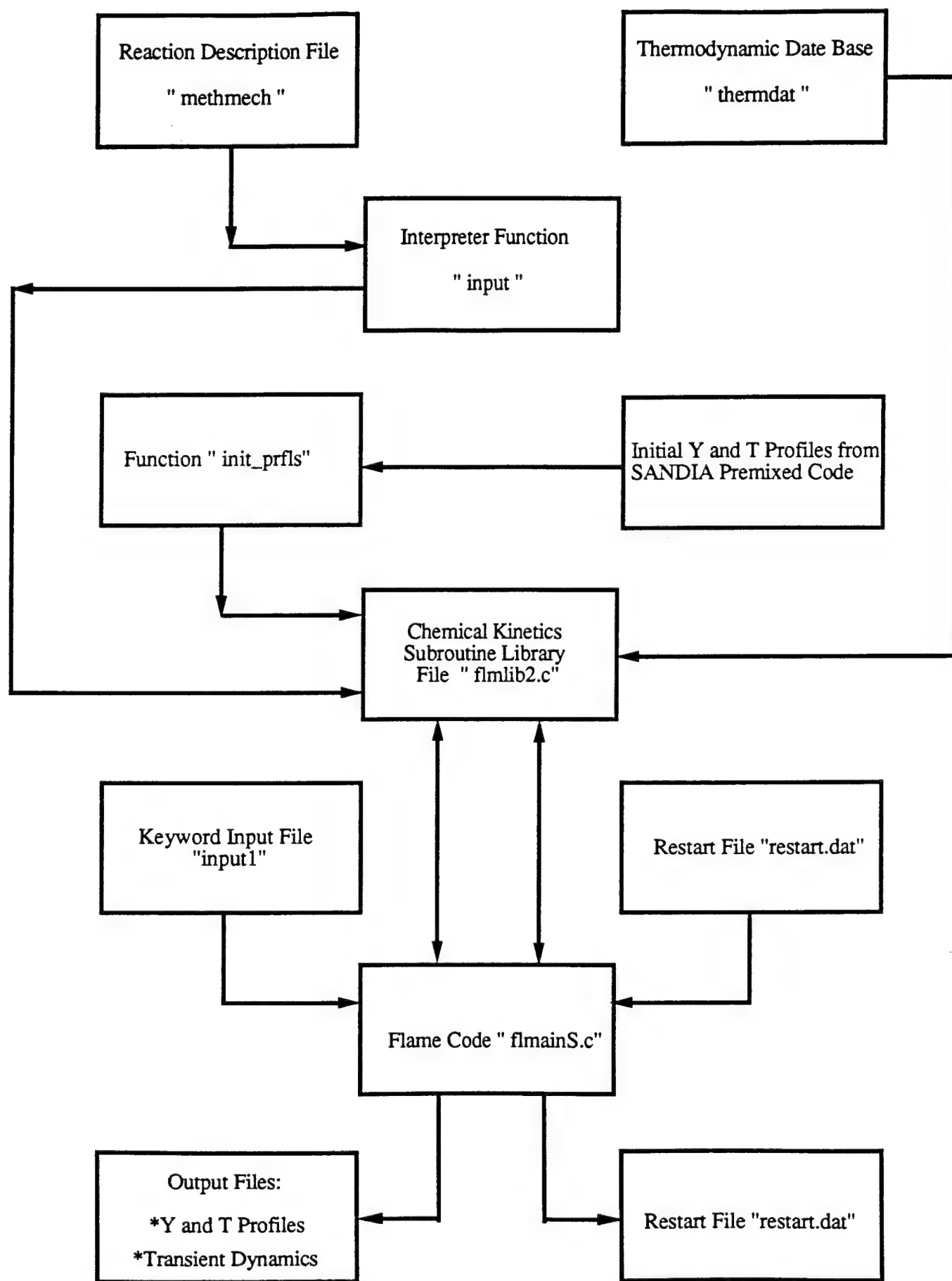
Table 1.

file input1:

```
1.0e+03
2.0e-03
1.0
0.3
0.4
yes
```

The first line of the input file specifies the externally imposed strain rate in 1/sec; second line is the time in sec. when the calculation stops; third line determines the computational time step of the calculation. The computational time step is equal to $t_{scl, Courant}$ divided by the number specified in the third line. The next two lines give the adaptation tolerance parameters α and β. The keyword "yes" means that the calculation will start not from the profiles provided by the SANDIA Premixed Flame Code [5], but from the previously recorded output of the Unsteady Strained Flame Code. This is frequently done to match the initial location of the flame with the stagnation point in order to compare, for example, the responses of the flame to different strains. Every $\Delta t = 2 \ 10^{-4}$ sec. the flame code produces the output files mjr00# (the major species and the temperature profiles) and mnr00# (the minor species and the total heat release profiles). The last digit "#" in the name of a file denotes the time when the file was written out. Thus, the file mnr003 contains the minor species profiles at time $3 * \Delta t = 6 \ 10^{-4}$ sec. from the start of the calculations. The transient integral parameters of the flame (the burning velocity, the total heat release rate, the flame location) are written into the file "omg.dat" every 100 time steps . The restart file "restart.dat" is produced when the calculations stop.

4.1 Results and discussion

The results obtained using the described model are compared with that of the Smooke model [2] for the unstrained flame; and the Rogg model [7] for the strained flame. The following parameters are used in the comparison:

(a) the burning velocity S_u [cm/ sec]
(b) the flame location y_f [cm] defined as the location of the maximum fuel consumption
(c) the total heat release rate $\dot{Q}$ [kJ/ cm^2-sec]

22

(d) the shape of the normalized profiles, where the normalized distance is given by:

$$\hat{y} = \rho_u \, S_u \, (y - y_f) \, c_p / \, \lambda \tag{4.1}$$

We define the burning velocity S_u of the steady propagating unstrained flame as follows. The mass fraction equation for species k is given by:

$$\rho \, \frac{\partial Y_k}{\partial t} + \rho v \, \frac{\partial Y_k}{\partial y} = \frac{\partial}{\partial y} \left(\frac{\rho D_k}{W_{mix}} \frac{\partial (W_{mix} Y_k)}{\partial y} \right) + \dot{\omega}_k \, W_k \quad for \ k = 0, K \tag{4.2}$$

For a steady propagating flame the first term in this equation is equal to zero and the mass flow rate is conserved:

$$\rho v \, \frac{\partial Y_k}{\partial y} = \frac{\partial}{\partial y} \left(\frac{\rho D_k}{W_{mix}} \frac{\partial (W_{mix} Y_k)}{\partial y} \right) + \dot{\omega}_k \, W_k \tag{4.3}$$

$$\rho v = \rho_u \, S_u = const \tag{4.4}$$

Using equation (4.4), we integrate equation (4.3) with respect to y from $+\infty$ to $-\infty$ to obtain:

$$\rho v \, (Y_{k,u} - Y_{k,b}) = \left(\frac{\rho D_k}{W_{mix}} \frac{\partial (W_{mix} Y_k)}{\partial y} \right)_u - \left(\frac{\rho D_k}{W_{mix}} \frac{\partial (W_{mix} Y_k)}{\partial y} \right)_b + \int_{-\infty}^{+\infty} \dot{\omega}_k \, W_k dy \tag{4.5}$$

Far ahead and far behind the flame, in the unburnt and burnt mixtures, respectively, the mixture reaches equilibrium, and, hence, the gradients on the right-hand side of equation (4.5) vanish and

$$\rho v \, (Y_{k,u} - Y_{k,b}) = \int_{-\infty}^{+\infty} \dot{\omega}_k \, W_k dy \tag{4.6}$$

For methane, CH_4, $Y_{CH_4, b} = 0$,, and equation (4.6) yields the following expression for the burning velocity:

$$S_u = \frac{1}{\rho_u Y_{CH4,u}} \int_{-\infty}^{+\infty} \dot{\omega}_{CH4} W_{CH4} dy \qquad (4.7)$$

This expression has physical meaning only when the flame reaches a steady-state. During the transient period, the presence of the unsteady term obscures the interpretation of the expression. Other characteristics of the flame are defined as follows:

- the flame location,

- the total heat release rate $\dot{Q} \equiv \int_{-\infty}^{+\infty} \sum_{k=0}^{K} \dot{\omega}_k H_k dy$ \qquad (4.8)

These two characteristics are more appropriate for the description of the transient behavior of a flame.

4.2 The unstrained flame

Although the model is derived for the unsteady *strained* flame, it can be used to study the unstrained flame in the limiting case when the externally applied strain rate tends to zero or is much smaller than the extinction strain. The strain rate in our calculations was equal to 1.0e-04 1/sec. Two models were used to evaluate the thermal conductivity coefficient λ:

Transport model 1: $\lambda \rho = \lambda_u \rho_u = const$, and
Transport model 2: $\lambda / c_p = A (T/T)'$, where $A = 2.58 \ 10^{-4}$ g/ cm-sec and $r = 0.7$

In figure 5a the burning velocity (4.7) is shown as a function of time for the transport model 1. The calculations start at time $t = 0$ with the profiles generated by the SANDIA Premixed Flame Code [5]. As it was mentioned earlier, the transient values of the burning velocity has little physical meaning since the burning velocity (4.7) is calculated using the steady-state assumption. As figure 5a shows, the burning velocity starts from 50 cm/ sec, decreases, and in 5.e-04 sec. reaches a steady-state value of 40.4 cm/ sec. As it was mentioned in section 1.2, Transport Model 1 overpredicts the values of λ in the reaction zone by 23 %. This is the reason for the steady-state burning velocity of 40.4 cm/sec

24

being higher than the experimental value of 37 cm/ sec. Figures 5b and 5c show the total heat release rate and the flame location as functions of time. The pattern of the total heat release rate variation is similar to that of the burning velocity. It starts from a value of 0.13 kJ/ cm^2-sec at time zero and drops to a steady-state value of 0.104 kJ/cm^2-sec in 5.e-04 sec. The flame location, y_f, after some short transient period, starts to change linearly with time as it is expected from a steady propagating premixed flame. The slope of the $y_f(t)$ line gives us the propagation velocity of the fuel consumption layer. For an unstrained flame, the velocity S_u is related to the velocity of the fuel consumption layer by the mass conservation principle:

$$S_u = \frac{\rho(\ max\ \dot{\omega}_{CH_4})}{\rho_u} \frac{\partial y_f}{\partial t} \qquad (4.9)$$

Since Transport Model 1 does not predict correctly the thermal conductivity coefficient λ in the reaction zone, in the following simulations we used only Transport Model 2.

The integral characteristics of the flame, S_u, y_f, h_t, obtained using Transport Model 2 are shown in figures 6a-c. The flame starts to propagate at the burning velocity $S_u = 45\ cm/ sec$, $y_f = 9.9\ cm$, $h_t = 0.12\ kJ\ /\ cm^2\text{-}sec$ and reaches the steady-state values of $S_u = 36.6\ cm/ sec$, $h_t = 0.1\ kJ\ /\ cm^2\text{-}sec$ in approximately 4.5e-04 sec. The flame location is a linear function of time. The steady-state value of 36.6 cm/sec is much closer to the experimental value of 37.6 cm/sec than the value of 40.4 cm/sec provided by Transport Model 1. In figures 7-15 we compare our temperature and mole fraction profiles plotted versus the normalized coordinate (4.1) with that of [2]. The construction of the normalized coordinate (4.1) suggests that a good agreement in the shapes of profiles can be obtained only if: (a) the profiles in the physical domain are correct, and (b) the integral characteristics of the flame (S_u , in particular) are correct.

In figure 7 the temperature profile of [2] (dashed line) is compared with the profile of the present model. The general agreement between the profiles is reasonably good, although the model slightly overpredicts the temperature in the post-flame region. It should be noted that the equilibrium values of the temperature in the present model and in [2] are the same due the boundary conditions imposed. The observed difference in the post-flame temperature can be explained by the fact that the size of domain is not large enough for the profile to reach an equilibrium value. We can expect that the discrepancy in the temperature profiles will affect the profiles of the minor species in this region. Temperature on the reactants side is slightly underpredicted. In figure 8 the CH_4 mole fraction profiles of the two models are compared. The agreement is very good, although

25

our model produces slightly lower values for X_{CH_4} behind the reaction zone $\hat{y} = 0$ than these obtained in Smooke's model [2]. This can be explained by the higher values of temperature in that region. In figures 9-14 the major species H_2O, H_2, O_2, CO, CO_2 and N_2 mole fraction profiles of two models are compared, respectively. The agreement between these profiles is excellent. The last profile presented here is the H mole fraction profile shown in figure 15. Although the part of the profile on the reactants side and its maximum value of it are captured by our model with a reasonable accuracy, the post-flame part of the profile is lower than that predicted in [2]. This fact could be explained by the high sensitivity of H profile to temperature and by the overprediction of temperature in the post-flame region by our model (see figure 7).

We *conclude* that the present model of the unsteady strained flame is able to predict correctly the burning velocity, heat release rate, the profiles of temperature, major and minor species of the unstrained flame if the externally imposed strain rate is small ($\varepsilon < 100 \ sec^{-1}$). Slight differences in the burning velocity and in the shapes of some profiles (T and H, in particular) can be attributed to the differences in the chemical kinetics mechanisms utilized in [2] and in our model. Although in both model the "starting" mechanism of methane oxidation is used, the reactions of CH_4 oxidation in [2] are written in a Lindemann fall-off form and are different from that of the present model.

4.3 The "unsteady" strained flame

The predictions of our model for a highly strained flame of $\varepsilon = 1,000 \ 1/sec$ are compared with the results obtained by Rogg [7]. In both simulations, the same chemical kinetics schemes and the transport models are used. In figures 16a-c the integral parameters of flame are shown as functions of time. The calculations start with the SANDIA profiles. In figure 16a the burning velocity S_u drops from 44 cm/sec to a steady-state value of 34 cm/sec. In order to compare the simulations with different strain rates, the flame is placed initially at the stagnation point $y = 0$. Figure 16b depicts the flame location, y_f, as a function of time. The flame starts its propagation at $y = 0$. After some time the flame begins to "feel" the influence of the external velocity field and its speed slows down continuously until it reaches a steady-state at $y = 0.17$ cm. This value is higher than the corresponding value of 0.1 cm in [7]. Figure 16c shows the variation of the heat release rate with time. It goes from a value of 0.12 kJ/ cm^2-sec and reaches a steady-state value of 0.8 kJ/cm^2-sec. Similar to that in [1], the burning velocity and the

26

heat release rate reach the steady state much faster than the flame location. Next, we compare the profiles of the major and minor species. Again, the profiles of [7] are plotted broken line for comparison. Since the steady-state location of the flame in our model is different from that of [7], the profiles of [7] were shifted in such a way that the positions of the fuel consumption layers in both models match. In figure 17 the temperature profiles are compared. These exhibit very close similarity, especially in the reaction zone region. In the post-flame zone, the temperature is higher in the Rogg's results [7]. As it was mentioned above, the equilibrium values of the temperatures in both models are the same by definition but the size of the domain shown in the picture is not large enough for our profile to reach this value. In figures 18 and 19 the CH_4 and O_2 mass fraction profiles of both models are plotted. They are virtually identical. In figure 20 the CO_2 mass fraction profiles are compared. The profiles are identical in the reaction zone and differ slightly in the post-flame region. The profile of CO_2 predicted in [7] has slightly higher values of CO_2 mass fraction here. The same could be said about the CO mass fraction profiles compared in figure 21. The profiles match almost precisely in the reaction zone, including the maximum values of CO mass fraction, but diverge in the post-flame region. The comparison of the H_2O profiles is presented in figure 22. Again, the profiles match almost exactly everywhere in the field. A slight discrepancy is observed only in the reaction zone. The previously plotted profiles represent the temperature and the major species. The model described in this paper predicts well almost all of them, except the CO profile.

A more severe test for a model is a comparison of the *minor species* profiles. These species are present in tiny concentrations. Many of them are extremely sensitive to the temperature and chemical kinetics mechanism. In figure 23 the mass fraction profiles of HO_2 are compared. They exhibit reasonable similarity in terms of thickness although the peak value is slightly overpredicted by our model. It should be noticed that the HO_2 profile is located ahead of the flame, in the region which is predicted by our model particularly well. The situation changes for OH profile presented in figure 24. While, again, the reaction zone side of the profile matches well, the post-flame part of our profile is significantly higher than that of [7]. The similar trend is observed for the H and O profiles in figures 25 and 26, respectively, while the H_2 profile is predicted reasonably well, as it is shown in figure 27. The similarity among the trends in the OH, H and O profiles can be explained by the fact that they are related to each other through the following mechanism of H_2 oxidation:

$$H_2 + O \leftrightarrow OH + H$$

$$H + O_2 \leftrightarrow OH + O$$
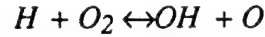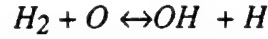
Figures 24, 25 and 26 show that the reason why our model overpredicts the post-flame zone is the fact that the flow is not strained as much as it should be. The equilibrium values of the mass fractions are the same for both models. A higher strain would cause a shrinking of the physical domain which, in turn, would move OH, O or H profiles closer to the flame, making them steeper in the post-flame region. The reason why the post-flame region is understrained could be the absence of the momentum equation in our model. As it was mentioned earlier in section 1.1, the momentum equation is identically equal to zero on the stagnation streamline. Nevertheless, it provides a boundary condition which links the strain rate on the reactants and products sides [7]:

$$\varepsilon_b = \varepsilon_u \sqrt{\rho_u/\rho_b} \tag{4.10}$$

This boundary condition follows from assumption $(\partial p/\partial x)_{-\infty} = (\partial p/\partial x)_{+\infty}$. It shows that the strain rate on the products side must be approximately $\sqrt{\rho_u/\rho_b} \approx 2.75$ times greater than that on the reactants side. On the reactants side, and inside the reaction zone the combustion generated velocity component $\vec{v}_c$ accounts for the velocity field created by the density variation in the flame. The temperature, major and minor species profiles are predicted correctly in that region. However, far from the reaction zone the $\vec{v}_c$ velocity component is unable to provide the correct asymptotic behavior of the velocity field which should have been imposed by satisfying the momentum equation. The physical domain in that region is thus understrained. That also explains why the steady-state location of the flame is overpredicted in our model.

In order to correct this flaw, an attempt has been made to specify the right asymptotic values of the velocity by constructing the strain rate field in the following fashion:

$$\varepsilon = \varepsilon_u, \, y > y_*$$
$$\varepsilon = (\varepsilon_u + \varepsilon_b)/2, \, y = y_* \qquad \text{and} \tag{4.11}$$
$$\varepsilon = \varepsilon_b, \, y < y_*$$

Two values have been chosen: (1) $y_* = 0$, and (2) $y_* = y_f(t)$. It should be noted that the construction of the strain rate field in this way does not violate the validity of the transformations of section 1.1. The computational domain is split into two sub-domains. The values of all dependent variables, including the total velocity, are continuous across the boundary. A typical steady-state profile for the first choice of the characteristic y_* is shown in figure 28. The H mass fraction profile (a thick dotted line) is compared with the profile obtained for the case of the uniform strain rate field. The reaction zone parts of the profiles are virtually identical, while the post-flame values of the two-strain-zone, $y_* = 0$ profile are approximately two times smaller than that of the uniform strain profile. Also shown in the figure in a dashed line the profile from [7] which still has somewhat lower values in the post-flame zone. The same trend was observed for OH and O profiles which are not presented here. The second choice of y_* produces unsatisfactory results. The steady-state H profile is presented in figure 29. Now the profile is "overstrained" which manifests itself by a lower peak value and a more "squeezed" shape. In the figure the profile is compared with that for the uniform strain case (dashed line). The same trend is observed for other minor species profiles and CO. The major species (except CO) and temperature profiles are reasonably well predicted. The overstrained character of the flame is also demonstrated in figure 30 where the flame location is plotted as a function of time. The steady state flame location of 0.02 cm is much lower that the value of 0.1 cm of [7].

In the case of a highly strained flame we conclude that:

(1) Our model is capable of predicting correctly the profiles of temperature and major species mass fractions in the reaction zone and the post-flame region. The steady-state flame location is overpredicted.

(2) The model predicts correctly the profiles of minor species in the reaction zone. The profiles of the radicals OH, O, H are significantly overpredicted in the post-flame region.

(3) The predictions of the model for the radicals profiles in the post-flame zone can be improved by the introduction of a two-zone strain rate field which provides the correct asymptotic velocity values.

References

1. Petrov, C. and Ghoniem, A.F. , " An Unsteady Strained Flame Model for Turbulent Combustion Simulations", AIAA - 94 - 0776, 32-nd Aerospace Sciences Meeting & Exhibit, January 10-13, 1994, Reno, NV

2. Smooke, M.D. and Giovangigli, V. ,"Formulation of the Premixed and Nonpremixed Test Problems," *Lecture Notes in Physics,* **384**, 1990, pp. 1-29

3. Rutland and Ferziger, "Unsteady Strained Premixed Laminar Flames", *Comb. Sci. Tech.,* **73**, 305, 1990

4. Kee,R.J., Dixon-Lewis, G., Warnatz, J., Coltrin, M.E., Miller,J.A., " A Fortran Computer Code Package for the Evaluation of Gas-Phase, Multicomponent Transport Properties,"*SANDIA Report SAND86-8246,* 1986

5. Kee, R.J., Grcar, J.F., Smooke, M.D., Miller, J.A., " A Fortran Program for Modeling Steady Laminar One-Dimensional Premixed Flames," *SANDIA Report SAND85-8240,* 1985

6. Kee, R.J., Rupley, F.M., Miller,J.A., " Chemkin-II: A Fortran Chemical Kinetics Package for analysis of Gas-Phase Chemical Kinetics," *SANDIA Report SAND89-8009* 1989

7. Rogg, B., " Response and Flamelet Structure of Stretched Premixed Methane-Air Flames,", *Comb. Flame,* **73**, 1988, pp. 45-65
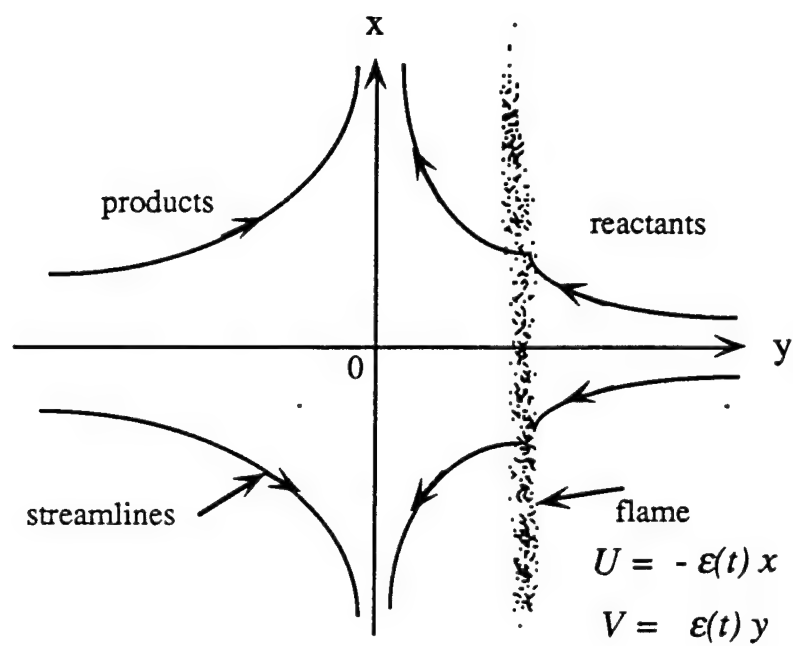
Figure 1. Flame propagation in a stagnation-point flow

$$U = -\varepsilon(t)\,x$$
$$V = \varepsilon(t)\,y$$
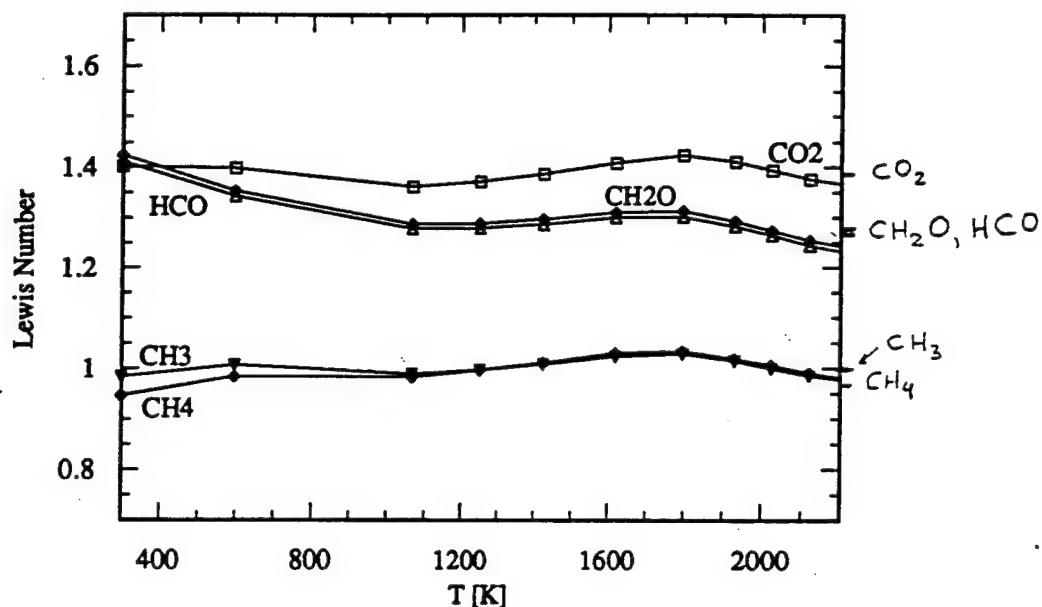
Figure 2a. The detailed transport-"starting" chemical kinetics Lewis numbers of CO_2, CH_2O , CH_4 , CH_3 , HCO as functions of the temperature for an atmospheric pressure, stoichiometric, premixed unstrained methane-air flame. SANDIA Transport Code.
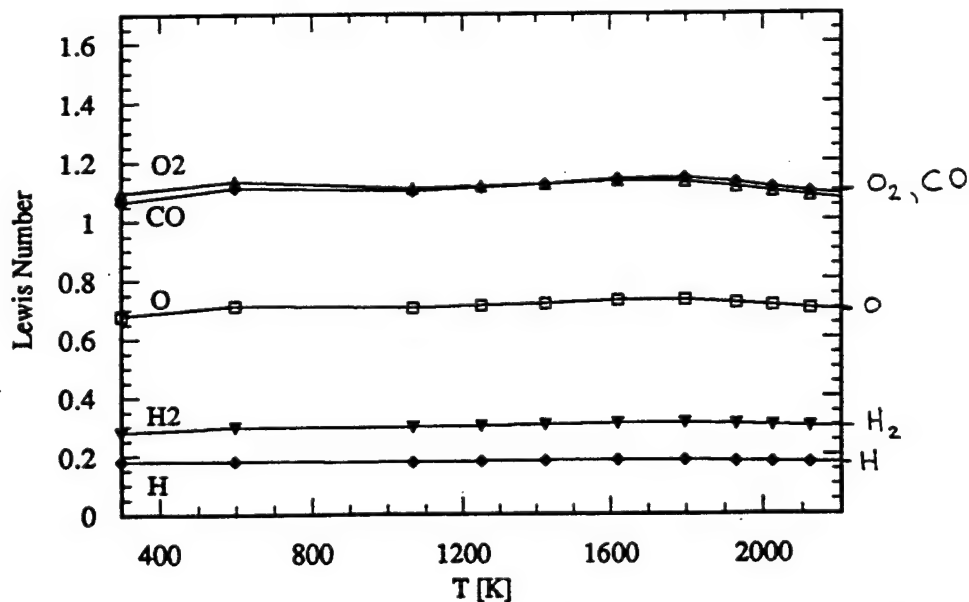
Figure 2c. The detailed transport-"starting" chemical kinetics Lewis numbers of O_2, CO , O , H_2 , H as functions of the temperature for an atmospheric pressure, stoichiometric, premixed unstrained methane-air flame. SANDIA Transport Code. Right-axis values are the results of Smooke [2].
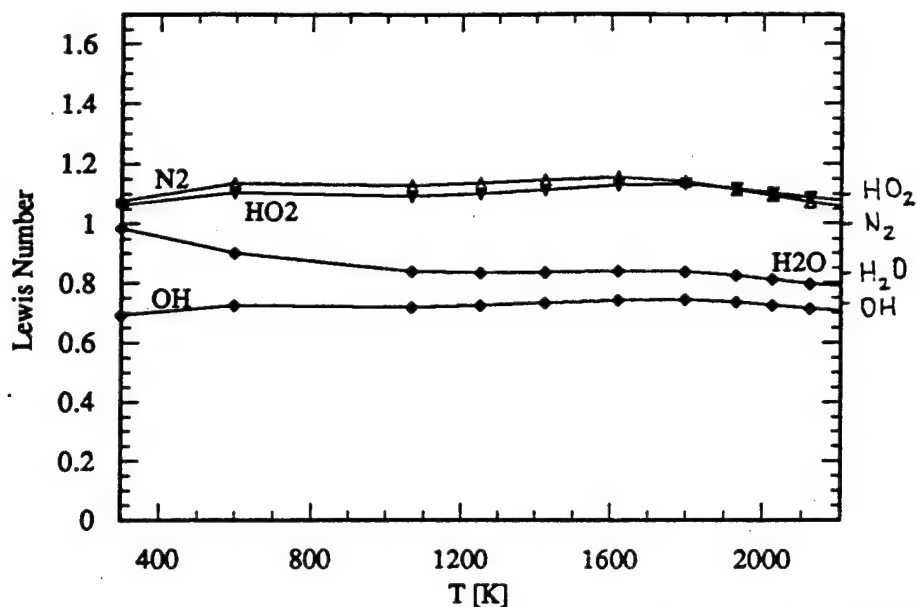
Figure 2d. The detailed transport-"starting" chemical kinetics Lewis numbers of N_2, HO_2, H_2O, OH as functions of the temperature for an atmospheric pressure, stoichiometric, premixed unstrained methane-air flame. SANDIA Transport Code. Right-axis values are the results of Smooke [2].
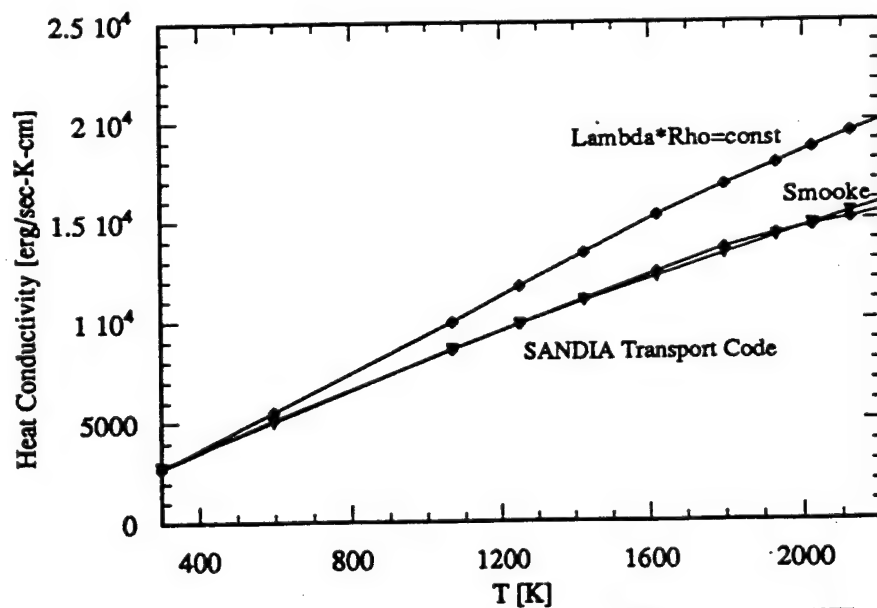
Figure 3. A comparison between the detailed transport-"starting" chemical kinetics value of the heat conductivity coefficient λ, the value obtained from the Smooke correlation $\lambda = 2.58\ 10^{-4} c_p\ (T/T_u)^r$, $r=0.7$, and from the assumption $\lambda \rho = const = \lambda_u\ \rho_u$ for an atmospheric pressure, stoichiometric, premixed unstrained methane-air flame.
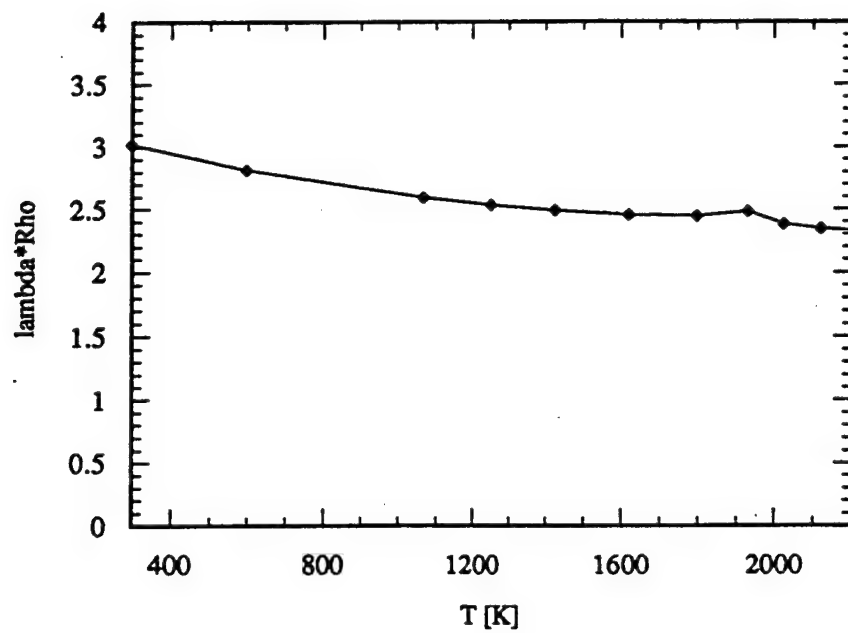
Figure 4. The product $\lambda \rho$ as a function of the temperature for an atmospheric pressure, stoichiometric, premixed unstrained methane-air flame. SANDIA Transport Code results.
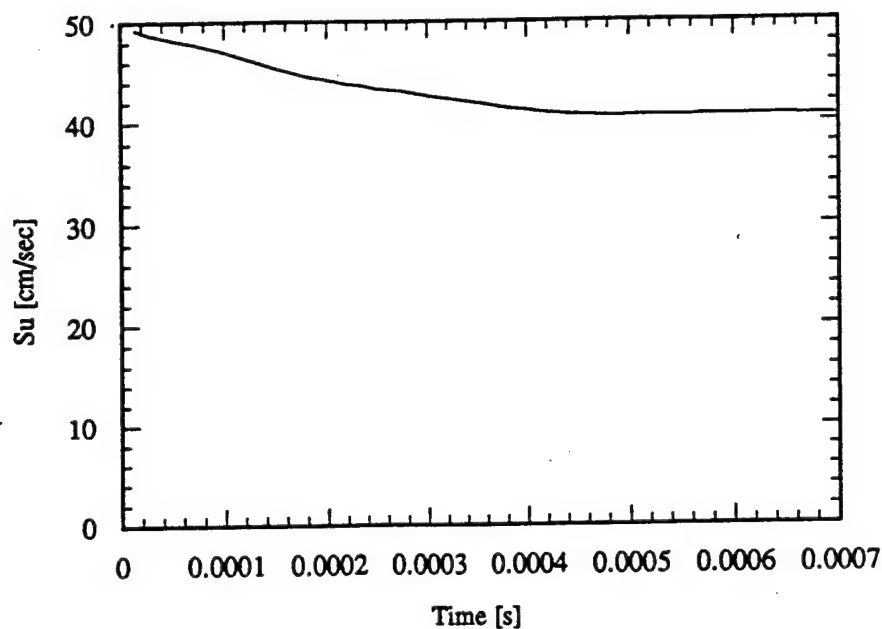
Figure 5a. The laminar burning velocity of a freely-propagating, premixed, atmospheric pressure, stoichiometric flame as a function of time. Transport model $\lambda \rho = const = \lambda_u \rho_u$, the "starting" chemical kinetics mechanism. Strain rate $\varepsilon = 10^{-4} s^{-1}$
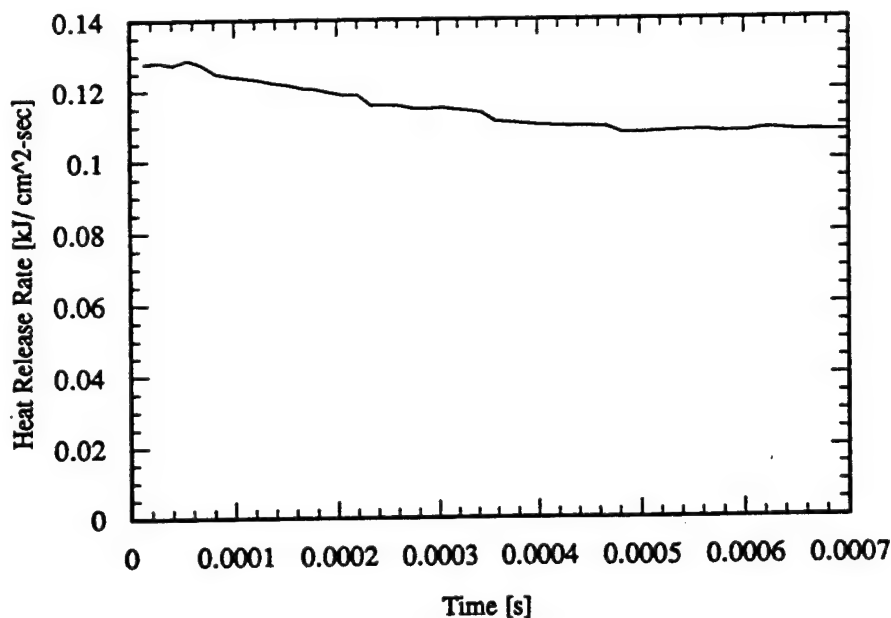
Figure 5b. The heat release rate of a freely-propagating, premixed, atmospheric pressure, stoichiometric flame as a function of time. Transport model $\lambda \rho = const = \lambda_u \rho_u$, the "starting" chemical kinetics mechanism. Strain rate $\varepsilon = 10^{-4} s^{-1}$
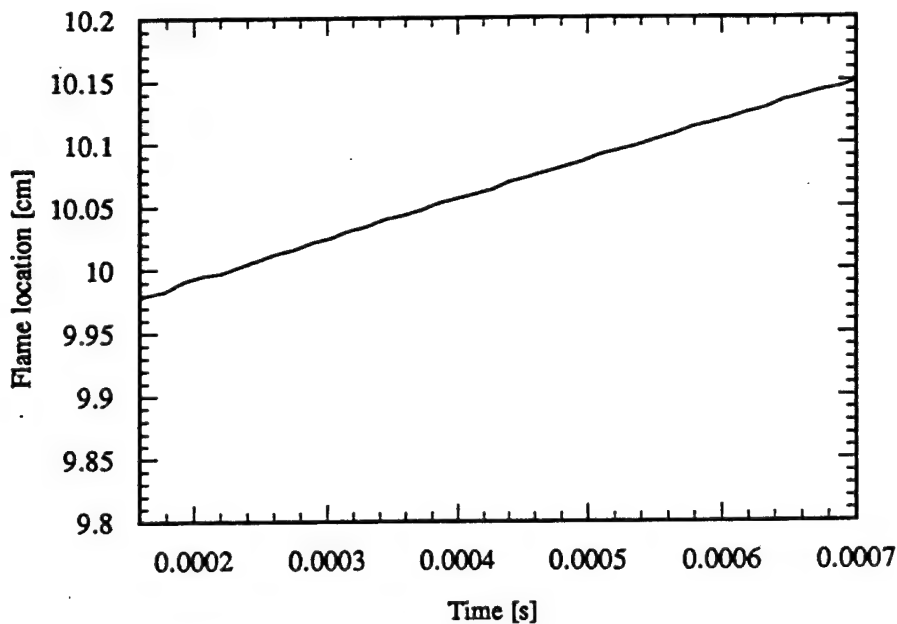
Figure 5c. The flame location of a freely-propagating, premixed, atmospheric pressure, stoichiometric flame as a function of time. Transport model $\lambda \rho = const = \lambda_u \rho_u$, the "starting" chemical kinetics mechanism. Strain rate $\varepsilon = 10^{-4} \ s^{-1}$
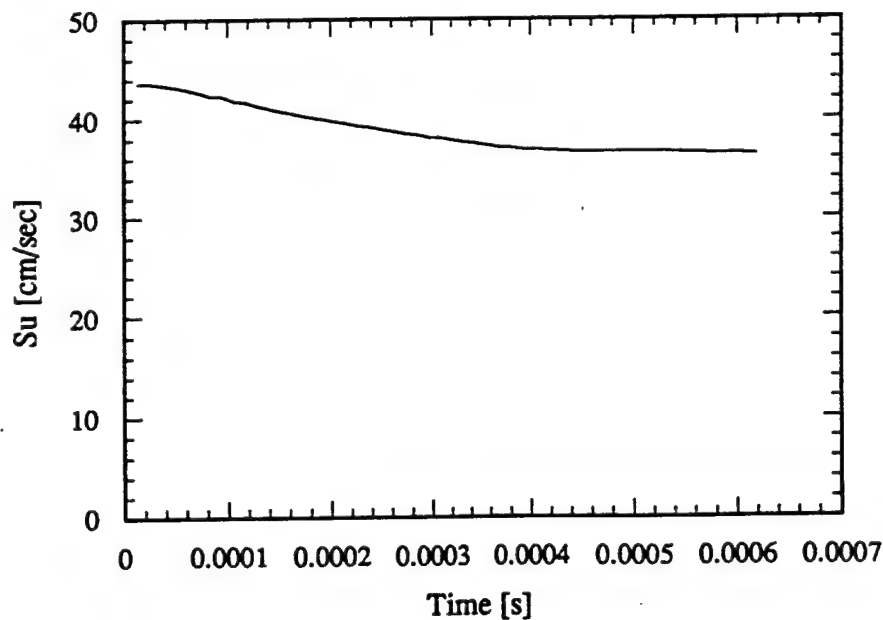
Figure 6a. The laminar burning velocity of a freely-propagating, premixed, atmospheric pressure, stoichiometric flame as a function of time. Transport model $\lambda = 2.58 \ 10^{-4} c_p \ (T/T_u)'$, the "starting" chemical kinetics mechanism. Strain rate $\varepsilon = 10^{-4} \ s^{-1}$
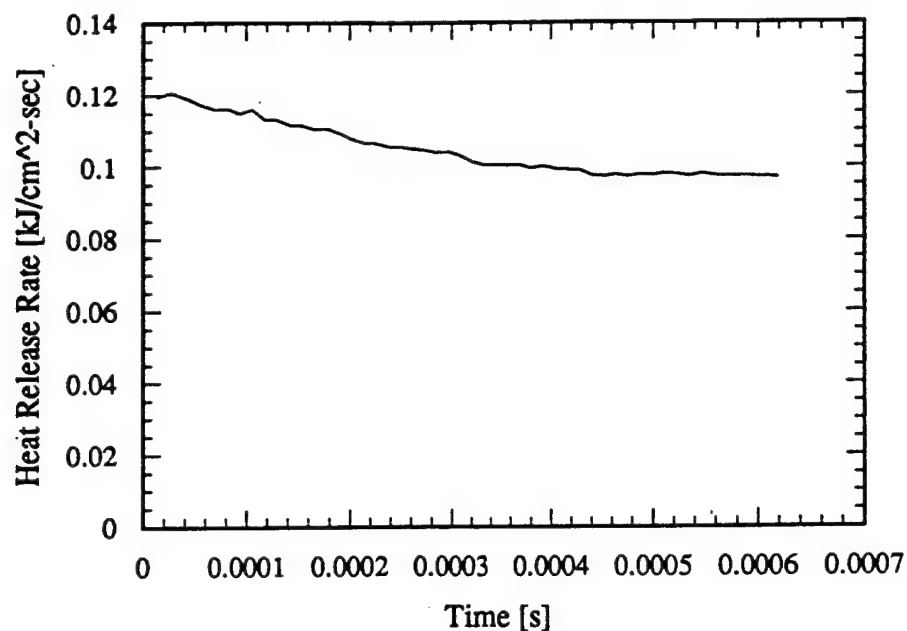
Figure 6b. The heat release rate of a freely-propagating, premixed, atmospheric pressure, stoichiometric flame as a function of time. Transport model $\lambda = 2.58 \ 10^{-4} c_p \ (T/T_u)^r$, $r=0.7$, the "starting" chemical kinetics mechanism. Strain rate $\varepsilon = 10^{-4} \ sec^{-1}$.
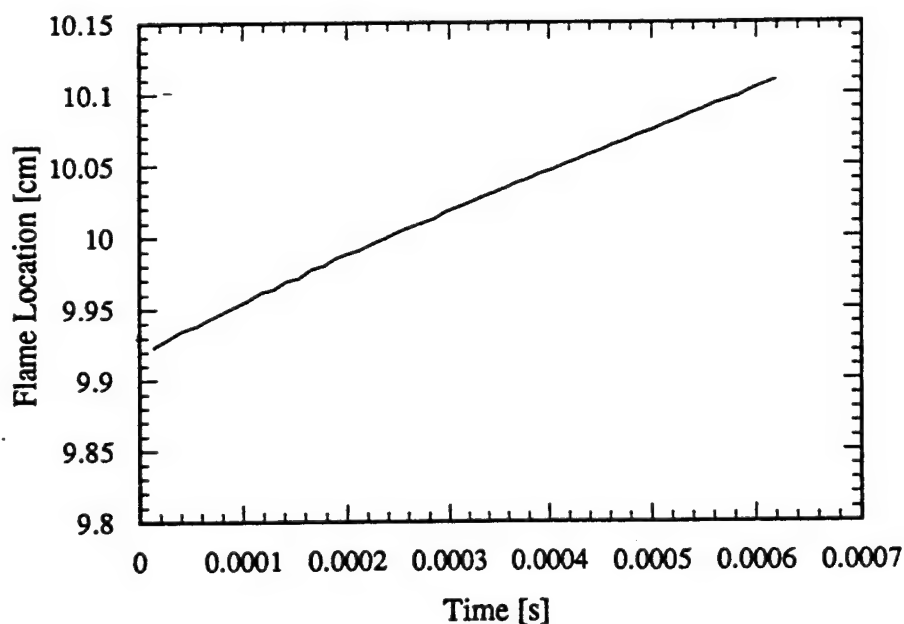
Figure 6c. The flame location of a freely-propagating, premixed, atmospheric pressure, stoichiometric flame as a function of time. Transport model $\lambda = 2.58 \ 10^{-4} c_p \ (T/T_u)^r$, $r=0.7$, the "starting" chemical kinetics mechanism. Strain rate $\varepsilon = 10^{-4} \ s^{-1}$
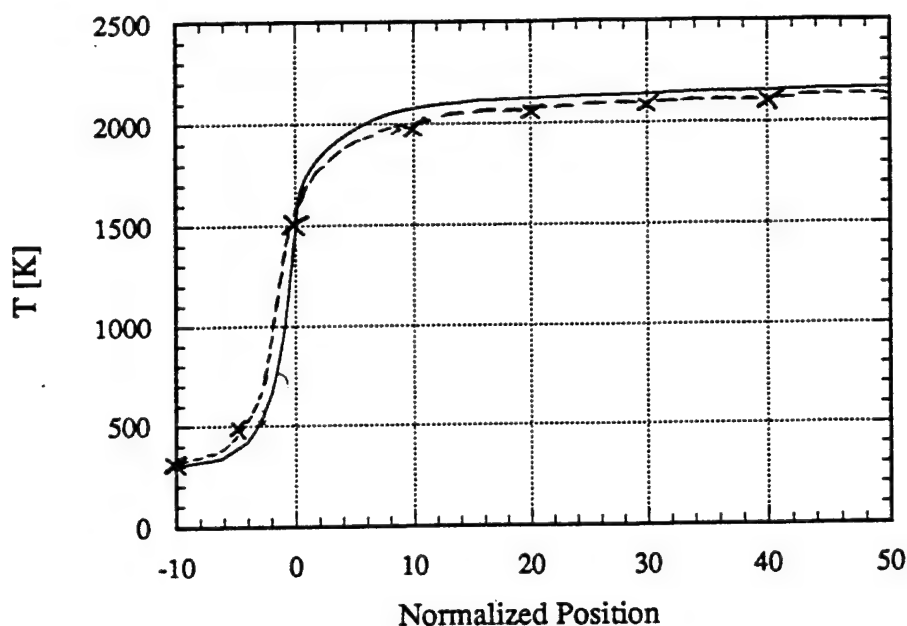
Figure 7. A comparison between the computed temperature profiles as a function of the normalized distance for an atmospheric pressure, stoichiometric, methane-air flame employing a $\lambda = 2.58\ 10^{-4} c_p\ (T/\ T_u)^r$ transport model and the "starting" chemical kinetics mechanism (solid line); and the profiles obtained by Smooke [2] (dashed line).
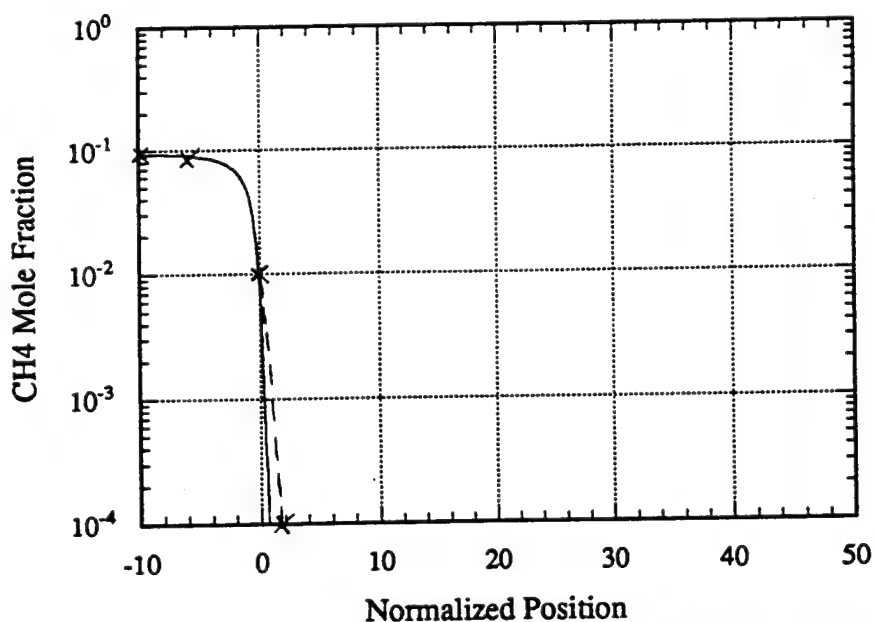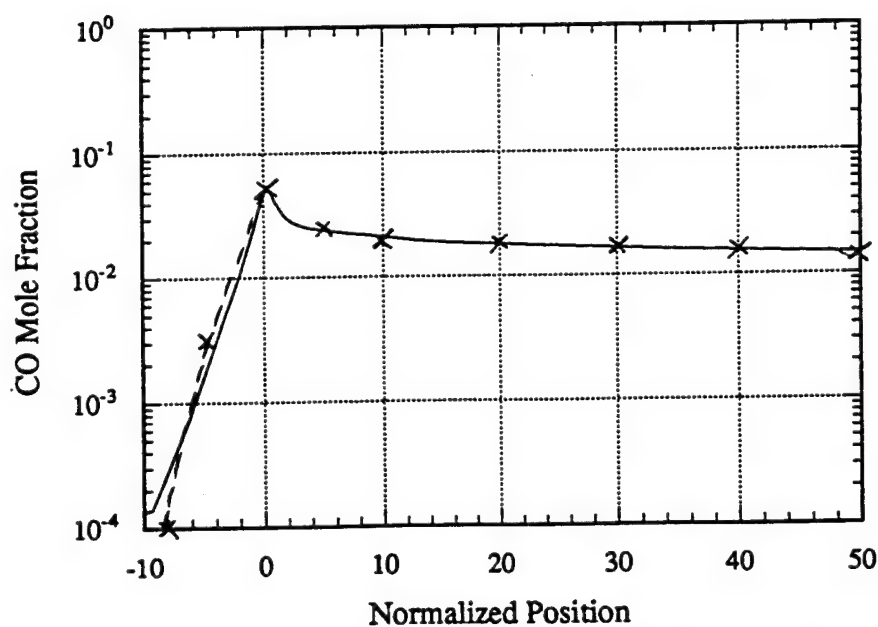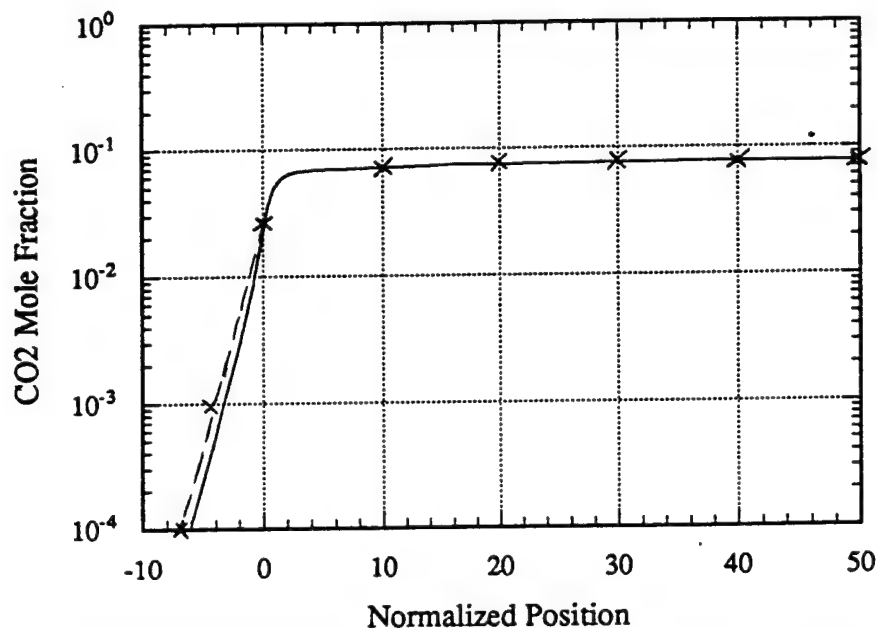

Figure 8. A comparison between the computed CH_4 mole fraction profiles as a function of the normalized distance for an atmospheric pressure, stoichiometric, methane-air flame employing a $\lambda = 2.58\ 10^{-4} c_p\ (T/\ T_u)^r$ transport model and the "starting" chemical kinetics mechanism (solid line); and the profiles obtained by Smooke [2] (dashed line).
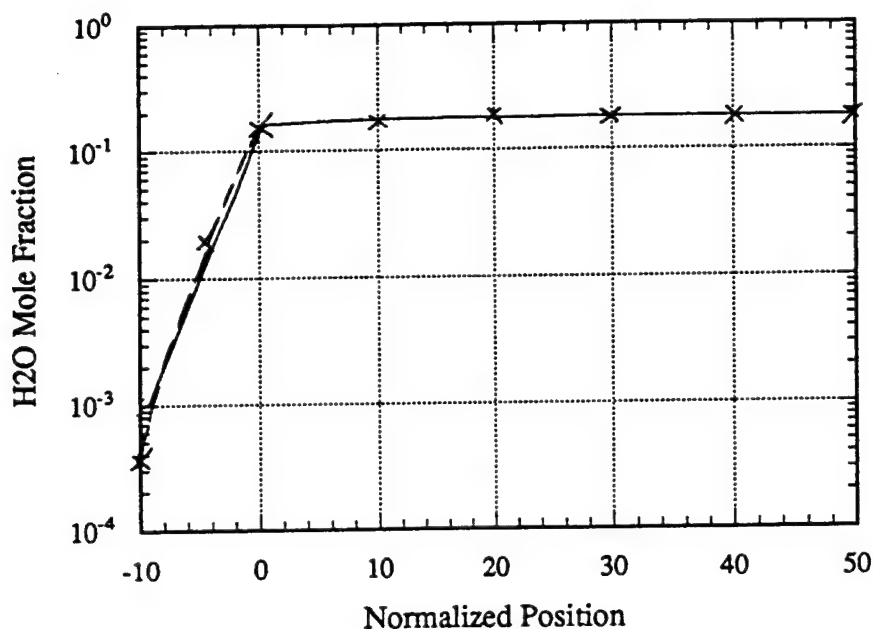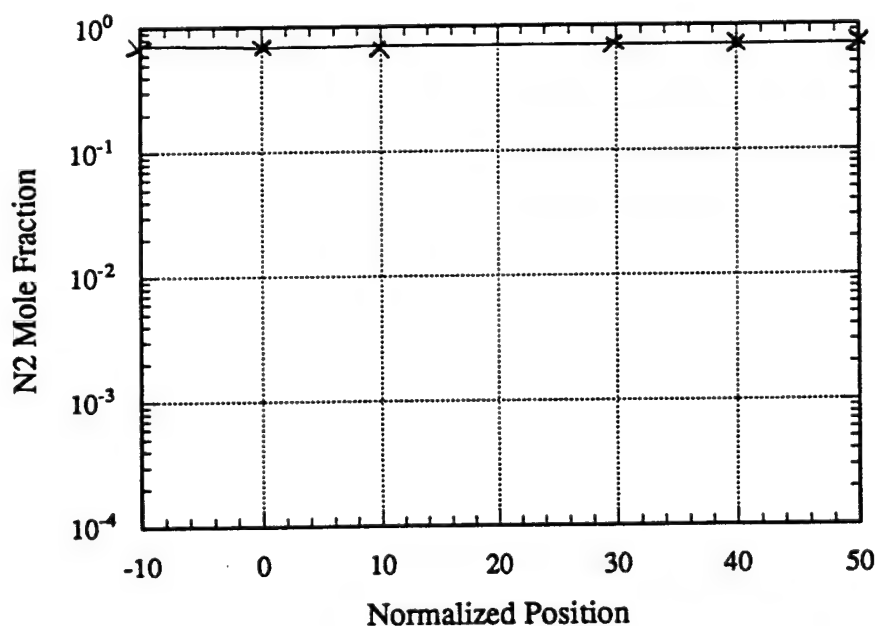
Figure 9. A comparison between the computed H_2O mole fraction profiles as a function of the normalized distance for an atmospheric pressure, stoichiometric, methane-air flame employing a $\lambda = 2.58 \ 10^{-4} c_p \ (T/ T_u)^r$ transport model and the "starting" chemical kinetics mechanism (solid line); and the profiles obtained by Smooke [2] (dashed line).
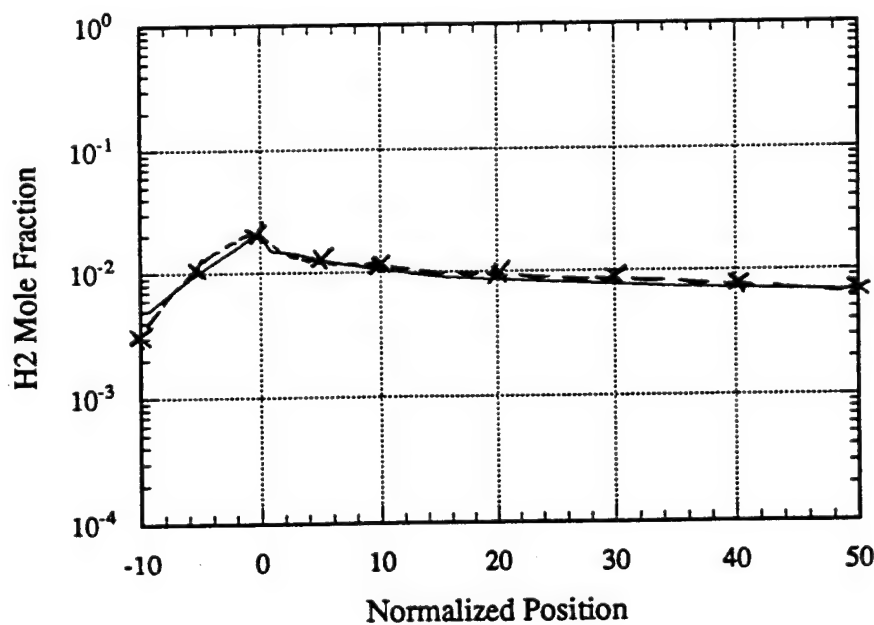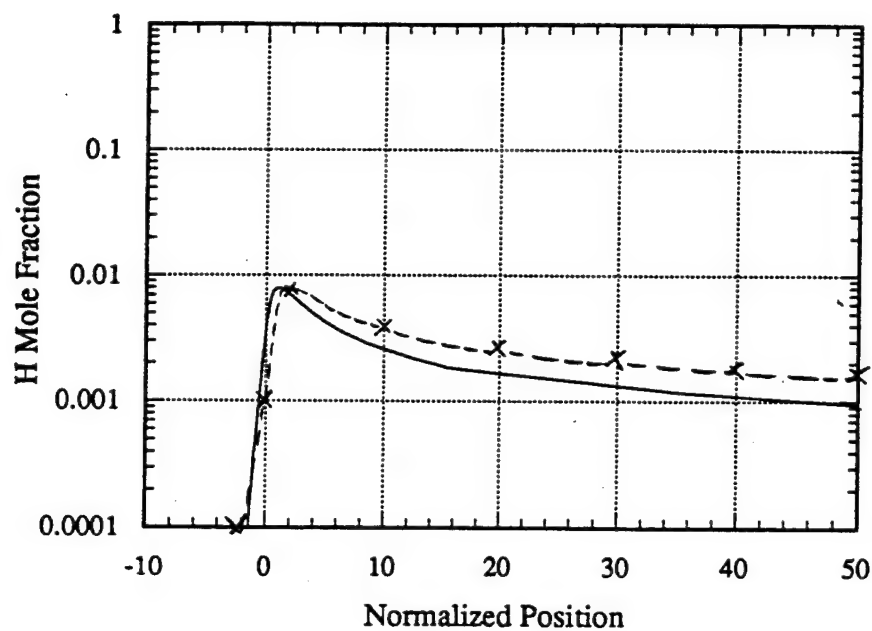

Figure 10. A comparison between the computed H_2 mole fraction profiles as a function of the normalized distance for an atmospheric pressure, stoichiometric, methane-air flame employing a $\lambda = 2.58 \ 10^{-4} c_p \ (T/ T_u)^r$ transport model and the "starting" chemical kinetics mechanism (solid line); and the profiles obtained by Smooke [2] (dashed line).
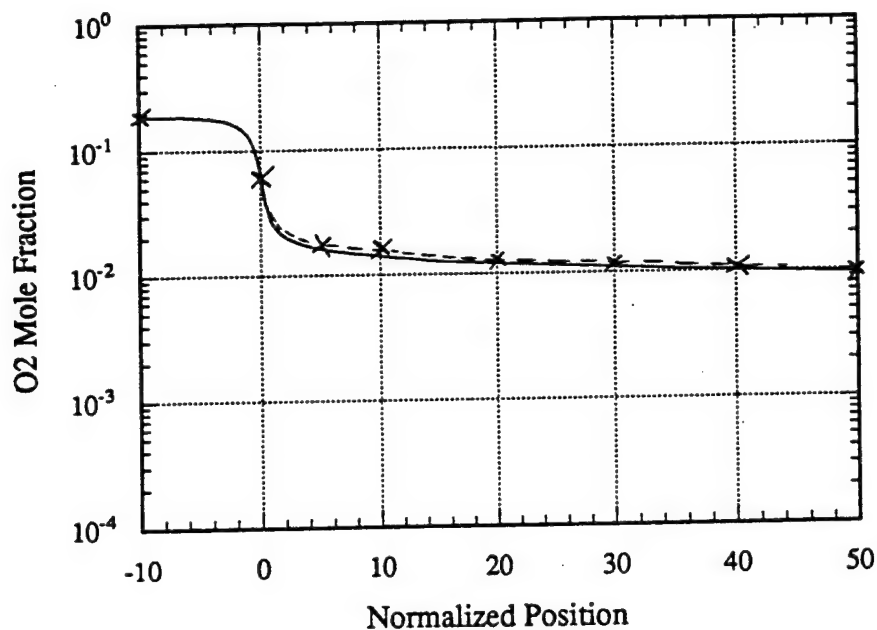
Figure 11. A comparison between the computed O_2 mole fraction profiles as a function of the normalized distance for an atmospheric pressure, stoichiometric, methane-air flame employing a $\lambda = 2.58 \ 10^{-4} c_p \ (T/ T_u)'$ transport model and the "starting" chemical kinetics mechanism (solid line); and the profiles obtained by Smooke [2] (dashed line).


Figure 12. A comparison between the computed CO mole fraction profiles as a function of the normalized distance for an atmospheric pressure, stoichiometric, methane-air flame employing a $\lambda = 2.58 \ 10^{-4} c_p \ (T/ T_u)'$ transport model and the "starting" chemical kinetics mechanism (solid line); and the profiles obtained by Smooke [2] (dashed line).

Figure 13. A comparison between the computed CO_2 mole fraction profiles as a function of the normalized distance for an atmospheric pressure, stoichiometric, methane-air flame employing a $\lambda = 2.58\ 10^{-4} c_p\ (T/\ T_u)'$ transport model and the "starting" chemical kinetics mechanism (solid line); and the profiles obtained by Smooke [2] (dashed line).

Figure 14. A comparison between the computed N_2 mole fraction profiles as a function of the normalized distance for an atmospheric pressure, stoichiometric, methane-air flame employing a $\lambda = 2.58\ 10^{-4} c_p\ (T/\ T_u)'$ transport model and the "starting" chemical kinetics mechanism (solid line); and the profiles obtained by Smooke [2] (dashed line).

Figure 15. A comparison between the computed H mole fraction profiles as a function of the normalized distance for an atmospheric pressure, stoichiometric, methane-air flame employing a $\lambda = 2.58 \ 10^{-4} c_p \ (T/T_u)'$ transport model and the "starting" chemical kinetics mechanism (solid line); and the profiles obtained by Smooke [2] (dashed line).
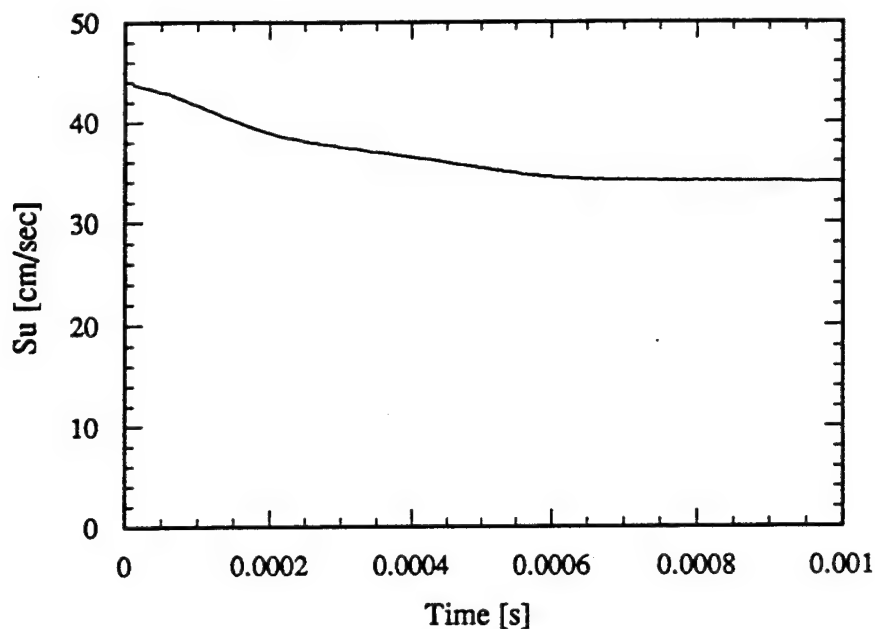
Figure 16a. The laminar burning velocity of a strained, premixed, atmospheric pressure, stoichiometric flame as a function of time. Transport model $\lambda = 2.58\ 10^{-4}c_p\ (T/T_u)^r$, $r=0.7$, the "starting" chemical kinetics mechanism. Strain rate $\varepsilon = 10^3\ s^{-1}$
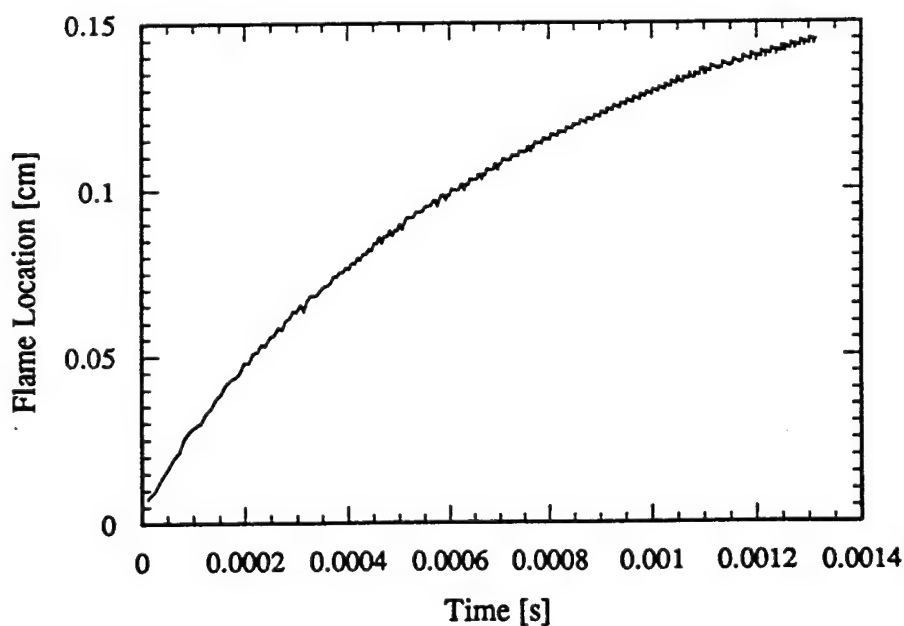
Figure 16b. The flame location of a strained, premixed, atmospheric pressure, stoichiometric flame as a function of time. Transport model $\lambda = 2.58\ 10^{-4}c_p\ (T/T_u)^r$, $r=0.7$, the "starting" chemical kinetics mechanism. Strain rate $\varepsilon = 10^3\ s^{-1}$

43
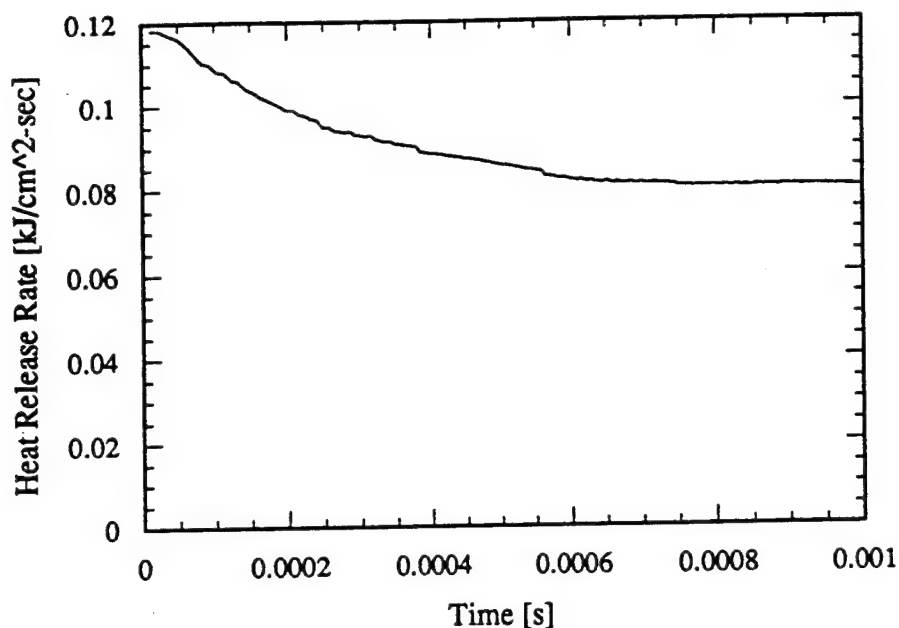
Figure 16c. The heat release rate of a strained, premixed, atmospheric pressure, stoichiometric flame as a function of time. Transport model $\lambda = 2.58 \ 10^{-4} c_p \ (T/T_u)^r$, $r=0.7$, the "starting" chemical kinetics mechanism. Strain rate $\varepsilon = 10^3 \ s^{-1}$
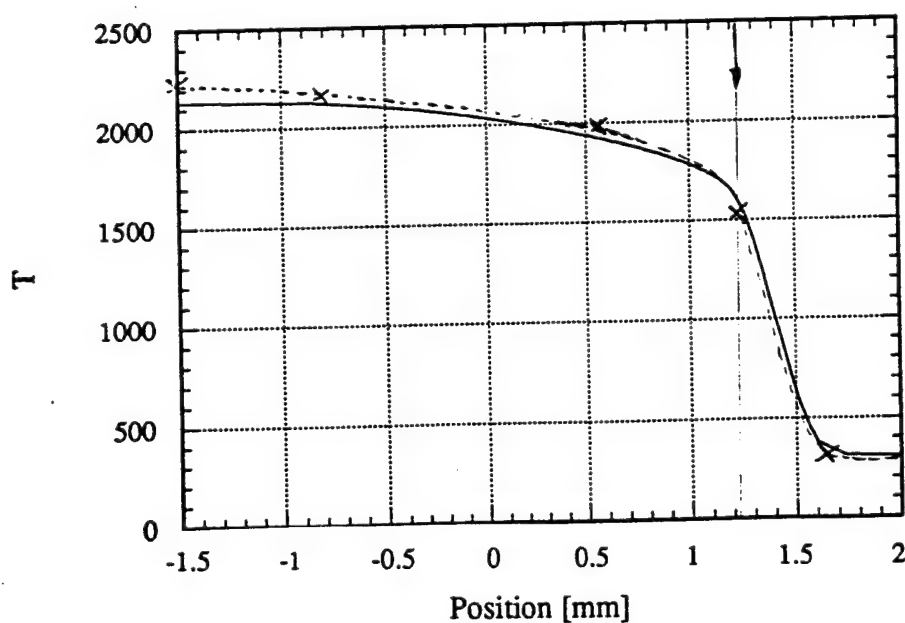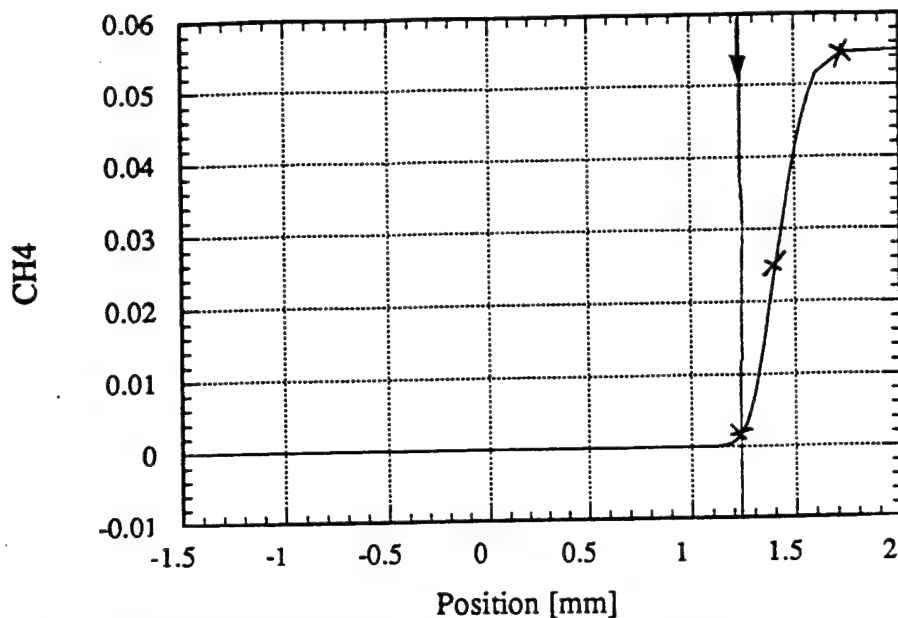

Figure 17. A comparison between the computed temperature profile for a highly strained atmospheric pressure, stoichiometric, methane-air flame employing a $\lambda = 2.58 \ 10^{-4} c_p \ (T/T_u)^r$ transport model and the "starting" chemistry mechanism (solid line) and the profile of Rogg [7] (dashed line). $\varepsilon = 10^3 \ s^{-1}$. The vertical arrow indicates the location of maximum fuel-consumption rate.
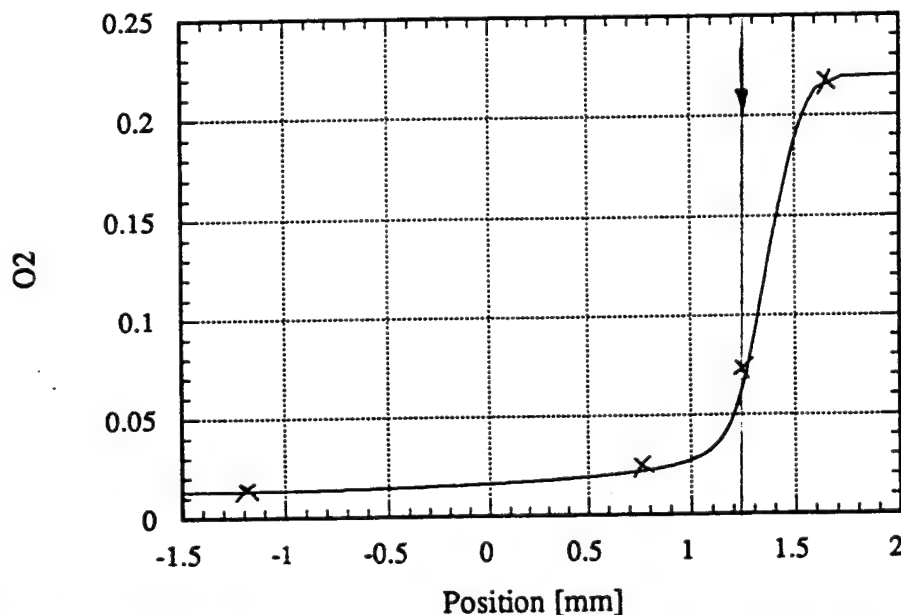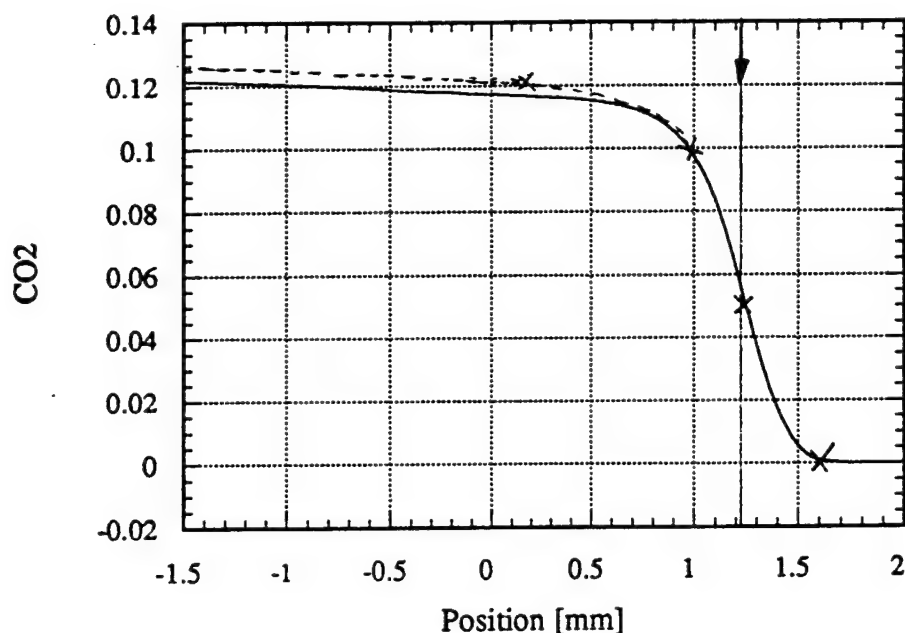
44

Figure 18. A comparison between the computed CH_4 mass fraction profile for a highly strained atmospheric pressure, stoichiometric, methane-air flame employing a $\lambda = 2.58 \ 10^{-4} c_p \ (T/T_u)^r$ transport model and the "starting" chemistry mechanism (solid line) and the profile of Rogg [7] (dashed line). $\varepsilon = 10^3 \ s^{-1}$. The vertical arrow indicates the location of maximum fuel-consumption rate.

Figure 19. A comparison between the computed O_2 mass fraction profile for a highly strained atmospheric pressure, stoichiometric, methane-air flame employing a $\lambda = 2.58 \ 10^{-4} c_p \ (T/T_u)^r$ transport model and the "starting" chemistry mechanism (solid line) and the profile of Rogg [7] (dashed line). $\varepsilon = 10^3 \ s^{-1}$. The vertical arrow indicates the location of maximum fuel-consumption rate.
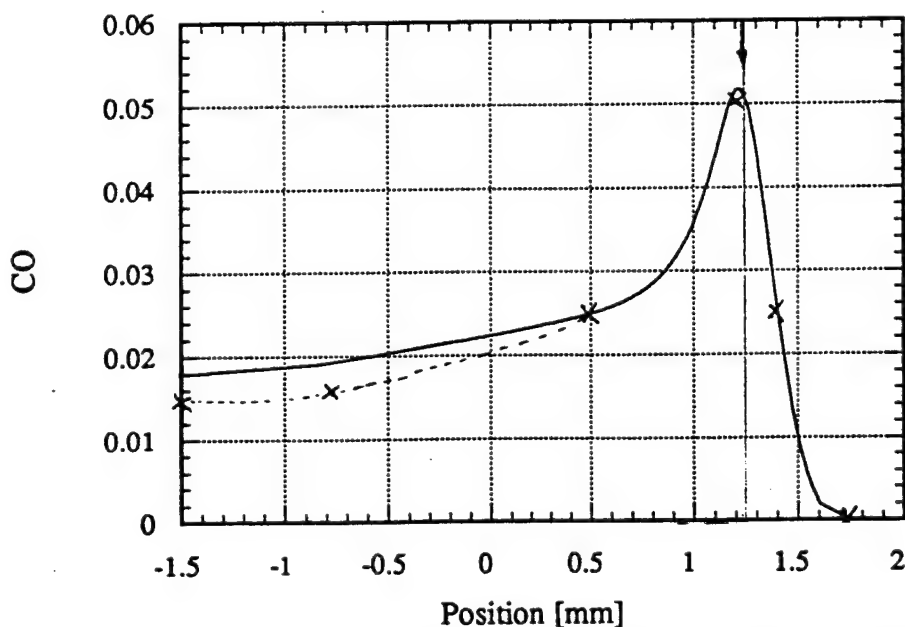
45

Figure 20. A comparison between the computed CO_2 mass fraction profile for a highly strained atmospheric pressure, stoichiometric, methane-air flame employing a $\lambda = 2.58 \; 10^{-4} c_p \; (T/T_u)'$ transport model and the "starting" chemistry mechanism (solid line) and the profile of Rogg [7] (dashed line). $\varepsilon = 10^3 \; s^{-1}$. The vertical arrow indicates the location of maximum fuel-consumption rate.
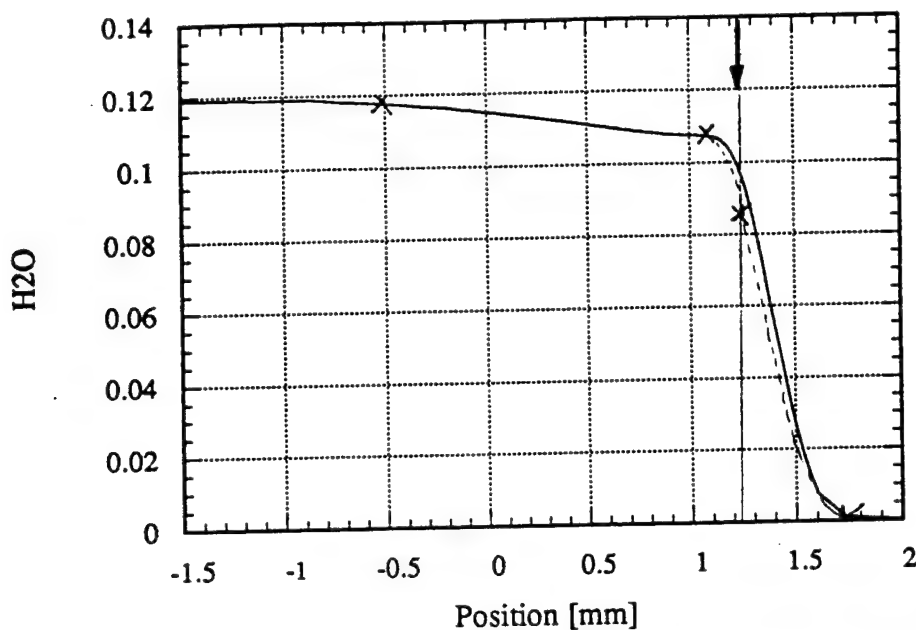

Figure 21. A comparison between the computed CO mass fraction profile for a highly strained atmospheric pressure, stoichiometric, methane-air flame employing a $\lambda = 2.58 \; 10^{-4} c_p \; (T/T_u)'$ transport model and the "starting" chemistry mechanism (solid line) and the profile of Rogg [7] (dashed line). $\varepsilon = 10^3 \; s^{-1}$. The vertical arrow indicates the location of maximum fuel-consumption rate.
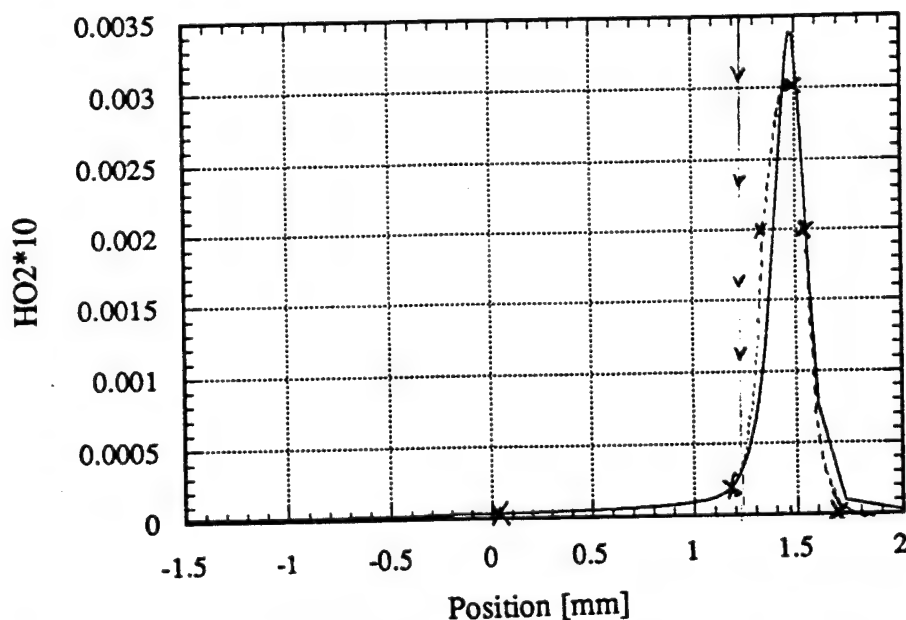
46

Figure 22. A comparison between the computed H_2O mass fraction profile for a highly strained atmospheric pressure, stoichiometric, methane-air flame employing a $\lambda = 2.58 \; 10^{-4} c_p \; (T/T_u)^r$ transport model and the "starting" chemistry mechanism (solid line) and the profile of Rogg [7] (dashed line). $\varepsilon = 10^{3} \; s^{-1}$. The vertical arrow indicates the location of maximum fuel-consumption rate.
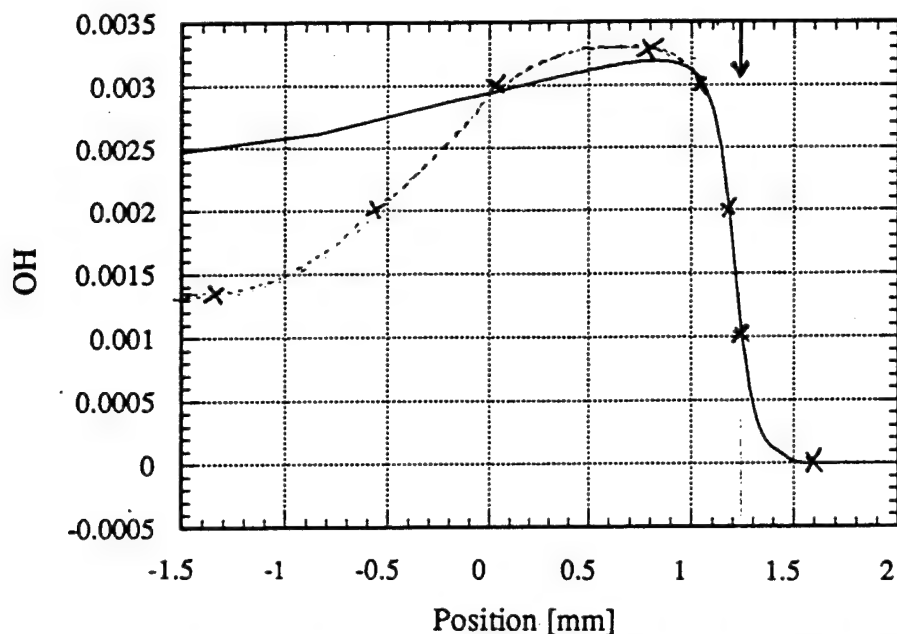

Figure 23. A comparison between the computed HO_2 mass fraction profile for a highly strained atmospheric pressure, stoichiometric, methane-air flame employing a $\lambda = 2.58 \; 10^{-4} c_p \; (T/T_u)^r$ transport model and the "starting" chemistry mechanism (solid line) and the profile of Rogg [7] (dashed line). $\varepsilon = 10^{3} \; s^{-1}$. The vertical arrow indicates the location of maximum fuel-consumption rate.

47

Figure 24. A comparison between the computed *OH* mass fraction profile for a highly strained atmospheric pressure, stoichiometric, methane-air flame employing a $\lambda = 2.58 \ 10^{-4} c_p \ (T/T_u)^r$ transport model and the "starting" chemistry mechanism (solid line) and the profile of Rogg [7] (dashed line). $\varepsilon = 10^{3} \ s^{-1}$. The vertical arrow indicates the location of maximum fuel-consumption rate.
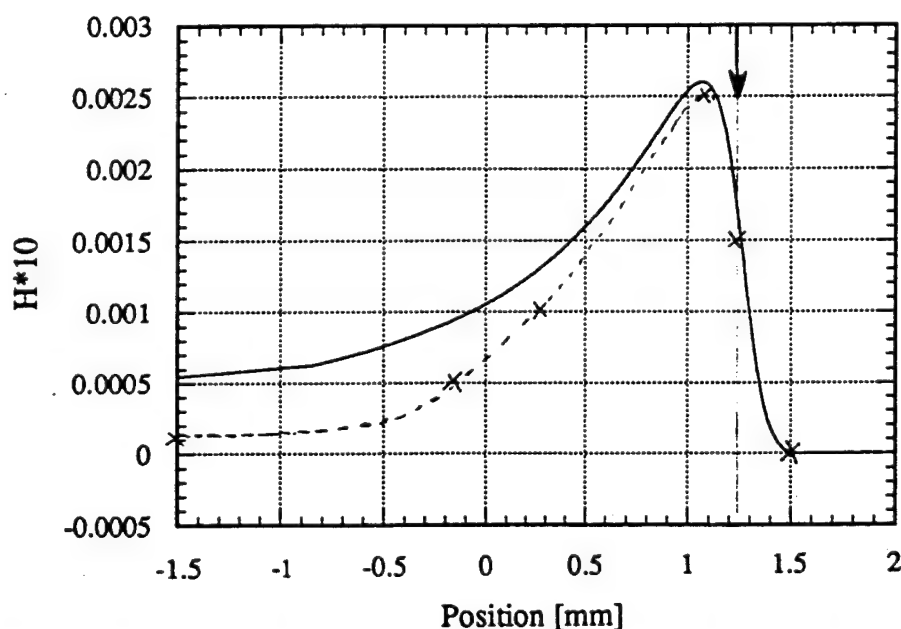

Figure 25. A comparison between the computed *H* mass fraction profile for a highly strained atmospheric pressure, stoichiometric, methane-air flame employing a $\lambda = 2.58 \ 10^{-4} c_p \ (T/T_u)^r$ transport model and the "starting" chemistry mechanism (solid line) and the profile of Rogg [7] (dashed line). $\varepsilon = 10^{3} \ s^{-1}$. The vertical arrow indicates the location of maximum fuel-consumption rate.
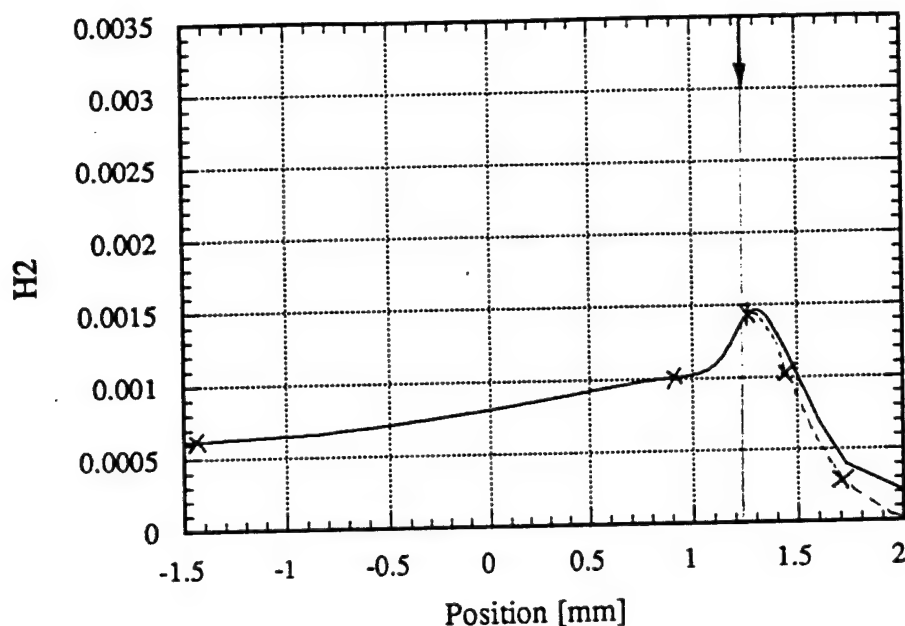
Figure 26. A comparison between the computed H_2 mass fraction profile for a highly strained atmospheric pressure, stoichiometric, methane-air flame employing a $\lambda = 2.58\ 10^{-4} c_p\ (T/T_u)^r$ transport model and the "starting" chemistry mechanism (solid line) and the profile of Rogg [7] (dashed line). $\varepsilon = 10^3\ s^{-1}$. The vertical arrow indicates the location of maximum fuel-consumption rate.
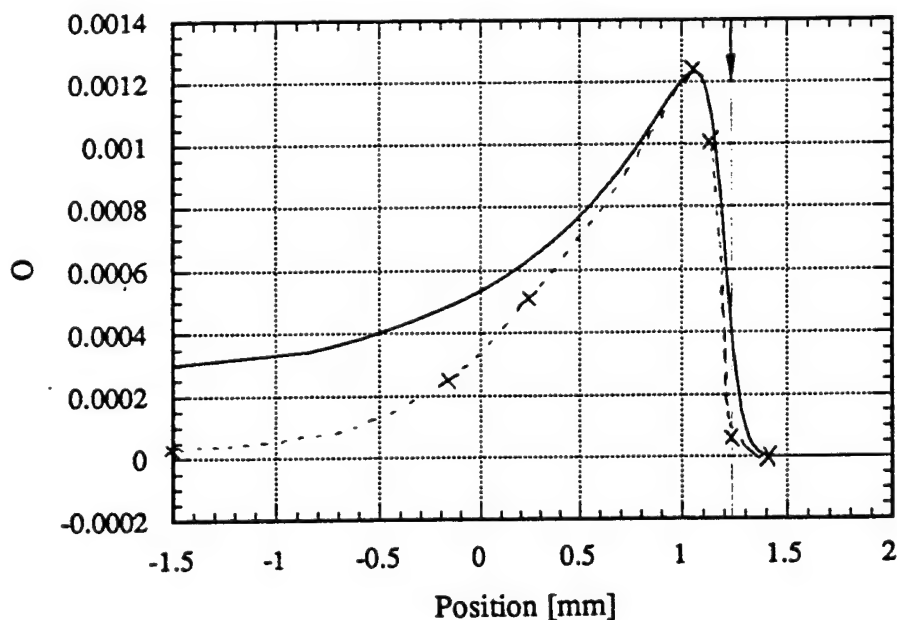

Figure 27. A comparison between the computed O mass fraction profile for a highly strained atmospheric pressure, stoichiometric, methane-air flame employing a $\lambda = 2.58\ 10^{-4} c_p\ (T/T_u)^r$ transport model and the "starting" chemistry mechanism (solid line) and the profile of Rogg [7] (dashed line). $\varepsilon = 10^3\ s^{-1}$. The vertical arrow indicates the location of maximum fuel-consumption rate.
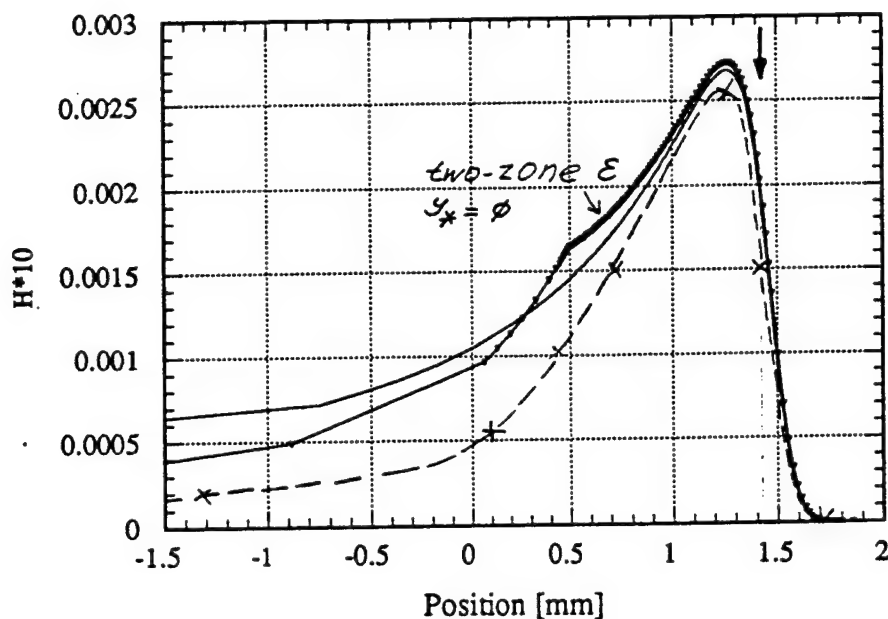
Figure 28. A comparison between the computed O mass fraction profile for a highly strained atmospheric pressure, stoichiometric, methane-air flame employing a $\lambda = 2.58\ 10^{-4} c_p\ (T/T_u)^r$ transport model and the "starting" chemistry mechanism (solid line) and the profile of Rogg [7] (dashed line). $\varepsilon = 10^3\ s^{-1}$. The vertical arrow indicates the location of maximum fuel-consumption rate.
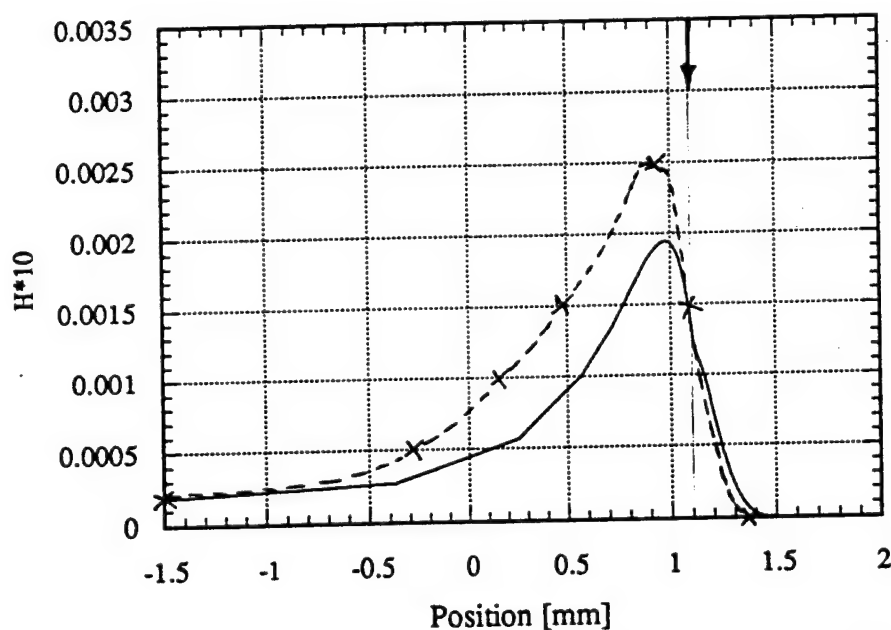

Figure 29. A comparison among the computed H mass fraction profile for a highly strained atmospheric pressure, stoichiometric, methane-air flame employing a $\lambda = 2.58\ 10^{-4} c_p\ (T/T_u)^r$ transport model, the "starting" chemistry mechanism and two-zone external strain field with $y_* = 0$ (dot-solid line), the profile obtained for the constant external strain (solid line), and the profile of Rogg [7] (dashed line). $\varepsilon = 10^3\ s^{-1}$. The vertical arrow indicates the location of maximum fuel-consumption rate.
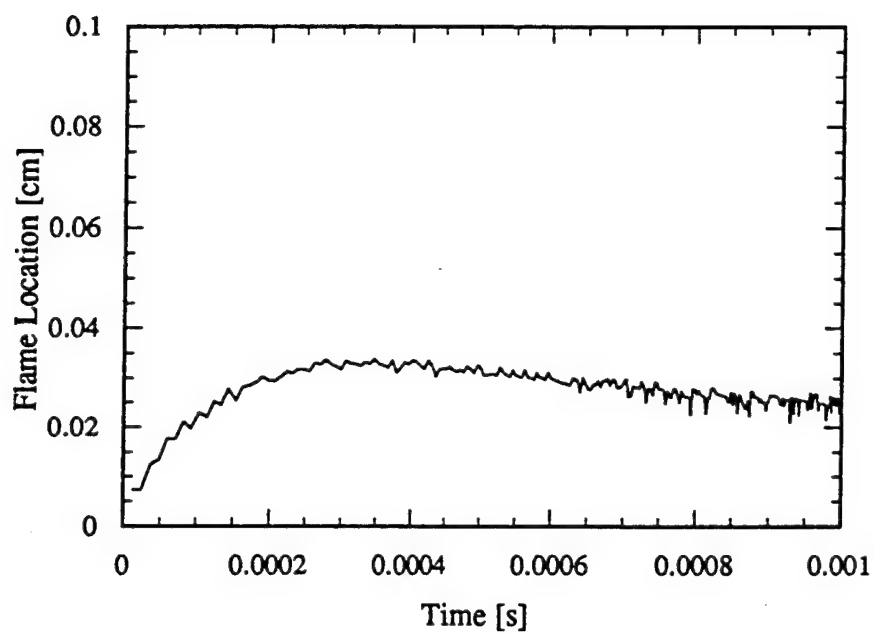
50

Figure 30. The flame location of a highly strained, premixed, atmospheric pressure, stoichiometric flame as a function of time. Transport model $\lambda = 2.58 \ 10^{-4} c_p \ (T/T_u)^r$, the "starting" chemical kinetics mechanism; two-zone strain, $y_* = y_f(t)$. Strain rate $\varepsilon_u = 10^3 \ s^{-1}$.

APPENDIX II

AIAA-94-0777

Dynamics Of Reacting Shear Flows; Effects Of Exothermicity And Forcing

M.C. Soteriou and A.F. Ghoniem
Massachusetts Institute of Technology
Cambridge, MA 02139

32nd Aerospace Sciences Meeting & Exhibit
January 10-13, 1994 / Reno, NV

DYNAMICS OF REACTING SHEAR FLOWS; EFFECTS OF EXOTHERMICITY AND FORCING

Marios C. Soteriou[1] and Ahmed F. Ghoniem[2]
Massachusetts Institute of Technology
Cambridge, MA 02139

ABSTRACT

The effects of combustion heat release on a spatially-developing, high Reynolds number, non-premixed, reacting shear-layer are investigated under both forced and unforced inlet conditions using the results of two-dimensional numerical simulations. Combustion is modeled using an infinite reaction speed model. The numerical solution is obtained using the Lagrangian transport-element method. Results indicate that in an unforced flow, heat release decreases the size of the mixing region and the amount of product formed over most of the domain via: (i) a delay of the onset of the flow instability and (ii) a reduction in the overall spinning and an apparent suppression of the interactions of the eddies. With external forcing, which promotes early destabilization of the layer, similar trends of mixing and combustion reduction are experienced, as manifested by reduced eddy spinning, which keeps the eddy major axis aligned with the flow direction, and alteration of the eddy pairing interaction to tearing of smaller eddies by their larger neighbors. Volumetric (area) expansion weakens the vorticity field and is responsible for delaying the onset of the instability in the unforced case, the reduction of the spinning of the eddies in both cases and the alignment of the major axis of the downstream larger eddy with the flow direction in the forced case. The suppression of eddy pairing is attributed to the presence of baroclinic vorticity generation.

I. INTRODUCTION

Turbulent reacting shear layers represent a generic and relatively simple model of many combustion systems. They are set up via the amplification of the instability of the shear region between two reacting fluids originally moving at different velocities, are essentially two-dimensional at their early stages, and are dominated by large-scale vortical structures [1]. These structures are the regions where reactants mix and burn and are, hence, of fundamental importance to the combustion process.

The effects of the combustion-heat release on a shear layer have been of interest but have only been investigated recently. Experimental studies [1-3] indicate that heat release reduces the growth of the shear layer and diminishes the rates of mixing and burning. Numerical studies, mostly restricted to the idealized temporally-evolving flow have been carried out for

both non-premixed [4,5] and premixed [6] layers and have, to some extend, been able to reproduce this behavior. However, due to the idealized nature of the temporal model, which is mainly a consequence of the introduction of periodic boundary conditions in the streamwise flow direction, the conclusions drawn from these studies must be treated with caution [7,8]. The non-premixed calculations, which are more relevant to this work assumed a constant volume combustion process and were carried out under an infinite activation temperature model and at quite low Damkohler number.

Numerical studies of spatially evolving reacting shear layers [e.g. 7,9,10], on the other hand, have been restricted to cases where the effects of combustion on the flowfield are negligibly small. An exception is presented in Ref.[11] where a large eddy simulation of an externally forced, compressible shear layer with variable transport properties and Arrhenius kinetics was performed. However, combustion-heat release and the activation temperature where kept low. Nevertheless, this work was instrumental in showing that the effect of the temperature-dependent transport properties is small.

In this paper the effects of combustion heat release on a spatially evolving reacting shear layer are numerically investigated at high values of heat release and for both forced and unforced inlet conditions using a high resolution numerical scheme. An advantage of such an approach is that it enables an assessment of the effect of heat release on the initial instability of the flow as well as on the dynamics downstream. An infinite reaction speed model is used to describe the reacting field. This model was shown, in earlier work [8,12], to adequately predict the effect of heat release on the flowfield when combustion is fast compared to the flow. The unforced layer results are presented first. This is done in terms of both the instantaneous and average flow dynamics. The forced layer results are subsequently presented in a similar fashion. Finally, explanations of the flow features are proposed based on the vorticity dynamics and the related convolution of the flame.

II. FORMULATION

The motion of a two-dimensional, high Reynolds number, reacting flow is considered. Compressibility effects are allowed under the low Mach number assumption [4]. The effects of gravity are neglected. All species behave as perfect gases with equal molar masses and constant and equal diffusivities and specific heats. Combustion occurs via a single step, irreversible, mole preserving, infinite rate reaction.

While the infinite reaction rate model eliminates some of the parameters involved in the reaction process, it, nevertheless, retains the enthalpy of reaction, which is the parameter of interest here. Its use is justified by our earlier work in which a comparison of this combustion model with the more complicated and computationally expensive Arrhenius kinetics model was presented [8,12]. Results indicated that when combustion is fast compared to the flow and, hence, the flame is thin and does not experience quenching, the infinite reaction rate model

[1] Post-doctoral associate, member, AIAA.
[2] Professor, Associate Fellow, AIAA.

the material line stretch. The latter is readily available due to the Lagrangian nature of the scheme.

In the second fractional integration step, diffusion effects are simulated using a core expansion scheme which mimics the diffusion process by expanding the element core size.

The severe distortion of the flowmap may lead to deterioration of the accuracy of the solution due to insufficient core overlap. In order to prevent this, but without sacrificing the efficiency of the calculation, elements are continuously inserted/removed in regions of high tensile/compressive strains, as assessed by the distance between neighboring elements. This insertion/removal is carried out according to local conservation laws.

IV. GEOMETRY AND BOUNDARY CONDITIONS

The shear layer evolves in a two-dimensional channel of height H and length X_{max}, between two parallel streams (1 for top and 2 for bottom) of different velocities which mix downstream of a thin splitter plate. Both streams are of the same density and temperature and each carries a single reactant. The top and bottom walls are modeled as rigid, slip, impermeable and adiabatic planes. At the downstream section, a condition of vanishing vorticity and SZ gradient is used as outflow boundary condition, and is applied by removing the elements which cross the $x=X_{max}$ plane. At the inlet section, the velocity and the λ profiles are assumed to be errorfunctions of equal thickness leading to Gaussian vorticity and λ gradient profiles of a common standard deviation, σ. In contrast, γ is assumed to be uniform and equal to unity there.

The errorfunction profile for λ implies that the profiles of the two reacting species are also errorfunctions. Profiles of this type are not unlike those experimentally observed downstream of the splitter plate. The same is true for the velocity profile. The unity value for the γ variable implies that temperature variation is only a consequence of the presence of combustion products. It should be evident that such an inlet condition coupled with the nature of the governing transport equation, eq. (5), and the rest of the boundary conditions described above, imply that γ is equal to unity throughout the domain at all times. This reduces the computational cost significantly.

These SZ variable profiles enable two sets of temperature and reacting species inlet profiles: (i) A non-reacting set where the temperature is uniform and no product exists and (ii) a reacting set where the flame extends all the way to the inlet and temperature and product profiles of the same thickness as that of the λ variable experience a maximum at the channel centerline. In this work, the second set is chosen due to the fact that it bypasses the ignition problem close to the inlet.

The channel height, H, is used as the length scale. σ is scaled in such a way that two wavelengths of the most unstable mode of the uniform density shear layer, obtained from linear stability analysis, fit within the channel height, i.e. $H=2 \times 12.8\sigma$. Under this condition, the channel is able to accommodate a paired eddy. The velocity field is scaled with the top stream velocity, U_1, whereas the density and temperature fields by the common to both streams values of these properties, ρ_o and T_o.

Initialization of the calculation is carried out by assuming that the inlet conditions persist throughout the domain. Hence, transport elements are distributed over nine flat material layers (lines) lying within the region of finite vorticity and λ-gradient defined by the above profiles. The elements are of square area of side h=0.0195. The value of the core radius is δ=0.0234, i.e. h/δ=0.833.

Finally, in some of the numerical simulations external forcing is implemented at the inlet. In the absence of forcing, the evolution of the layer reflects the amplification of numerically-excited instability waves, resulting in the "natural"-unforced layer behavior. The forcing signal consists of in-phase components of the most unstable mode of the uniform density layer and its subharmonic, both at an amplitude of 0.025. The interaction of the two forcing frequencies gives rise to eddies of disparate size depending on whether the two modes act constructively or destructively. This type of forcing is known to lead to eddy pairing in uniform density, non-reacting shear layers [13]. Implementation of the forcing is achieved by displacing elements at the inlet according to the forcing signal.

V. RESULTS AND DISCUSSION

V.1. Parameters

Numerical simulations were carried out for both forced and unforced reacting shear layers. The time step for all calculations was Δt=0.1 while the length of the domain was X_{max}=8 and 5 for the unforced and forced cases, respectively. A shorter domain was used for the forced case since the destabilization of the flow takes place closer to the inlet due to the external forcing.

For all cases, the inlet velocity ratio is $r=\frac{U_2}{U_1}=0.5$ and the Reynolds number (and Peclet number since Pe=Re) is Re = 12800. The corresponding Reynolds number based on the velocity difference across the layer, $\Delta U=U_1-U_2$, and the vorticity-layer original thickness, $d = 2\sigma$, is $Re_d = \frac{\Delta U\, d}{\nu} = 500$. The mass stoichiometry ratio is ϕ=1 and the non-dimensional enthalpy of reaction, referred to in this text as "heat release", is $Q_o = 6$.

To assess the dynamic effects of combustion-heat release, the reacting calculations were repeated but the density was kept constant and equal to its inlet value, in effect decoupling it from the temperature. Since, under the assumptions of our model, the variation in the density is the only means by which the reacting field can influence the flow, by keeping the density invariant the flow remains insensitive to the reaction. Furthermore, the fact that under the infinite reaction speed model the density has no direct effect on the reaction rate simplifies the assessment of the dynamic effects of heat release by distinguishing them from chemical effects. When this is not true, a more sophisticated approach in decoupling the flow and the reaction is necessary [8].

V.2 The Unforced Layer

V.2.1 Instantaneous Flowfield

Figures 1, 2 and 3 display an instantaneous comparison between the uniform and variable density unforced layers in terms of the vorticity, λ and the temperature, respectively. It should be noted that the apparent disappearance of the thin vorticity layer close to the inlet is not a result of the numerical simulation but of the resolution of the post-processing software.

The flow, in both cases, is dominated by large scale coherent vortical structures. Their formation is a result of the destabilization of the initially flat vorticity layer existing between the two fluid streams, via the amplification of the Kelvin-Helmholtz instability and the subsequent non-linear rollup of the layer around itself. Density variation resulting from the combustion heat release significantly modifies the flowfield and causes a decrease in the layer cross-stream growth. This appears to be a consequence of two effects: (i) a substantial delay in the onset of the flow instability, and (ii) an alteration of the evolution and interactions of the eddies.

In the uniform density case, the eddies contain only negative vorticity and appear to spin more vigorously. Their interactions are by pairings i.e. the amalgamation of eddies into a larger coherent structures initiated by the clockwise spiraling of these eddies around one another. In the variable density case, on the other hand, positive vorticity appears on the eddy outskirts and is progressively entrained into their cores. Pairings appear to be suppressed. Rather, the growth of the vortical structures is manifested by increases in the size of single eddies.
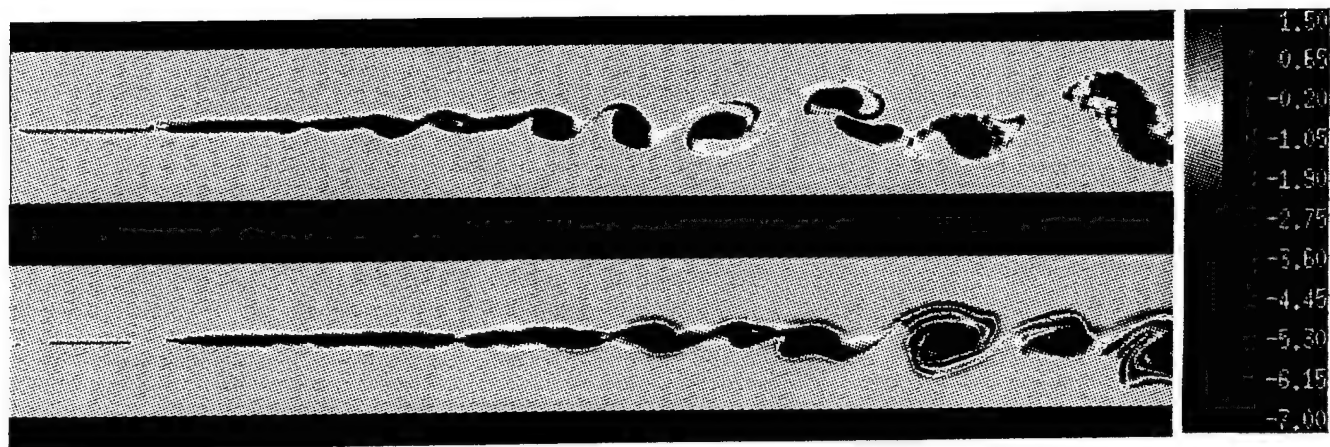
Figure 1. Vorticity fields of the uniform density (top) and variable density (bottom) unforced cases at t=13.
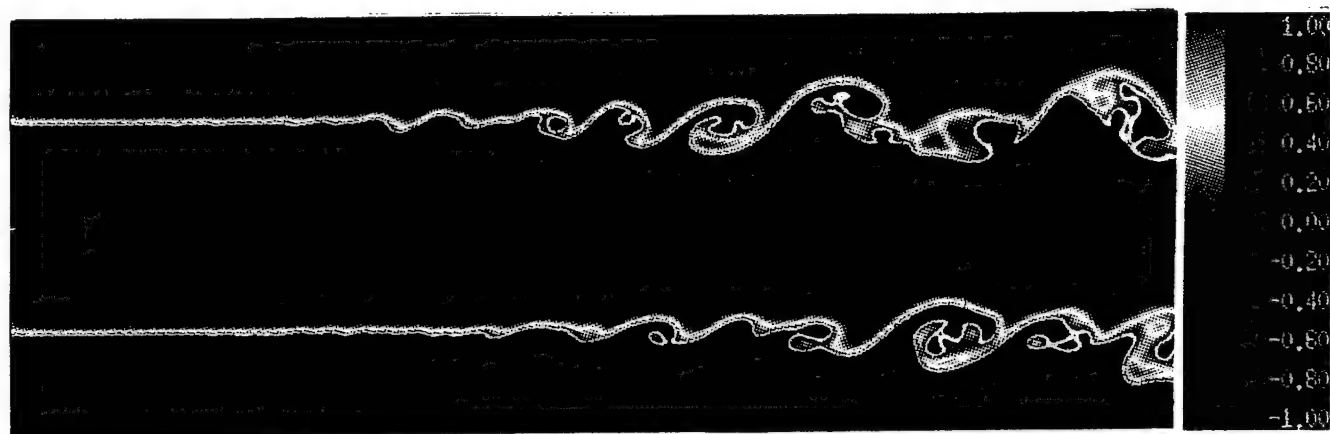

Figure 2. λ fields of the cases of figure 1. The white contour indicates the locus of the reaction interface ($\lambda=0$)
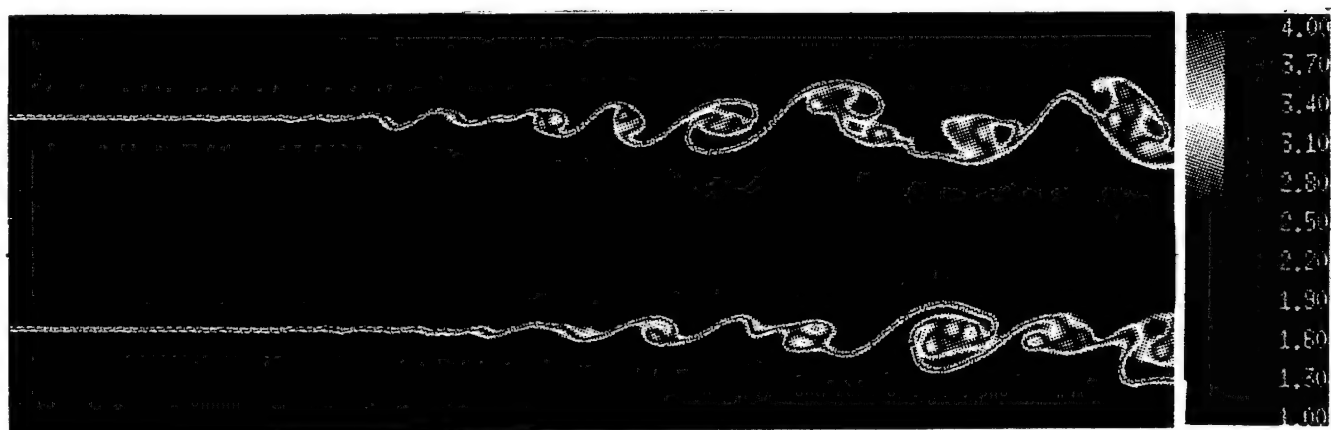

Figure 3. Temperature fields of the cases of figure 1

and is plotted versus the streamwise coordinate. Equation (16) indicates that the product thickness calculated here is representative of the mass of product at a given channel cross-section. Results are shown in figure 7.
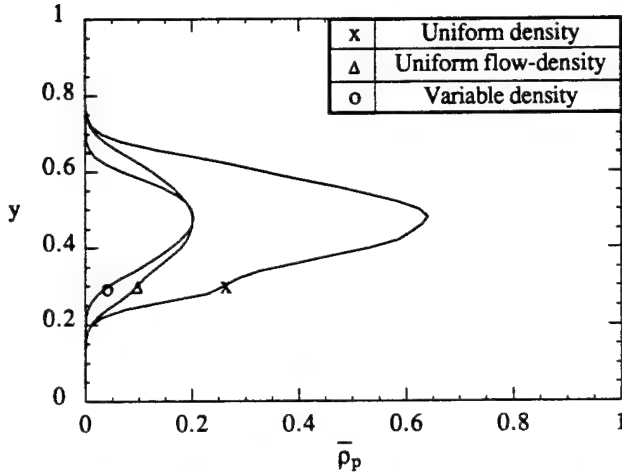

Figure 6. The time-averaged product density profiles of the uniform density, uniform flow-density and variable density unforced cases at x=5.
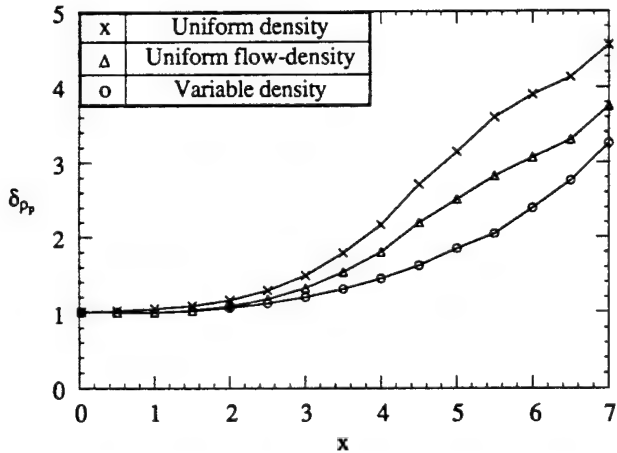

Figure 7. Product density thickness evolution with the streamwise coordinate for the uniform density, uniform flow-density and variable density, unforced cases.

As speculated earlier, the product thickness decreases throughout the flow domain for the variable density case. This is due to the drop of the density within the mixing region as well as the decrease in the size of the mixing region.

V.2.3 Fluctuating Flow

Modification of the instantaneous flow in the presence of heat release implies that the fluctuating nature of the flow is also altered. This is illustrated by considering the turbulent correlations resulting from averaging the equations of motion. In a variable density field this is preferably done using the Favre (density weighted) approach rather than the traditional Reynolds

approach. The main reason for this is the relative algebraic simplicity of the resulting averaged equations in the former case.

In Favre averaging, a quantity, ξ, is averaged according to:

$$\tilde{\xi} = \frac{\overline{\rho \xi}}{\overline{\xi}} , \qquad (17)$$

where the tilde indicates Favre averaging and the overbar, Reynolds averaging. The Favre fluctuating quantities, $\xi^{''}$, are, hence, defined as:

$$\xi^{''} = \xi - \tilde{\xi} , \qquad (18)$$

Favre averaging of the equations of motion for the flow considered here results in the following correlations of fluctuating quantities :

$$\overline{\rho \widetilde{u^{''} v^{''}}}, \quad \overline{\rho \widetilde{u^{''2}}} \quad \text{and} \quad \overline{\rho \widetilde{v^{''2}}} . \qquad (19)$$

As pointed out in Ref.[14] the first term, the turbulent stress term, represents the rate of transfer of momentum flux. The second and third terms are indicative of the flow turbulent kinetic energy per unit volume in the streamwise and cross stream directions, respectively, and are representative of the turbulence intensity. The total flow turbulent kinetic energy is:

$$KE = \frac{\overline{\rho \widetilde{u^{''2}}} + \overline{\rho \widetilde{v^{''2}}}}{2} . \qquad (20)$$

As noted earlier, due to heat release, the density decreases significantly and this results in reduced Favre turbulent quantities. This does not necessarily imply that the fluctuations are diminished. To clarify this point, in what follows the uniform flow-density case, is provided for comparison. Since this latter case has the same flowfield as the uniform-density case then the corresponding Reynold's turbulent quantities are identical. Thus, any difference in the Favre turbulent quantities between the two cases can only be a consequence of the variable density and will thus provide an indication of the extent of its effect on the variable density case.
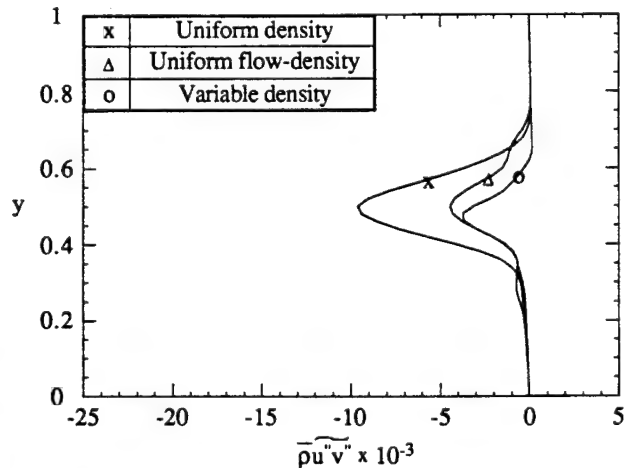

Figure 8. The Favre-averaged turbulent stress profiles of the uniform density, uniform flow-density and variable density unforced cases at x=5.
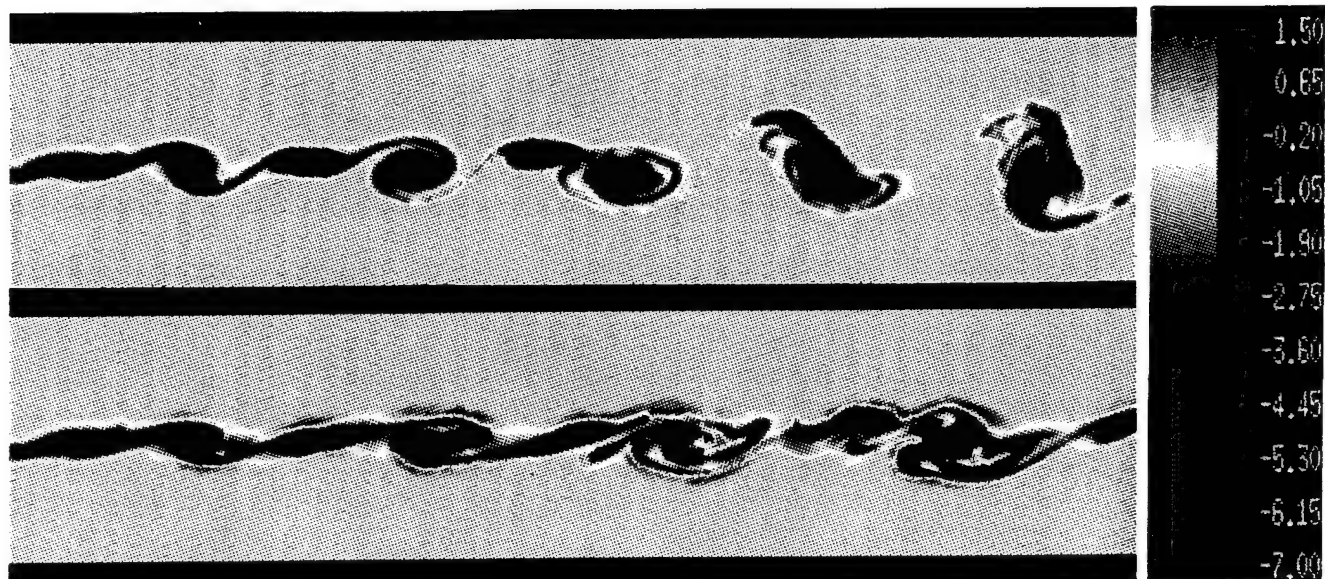
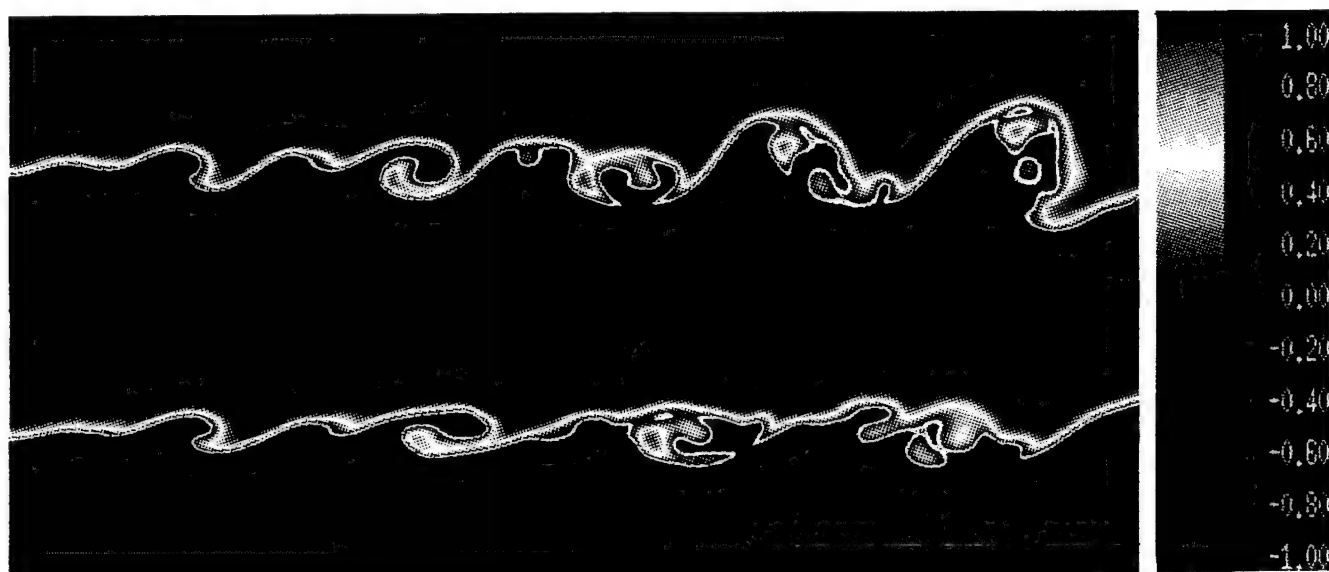Figure 10. Vorticity fields of the uniform density (top) and variable density (bottom) forced cases at t=10.

Figure 11. λ fields of the cases of figure 10. The white contour indicates the locus of the reaction interface (λ=0)
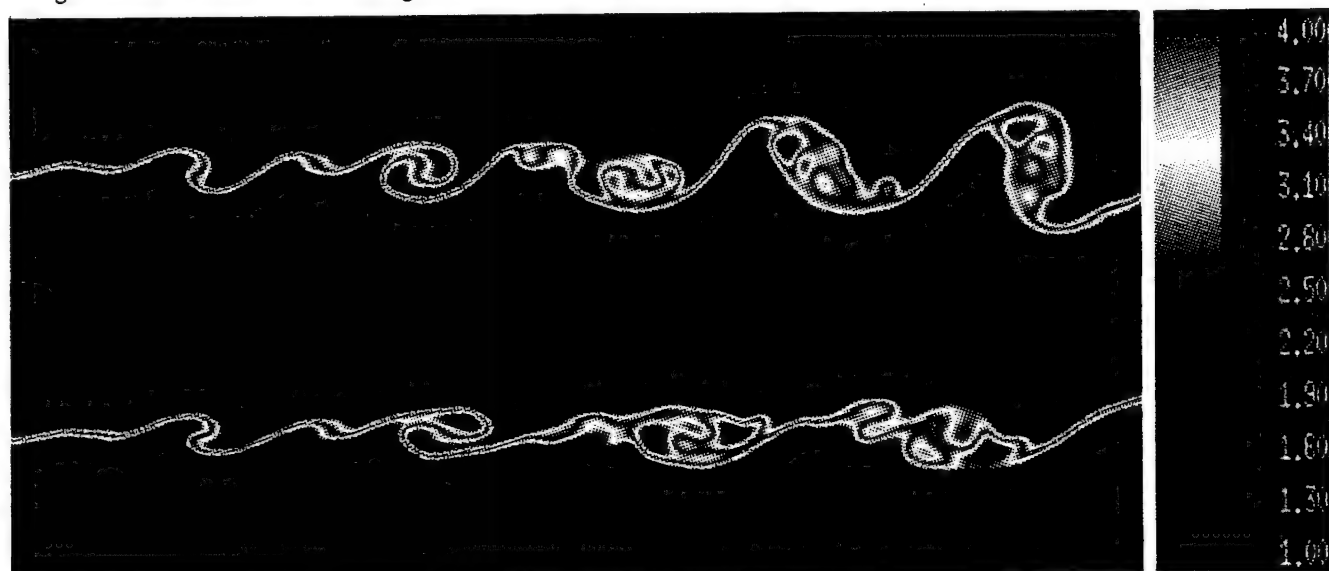

Figure 12. Temperature fields of the cases of figure 10.

down in the presence of density variation for most of the domain despite the forcing which bypasses the instability suppression seen in the unforced flow. The drop is much more significant in the region where interactions of the vortical structures take place. Thus, the modification of these interactions as well as the properties of the resulting larger structures represent the most important mechanisms by which heat release decreases the forced shear layer cross-stream growth.
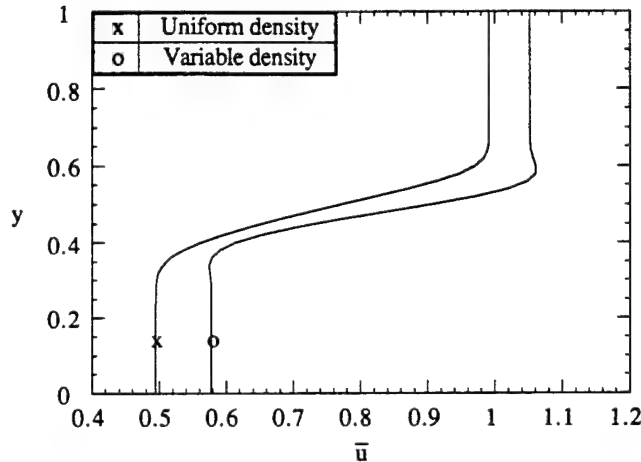
occupies a larger area. The main result of this should be that the significant drop in the mixing region thickness seen above is not as damaging to the rates of combustion.

Figure 13. The time-averaged velocity profiles of the uniform and variable density, forced cases at x=2.5.
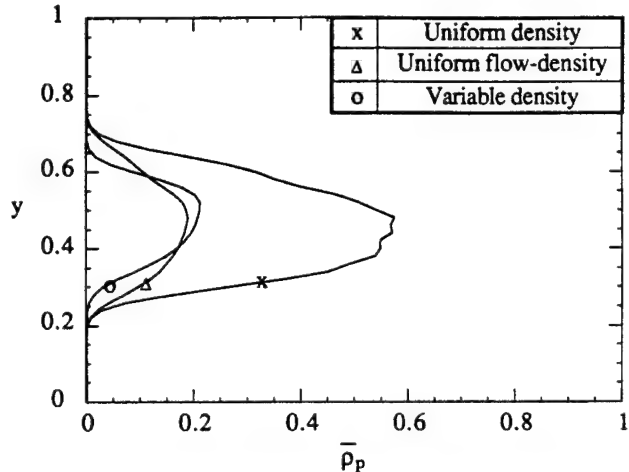
Figure 15. The time-averaged product density profiles of the uniform density, uniform flow-density and variable density forced cases at x=2.5.
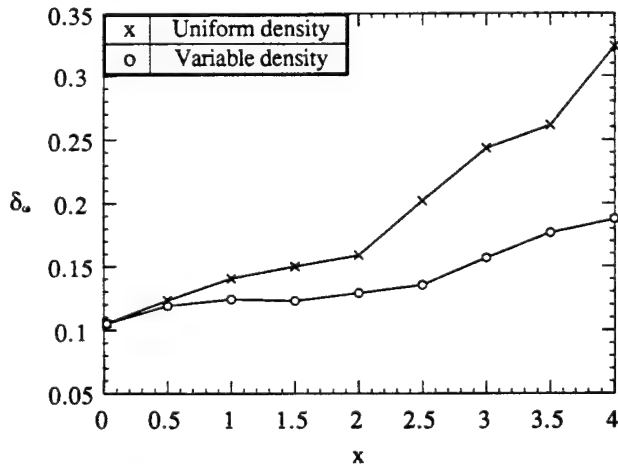

Figure 14. Vorticity thickness evolution with the streamwise coordinate for the uniform and variable density, forced cases.
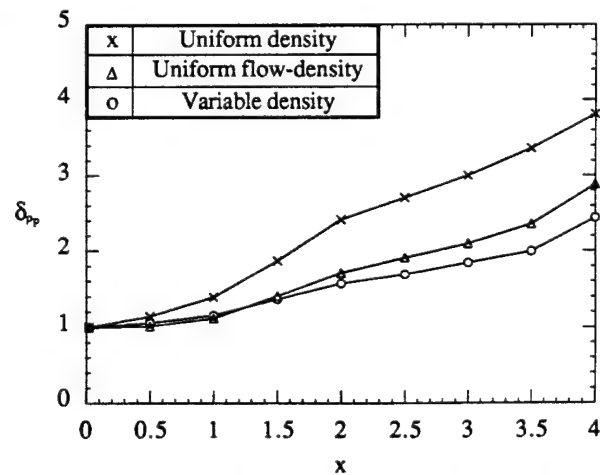
Figure 16. Product density thickness evolution with the streamwise coordinate for the uniform density, uniform flow-density and variable density, forced cases.

In figure 15, the product density profiles of the uniform and variable density cases together with the uniform flow-density case are presented. Again, the similarity between these and the product density profiles of the unforced flow is significant. The uniform flow-density case experiences a smaller peak than the variable density case indicating that even though the mixing region is smaller for this case, combustion is more efficient. This is because of the earlier observation that the instantaneous mixing region, while smaller in width, actually

This statement is quantified in figure 16 where the product thickness is plotted versus the streamwise coordinate. The figure clearly indicates that heat release decreases the mass of product formed throughout the flow domain but that most of this effect is associated with the decrease in the density rather than the alteration of the mixing. In agreement with earlier speculation, the drop is not as substantial as the drop in the vorticity thickness would suggest.

V.3.3 Fluctuating Flow
The fluctuating features of the flow are now illustrated by the Favre averaged turbulent stress, figure 17, and kinetic

the termination of reaction due to unavailability of reactants which results from an overaccumulation of products, can and does take place.) These processes are certainly valid at the initial stages of the flow (before eddy formation) and at the braids. As the layer rolls into eddies, the ability of the flow to enhance burning is also dependent on the relative concentrations of reactants which are reduced due to the accumulation of products. During the early stages of the rollup the availability of reactants is practically unimpaired (through entrainment of reactants from the free streams), and the accumulation of products is small. Thus, in this region, the increases in product formation can also be related to the straining of the reaction interface. Further downstream, however, where the eddies mature and start interacting, accumulation of products and the reduction of reactants concentrations in the eddy cores are more prominent. Thus, stretching of the reaction interface in this region does not necessarily result in significant increases in the amount of products formed.

Hence, the above discussion provides the explanation why the reduction in the convolution of the reaction interface in the variable density case results in a decrease in the product thickness.

VI. CONCLUSIONS

Results of numerical simulations of both forced and unforced two dimensional spatially-developing, high Reynolds number, non-premixed reacting shear-layers indicate that combustion heat release reduces the efficiency of mixing and, hence, of burning. Moreover it lowers the intensity of turbulence and accelerates the flow in the streamwise direction.

In the absence of external forcing, the mixing region is reduced for most of the domain via a delay in the onset of the flow instability, a reduction of the overall spinning of the eddies and an apparent suppression of their downstream interactions.

When external forcing is applied, the reduction in mixing is mainly due to the reduced spinning of the eddies which keeps their major axes aligned with the flow direction, and the alteration of the eddy interaction mechanism from pairing to tearing of smaller eddies by their larger neighbors.

The streamwise flow acceleration is mainly attributed to the volumetric (area) expansion related to the changes in density. This expansion, which results to a thicker shear region close to the inlet, is responsible for the delay in the onset of the flow instability of the unforced case. Volumetric expansion also weakens the vorticity. This leads to the reduction of the spinning of the eddies of both forced and unforced flows and the alignment of the major axis of the downstream larger eddy with the flow direction in the forced case. On the other hand, the resistance to pairing seen in both cases is attributed to baroclinic vorticity generation. This mechanism is responsible for the formation of positive vorticity on the outer perimeter of the large eddies, whose vorticity is predominantly negative. The positive vorticity inhibits the clockwise rotation involved in the eddy pairing interaction and it also leads to diminished entrainment from the free streams.

REFERENCES

1. Hermanson, J.C. and Dimotakis, P.E., "Effects of Heat Release in a Turbulent, Reacting Shear Layer", *Journal of Fluid Mechanics*, Vol. 199, 1989, pp. 333-375.

2. Keller, J.O., "An Experimental Study of Combustion and the Effects of Large Heat Release on a Two Dimensional Turbulent Mixing Layer" Ph.D. Thesis, University of California, Berkeley CA, 1982.

3. Mungal, M.G. and Dimotakis, P.E., "Mixing and Combustion With Low Heat Release in a Turbulent Shear Layer" *Journal of Fluid Mechanics*, Vol. 148, 1984, pp. 349-382.

4. McMurtry, P.A., Jou, W.H., Riley, J.J. and Metcalfe, R.W., "Direct Numerical Simulations of a Reacting Mixing Layer With Chemical Heat Release", *AIAA Journal*, Vol. 24, 1986, pp. 962-970.

5. McMurtry, P.A., Riley, J.J. and Metcalfe, R.W., "Effects of Heat Release on the Large-Scale Structure in Turbulent Mixing Layers", *Journal of Fluid Mechanics*, Vol. 199, 1989, pp. 297-332.

6. Ghoniem, A.F. and Krishnan, A., "Origin and Manifestation of Flow-Combustion Interactions in a Premixed Shear Layer", *22nd Symposium (International) on Combustion*, The Combustion Institute, Pittsburgh PA, 1988, pp. 665-675.

7. Givi, P. and Jou, W.H., "Direct Numerical Simulations of a Two-Dimensional, Reacting, Spatially Developing, Mixing Layer by a Spectral Element Method", *22nd Symposium (International) on Combustion*, The Combustion Institute, Pittsburgh PA, 1988, pp. 635-643.

8. Soteriou, M.C., "Numerical Study of Turbulent Combustion in a Shear Layer", Ph.D. Thesis, Massachusetts Institute of Technology, Cambridge MA, 1993

9. Ghoniem, A.F. and Givi, P., "Lagrangian Simulation of a Reacting Mixing Layer at Low Heat Release", *AIAA Journal*, Vol. 26, 1988, pp. 690-697.

10. Ghoniem, A.F. and Heidarinejad, G., "Effect of Two-Dimensional Shear Layer Dynamics on Mixing and Combustion at Low Heat Release", *Combustion Science and Technology*, Vol. 72, 1990, pp. 79-99.

11. Grinstein, F.F. and Kailasanath, K., "Chemical Energy Release and Dynamics of Transitional, Reactive Shear Flows", *Physics of Fluids*, Vol. 4, 1992, pp. 2207-2221.

12. Soteriou, M.C. and Ghoniem, A.F., "Vortex-Transport Element Simulation of the Exothermically Reacting Spatially Developing Layer", presented at the 2nd U.S. National Congress On Computational Mechanics", Washington D.C., 1993

13. Ghoniem, A.F. and Ng, K.K., "Numerical Study of the Dynamics of a Forced Shear Layer", *Physics of Fluids*, Vol. 30, 1987, pp. 706-721.

14. Libby, P.A. and Williams, F.A., "Fundamental Aspects", *Turbulent Reacting Flows*, Libby, P.A. and Williams, F.A. eds., Springer-Verlage, Berlin, 1980, pp.1-43.

16. Soteriou, M.C. and Ghoniem, A.F., "The Vorticity Dynamics Of An Exothermic, Spatially-Developing, Forced, Reacting Shear Layer", submitted for presentation at the 25th Symposium (International) on Combustion, 1994

APPENDIX III

THE VORTICITY DYNAMICS OF AN EXOTHERMIC, SPATIALLY-DEVELOPING, FORCED, REACTING SHEAR-LAYER

Marios C. Soteriou and Ahmed F. Ghoniem
Department of Mechanical Engineering
Massachusetts Institute of Technology
Cambridge, MA 02139, USA

ABSTRACT

The effects of combustion exothermicity on the vorticity dynamics of a low-Mach number, forced, spatially-developing, high Reynolds number, reacting-shear layer are investigated using the results of a two-dimensional numerical simulation. The chemical reaction is modeled by single-step, irreversible, Arrhenius kinetics with high Damkohler number, moderate Karlovitz number and significant heat release. The numerical solution is obtained using the Lagrangian transport-element method. Results indicate that a fast exothermic reaction, with the concomitant density variation, modifies the shape, size, speed and orientation of the large-scale vortical structures and their downstream interactions, leading to an overall reduction of the cross-stream growth of the mixing region. These changes are traced to the two primary mechanisms by which density variation due to heat release modifies vorticity: volumetric expansion and baroclinic generation. It is shown that the weakening of the vorticity due to volumetric expansion diminishes the cross-stream mixing zone by aligning the eddy major axis with the flow direction. Baroclinic vorticity generation, on the other hand, is responsible for the formation of a band of positive vorticity on the outer perimeter of the large eddies, whose vorticity is predominantly negative, which inhibits entrainment and alters the eddy interaction mechanism from pairing of adjacent eddies to tearing of smaller eddies by their larger neighbors. Both mechanisms contribute to the acceleration of the eddies in the streamwise direction.

INTRODUCTION

Post-transitional, exothermic, reacting-shear layers are encountered in many combustion systems. The flow, which arises due to the intrinsic instability of the shear region between two reacting streams originally moving at different velocities is endowed with mechanisms which enhance mixing and combustion rates. Experimental studies [1,2] indicate that the essentially two-dimensional vortical structures, or eddies, which characterize the early stages of the non-reacting flow persist in its reacting counterpart despite the significant effects of combustion exothermicity. Moreover, most of the products are found within these structures exemplifying their importance to the combustion process and motivating further studies into their properties. The latter are essentially controlled by vorticity dynamics.

The effects of combustion exothermicity on a post-transitional shear layer have been the subject of several studies. Experimental investigations [1,3,4] indicate that heat release reduces the shear-layer growth and diminishes the rates of mixing and combustion. Numerical studies, mostly restricted to the idealized temporally-evolving flow, have been carried out for both non-premixed [5-6] and premixed [7] layers and have, to some extend, been able to reproduce this behavior. However, due to the idealized nature of the temporal model, conclusions drawn from these studies must be treated with caution, e.g., it is well known that asymmetric entrainment can not be reproduced by this model [8-12]. Moreover, the non-premixed calculations [5,6] were limited to a temperature-independent (zero activation energy) reaction rate and a low Damkohler number.

On the other hand, numerical studies of spatially-evolving layers have been restricted to cases where the effects of combustion on the flowfield are negligibly small [e.g., 13,14]. An exception is presented in Ref.[15] where a large-scale simulation of a compressible shear layer with variable transport properties and Arrhenius kinetics was performed. However, combustion heat release was kept low and the effect of the activation temperature was diminished by raising the background temperature. Nevertheless, a useful

2

conclusion which can be drawn from that work is that the effects of the temperature-dependent transport properties play a weak role in the dynamics.

In this paper the vorticity dynamics of a forced, spatially-developing, exothermic shear layer are investigated while allowing for temperature-dependent Arrhenius kinetics and significant exothermicity. Results are obtained using the two-dimensional transport-element simulations. The numerical scheme makes it possible to use higher activation energy and Damkohler number than previously attempted. The effects of combustion exothermicity on the vorticity dynamics are analyzed in terms of the contributions of the two major mechanisms of vorticity modification i.e. volumetric expansion and baroclinic vorticity generation.

THE GOVERNING EQUATIONS

A two-dimensional reacting shear flow in which gravitational effects are negligible and compressibility effects are limited to the low Mach number regime [5] is considered. We assume that all species behave as perfect gases with equal molecular masses and equal and constant mass diffusivities and specific heats. The momentum and thermal diffusivities are also constant and the Lewis number is equal to unity. Combustion occurs according to a single-step, irreversible, mole-preserving Arrhenius reaction i.e. $\phi^* \eta_1 + \eta_2 \rightarrow (1+\phi^*) \eta_p$ where η_i denotes species, i = 1, 2 for the reacting species and i = p for the product, and ϕ^* is the molar stoichiometric ratio.

We use the Helmholtz decomposition to recast the equations into their vorticity-streamfunction-velocity potential form, and Shvab-Zeldovich (SZ) variables to simplify the scalar-transport equations. The equations of the SZ variables are then transformed into SZ-gradient equations. Since combustion occurs at a finite rate, and thus the SZ variable solutions alone cannot yield the complete reacting field, one reacting variable is solved for in primitive form. The resulting equations, in non-dimensional form, are:

$$\nabla^2 \phi_e = -\frac{1}{\rho}\frac{d\rho}{dt}, \qquad \nabla^2 \psi = -\omega, \quad \text{and} \quad \nabla^2 \phi_p = 0 \qquad (1a,b,c)$$

$$\frac{d\omega\widehat{k}}{dt} = -(\nabla \cdot \mathbf{u})\omega\widehat{k} + \frac{\nabla\rho \times \nabla p}{\rho^2} + \frac{1}{Re}\nabla^2 \omega\widehat{k} \qquad (2)$$

$$\frac{d\mathbf{g}}{dt} = -\mathbf{g}\cdot\nabla\mathbf{u} - \mathbf{g}\times(\omega\widehat{k}) + \frac{1}{Pe}\nabla^2 \mathbf{g} \qquad (3)$$

$$\frac{dY_p}{dt} = \frac{1}{Pe}\nabla^2 Y_p + (1+\phi)\frac{\dot{w}}{\rho} \qquad (4)$$

The velocity vector, $\mathbf{u}=(u,v)$, is reconstructed as $\mathbf{u} = \nabla\phi_e + \nabla\phi_p + \nabla\times(\psi\widehat{k})$. To dimensionalize, we use the initial thickness of the vorticity layer, d, the velocity difference between the two streams, ΔU, and the initial temperature and density, T_o and ρ_o, respectively. $\mathbf{x} = (x,y)$ is a right-handed Cartesian coordinate system, t is time,

4

$\nabla = \left(\dfrac{\partial}{\partial x}, \dfrac{\partial}{\partial y} \right)$ and $\dfrac{d}{dt} = \dfrac{\partial}{\partial t} + \mathbf{u} \cdot \nabla$. ϕ_e is the expansion velocity potential, ϕ_p is the velocity potential related to the boundary conditions, ψ is the streamfunction, $\omega = \nabla \times \mathbf{u}$ is the vorticity, where $\hat{k}$ is the unit vector normal to the plane of motion, p is the pressure, ρ is the density which is related to the temperature, T, via $\rho T = 1$. The Reynolds and Peclet numbers are $Re = \dfrac{\Delta U \, d}{\nu}$ and $Pe = \dfrac{\Delta U \, d}{\alpha}$, respectively, where ν is the kinematic viscosity and α is the thermal diffusivity. $\mathbf{g} = \nabla \beta$ is the gradient of the SZ-variable, $\beta = \lambda$ or γ where $\lambda = Y_1 - \phi Y_2$ and $\gamma = T - \dfrac{Q_o \phi}{1+\phi} Y_p$. Y_i is the mass-fraction of species i with $Y_1 + Y_2 + Y_p = 1$, ϕ is the mass stoichiometric ratio, $\phi = \phi^* \dfrac{M_1}{M_2}$, M_i being the molar mass of species i, $Q_o = \dfrac{\Delta h_f}{c_p T_o}$ is the normalized enthalpy of reaction with c_p being the mixture specific heat, $\dot{w} = A_f \rho^2 \, Y_1 \, Y_2 \exp(- \dfrac{T_a}{T})$ is the reaction rate where $A_f = \dfrac{\tilde{A}_f \rho_o d}{\Delta U}$ is the frequency factor and $T_a = \dfrac{E_a}{R T_o}$ is the activation temperature, where E_a and R are the activation energy and the universal gas constant, respectively.

NUMERICAL SOLUTION

We use the transport-element method to perform the numerical simulation (for detail, see Ref.[12].) In this Lagrangian, grid-free scheme, the vorticity, volumetric expansion, SZ-gradients and product mass fraction are discretized among a large number of elements of finite area and overlapping Gaussian cores. The vortical and expansion contributions to the velocity are computed using convolutions over the fields of vortex and expansion elements, respectively. The SZ-variables are obtained from the corresponding discrete gradient fields via a similar convolution. The contribution of the boundary conditions is obtained using conformal mapping and the method of images.

The evolution of the flow and scalar fields is obtained by integrating the governing equations, written for each element, in two fractional steps. In the first step, which includes all processes except diffusion, the elements are advected with the local velocity vector and the relevant source terms are integrated, e.g., the circulation of an element is modified by the baroclinic term according to the cross product of the material acceleration and the density gradient. The SZ-gradient equation is substantially simplified using kinematical relations between the gradient and the stretch of the associated material line. The integration of the product-mass fraction equation, carefully performed to eliminate conventional sources of numerical errors, modifies the local concentrations according to the reaction source term. In the second fractional step, diffusion effects are incorporated via a novel implementation of the core expansion scheme in which after each core expansion the strength of the elements is recomputed using the original core size [12].

The severe distortion of the flowmap, which could lead to insufficient core overlap and deterioration of the numerical accuracy is accommodated by continuously inserting/removing elements in regions of high tensile/compressive strains, as assessed by the distance between neighboring elements. This insertion/removal of elements is carried out while satisfying local conservation laws.

GEOMETRY AND BOUNDARY CONDITIONS

The shear layer evolves downstream of a thin plate in a two-dimensional channel of height H, and length $X_{max} = 5H$, between two parallel streams of unequal velocities but same temperature and density (T_o, ρ_o), each stream carrying a single reactant. The top and bottom walls are modeled as rigid, slip, impermeable and adiabatic planes. At the exit, a condition of vanishing gradient is imposed by deleting the elements as they cross the boundary. At the inlet section, (1) errorfunction profiles with equal thicknesses are assumed for u and λ, rendering the ω and $\nabla\lambda$ profiles Gaussians, with a standard deviation σ, (2) γ is taken to be unity, (3) a finite amount of product is introduced, in the form of a Gaussian profile with a standard deviation, σ, and a peak value of 0.4 to enforce ignition. The scaling of σ, where $d=2\sigma$, with H is such that two wavelengths of the most unstable mode of the uniform-density shear layer fit within the channel height.

The calculations are initialized by assuming that the inlet conditions persist throughout the domain. Square elements of side $h=0.0195H$ are distributed over nine horizontal material layers lying within the support of the discretized quantities. The core radius is such that $\frac{\delta}{h} = 1.2$.

External forcing is implemented at the inlet by displacing the elements in the cross-stream direction. The forcing signal consists of in-phase components of the most unstable mode of the uniform-density layer and its subharmonic, both at an amplitude $A_f = A_s = 0.32d$. This forcing, which promotes rollup and pairing in the uniform density flow [16], results in the formation of two eddies of unequal size per cycle. A large eddy, referred to in this text as the L-eddy, forms when the two components of the signal act constructively and a small eddy, the S-eddy, when they act destructively (see figure 1).

7

RESULTS AND DISCUSSION

Parameters

The following parameters are used. The inlet velocity ratio is $r = 0.5$, $Re = 500$, $T_a = 10$, $A_f = 100$, $\phi = 1$ and $Q_0 = 6$, corresponding to Damkohler number, $Da = \frac{\tau_{dif}}{\tau_{che}} = 1026$, where $\tau_{dif} = \frac{d^2}{\alpha}$ is the diffusion time scale and $\tau_{che} = \frac{T_f}{A_f}\exp(\frac{T_a}{T_f})$ the chemical reaction time scale, and Karlovitz number, $Ka = \frac{\tau_{che}}{\tau_{flw}} = 0.49$, where $\tau_{flw} = \frac{d}{\Delta U}$ is the flow time scale. The vorticity dynamics of the reacting layer are investigated by (1) comparing the results of constant-density (CD) and variable-density (VD) simulations, (2) analyzing the distributions of the vorticity modification terms, and (3) comparing results of simulations in which one of the vorticity modification mechanisms is removed. Under the assumptions of our model, the effects of the exothermic energy are confined to density variation.

The flowfield

Figure 1 displays a comparison between the CD and the VD layers, both depicted in terms of the vortex elements and their velocity vectors measured with respect to the inlet mean velocity. In agreement with experimental observations, the flow in both cases is dominated by large-scale vortical structures which form due to the destabilization of the initial vorticity layer via the amplification of the Kelvin-Helmholtz instability, the rollup of the fundamental eddies, and their interactions due to the subharmonic instability. The figure shows that density variation modifies the evolution and interactions of the vortical structures leading to an overall reduction of the cross-stream growth.

In the VD case, the vortical structures accelerate in the streamwise direction. At the initial stage, the fundamental eddies are larger, primarily in the mean flow direction, i.e., they are less rounded. In the latter stages, the pairing-merging of fundamental eddies into larger, coherent and rounded structures observed in the CD case is impaired and replaced by tearing of the S-eddy between its two neighboring L-eddies. This results in subharmonic structures which are less rounded and, in contrast to the CD case, tend to

8

keep their major axis aligned with the streamwise direction. As a result, the layer cross-stream growth is significantly inhibited.

The Temperature Field

Since the effect of combustion on the flow is felt solely through the density field, one should be able to explain the various phenomena described above by reviewing the density, or temperature, field and the mechanisms by which this field influences the flow. Figure 2 presents instantaneous, 2D maps of the temperature, which in the case of the VD flow is equivalent to inverse density, while in the CD case, is artificially decoupled from the flow, for the two cases of figure 1. It is clear that the region of temperature variation is the same as the region where vortical structures exist. This is because these structures control the mixing of the two reactants and hence, are where combustion takes place. The plot also provides a clear indication that significant phenomena occur at scales smaller than those of the vortical structures. Density variation is more closely related to the rollup of the material layer initially positioned between the two reactants, which for $\phi = 1$, coincides with the vorticity layer. The density experiences a minimum in the vicinity of this layer confirming that this is where most burning occurs. Thus, analysis of the flow and reaction fields can best be accomplished by investigating the dynamics of the vorticity layer.

Vorticity Dynamics, Preliminaries

The combustion-related density field can influence the dynamics in several ways. Mass conservation implies that density decrease causes volumetric expansion which, since the flow is semi-confined, causes a streamwise acceleration. The vorticity equation indicates that in a 2D, VD field, the vorticity of a fluid element is modified by three mechanisms. Volumetric expansion, $-(\nabla.\mathbf{u})\omega$, baroclinic generation, $\dfrac{\nabla\rho \times \nabla p}{\rho^2}$, and viscous diffusion, $\dfrac{1}{Re}\nabla^2\omega$. In an exothermic field, $\nabla \cdot \mathbf{u}$ is generally positive and volumetric expansion reduces the element vorticity while preserving its circulation; the

9

decrease of the vorticity is equal and opposite to the increase in area, without changes in sign.

Baroclinic vorticity generation arises from the misalignment of the pressure and density gradients and is capable of producing vorticity of both signs. Since the pressure gradient is mainly a manifestation of the fluid acceleration, vorticity is formed as neighboring elements experience differential accelerations due to their different density. Because of its directional nature, baroclinic vorticity generation is strongly linked to the geometry of the flow map.

Viscous diffusion acts to smooth out vorticity variations. However, when the Reynolds number is high, viscous diffusion plays a minor role.

Vorticity Distribution

Figure 3 presents the vorticity distribution of the two cases shown in figure 1, with blue and red indicating positive and negative vorticity, respectively. The most striking difference between the two cases is the presence of positive vorticity, in the VD case, on the outer rims of the vortical structures whose vorticity is, primarily, of a negative sign. Most of the negative vorticity has its origin in the incoming flow. Since only the baroclinic torque is capable of producing vorticity of both signs, the positive vorticity must be a manifestation of this mechanism.

Baroclinic Vorticity Generation

Figure 4 (top) shows the baroclinic vorticity production term at the same time step as before, with red and blue indicating positive and negative rates. The complexity of this figure can be unraveled by considering the action in the neighborhood on a single eddy during rollup. This is done in figure 5 where schematic diagrams of the geometric evolution of the layer are drawn, and the corresponding baroclinic term is estimated by considering the cross product of the density gradient and the fluid acceleration.

During rollup, the layer acquires a "Z" configuration. Throughout this process, fluid from the braids is accelerated in the streamwise direction towards the evolving

10

structure. This acceleration changes its direction as one crosses the stagnation point, defined in the frame of reference moving with the eddy, between the neighboring structures. The density field is such that the density gradient is approximately normal to the layer, changing sign across it, while the local stretch ensures that the magnitude of the gradient stays large. Thus, in the braids, the enhanced density gradient and the fluid acceleration are mutually normal and the contribution of the baroclinic term is maximum. The arrangement of the vectors involved creates positive and negative vorticity on the upper and lower sides of the braid on the left-hand side of the eddy, respectively, while the opposite occurs on the right-hand side.

Closer to the center of the structure, which in the moving reference frame is also a stagnation point, the acceleration on both sides reverses sign and so does the generated vorticity. The baroclinic term becomes weaker as the fluid acceleration is increasingly dominated by rotation and the density gradient zone thickens. As rollup continues, a region of negative vorticity is established inside the eddy core, surrounded by a band of strong positive vorticity on the outside, particularly on the upper left and lower right sides, as shown in figures 4 and 5. Adding an overall negative vorticity to this picture would result in the vorticity field shown in figure 3.

This rearrangement of the vorticity has significant implications. For example, positive vorticity around the eddies decreases the entrainment of irrotational fluid into the large structures, since it weakens the field created by the original negative vorticity. Furthermore, it may upset the eddy interaction mechanism which is responsible for pairing in the CD flow. This vorticity, as will be shown in detail later, also induces a streamwise velocity on the eddies.

Divergence

The effect of the expansion term on the vorticity field can be inferred from the vorticity plots. Figure 3b shows that the vorticity occupies more area and that the negative vorticity is weaker than in the CD case. To highlight the zone where volumetric expansion

11

has the strongest effect on the vorticity, we plot in figure 4 (bottom) the distribution of the $-(\nabla.u)\omega$ term, i.e. the rate of vorticity change due to divergence. Since divergence is essentially due to the Lagrangian change in density, this zone can also be considered as where the flame is located. In this regard, the figure indicates that most of the burning occurs within the braids, which is expected since D_a is high while K_a is moderate. Evidently, the expansion in the braids weakens the vorticity there and through the roll-up leads to the formation of less vigorous eddies.

Separating the Mechanisms

The above discussion indicates that the approach of analyzing the effect of the different mechanisms of vorticity modification using simulations which involve all the terms in the governing equation has the following limitations: (1) it is not obvious how the two mechanisms interact, and (2) it is not clear whether the changes in the evolution of individual eddies, e.g., acceleration, or the shift of the eddy interaction mechanism from pairing to tearing is a result of expansion, baroclinicity, or both. To overcome these limitations, the calculation for the VD case was repeated twice, but at each time, one of the two mechanisms of vorticity modification was eliminated in an attempt to distinguish between the phenomena attributable to each mechanism. These simulations are labeled baroclinicity-only and expansion-only simulations.

Figure 6 displays the results of these calculations. The figure shows that the suppression of pairing and the onset of tearing are due to the baroclinic generation, while the alignment of the major axis of the structure with the streamwise direction is due to volumetric expansion. In the expansion-only simulation, figure 6 (bottom), pairing occurs in a way similar to that found in the CD flow. In this case, the vorticity layer thickens due to volumetric expansion, and rollup is slowed down due to the weakened vorticity.

In the baroclinicity-only case, figure 6 (top), on the other hand, the S-eddies are torn between their neighboring L-eddies, similar to the VD case. Positive vorticity surrounding the vortical structures inhibits the spiraling of the fundamental eddies around a

common center. This allows enough time for the larger L-eddies to gain fluid at the expense of the S-eddies. The above argument implies, as shown before [17] that in the absence of external forcing, baroclinic vorticity generation suppresses eddy interaction.

Comparisons between the fundamental eddies of the CD and baroclinicity-only case indicate that these eddies are smaller and more elliptical in the latter, i.e., baroclinicity is responsible for reducing entrainment, as mentioned earlier. Figure 6 also reveals that the acceleration of the vortical structures in the streamwise direction is not only due to volumetric expansion but also due to baroclinicity. This has been observed before in the study of the non-reacting VD flow [18]. This acceleration is due to the redistribution of the vorticity inside the structures and the loss of eddy symmetry which arises from the unequal tearing of the S-eddy towards its neighboring L-eddies.

Finally, the number of elements used to discretize the evolving material layers indicates that baroclinic vorticity generation increases the eddy-induced strain while volumetric expansion reduces it.

CONCLUSIONS

Combustion exothermicity modifies the evolution and interactions of the vortical structures in a spatially-developing shear layer. It flattens the eddies and complicates their vorticity distribution, increases their speed, alters their interaction mechanism from pairing to tearing, and keeps their major axis aligned with the flow direction. Consequently the size of the mixing region is reduced.

The alteration of the eddy shape is a consequence of the baroclinic torque which significantly complicates the eddy vorticity field and reduces entrainment. Vorticity generation is also responsible for the modification of the eddy interaction mechanism. The alignment of the eddy major axis with the streamwise direction is a manifestation of the weakening vorticity field due to volumetric expansion. The acceleration of the eddies is a combined effect of both mechanisms; volumetric expansion because of confinement and baroclinic generation because it induces vorticity asymmetry within each individual eddy.

At the initial stages, baroclinic generation reduces the eddy size by suppressing entrainment while volumetric expansion weakens the existing vorticity. Further downstream, where eddy interactions take place, both mechanisms act to decrease the mixing region; baroclinic generation by resisting pairing and volumetric expansion by aligning the eddy major axis with the flow direction. For forced shear layers this latter effect is by far the more significant.

14

REFERENCES

1. Hermanson, J.C. and Dimotakis, P.E., *Journal of Fluid Mechanics*, 199: 333, (1989).

2. Brown, G.L. and Roshko, A.J., *Journal of Fluid Mechanics*, 64: 775 (1974).

3. Keller, J.O., Ph.D. Thesis, University of California, Berkeley CA, 1982.

4. Mungal, M.G. and Dimotakis, P.E., *Journal of Fluid Mechanics*, 148: 349 (1984).

5. McMurtry, P.A., Jou, W.H., Riley, J.J. and Metcalfe, R.W., *AIAA Journal*, 24: 962 (1986).

6. McMurtry, P.A., Riley, J.J. and Metcalfe, R.W. *Journal of Fluid Mechanics*, 199: 297 (1989).

7. Ghoniem, A.F. and Krishnan, A., *22nd Symposium (International) on Combustion*, The Combustion Institute, Pittsburgh PA, pp. 665 (1988).

8. Grinstein, F.F, Oran E.S. and Boris, J.P., *Journal of Fluid Mechanics*, 165: 201 (1986).

9. Givi, P. and Jou, W.H., *22nd Symposium (International) on Combustion*, The Combustion Institute, Pittsburgh PA, pp. 635 (1988).

10 Sandham, N.D. and Reynolds, W.C., *Journal of Fluid Mechanics*, 224: 133 (1974).

11. Givi, P., Prog. Energy Combust. Sci., 15, 1 (1989).

12. Soteriou, M.C., Ph.D. Thesis, Massachusetts Institute of Technology, Cambridge MA, 1993

13. Ghoniem, A.F. and Givi, P., *AIAA Journal*, 26: 690 (1988).

14. Ghoniem, A.F. and Heidarinejad, G., *Combustion Science and Technology*, 72: 79 (1990).

15. Grinstein, F.F and Kailasanath, K., *Physics of Fluids*, 4: 2207, (1992).

16. Ghoniem, A.F. and Ng, K.K., *Physics of Fluids*, 30: 706 (1987).

17. Soteriou, M.C. and Ghoniem A.F., AIAA Paper 94-0777

18. Soteriou, M.C., Knio, O.M. and Ghoniem A.F., AIAA Paper 91-0081

FIGURE CAPTIONS

Figure 1. The flowfield in the uniform-density, top, and variable-density, bottom, cases at $t = 64$, depicted using the vortex elements and their velocity vectors measured with respect to the mean flow. The top/bottom number of elements is 5389/4034. L and S denote examples the fundamental eddies which form during the first and second halves of the subharmonic forcing function. Arrows indicate the location of eddies formed at the same time.

Figure 2. The temperature fields of the uniform-density, top, and the variable-density case, bottom, at $t = 64$. The blue to red color bar describes the temperature scale $1 \leq T \leq 3.75$.

Figure 3. The vorticity distribution in the uniform-density, top, and variable-density case, bottom, at $t = 64$. The blue to red color bar describes the vorticity scale $-1.095 \leq \omega \leq 0.235$.

Figure 4. The distributions of the rates of vorticity modification by baroclinic generation, top, and volumetric expansion, bottom, at $t = 64$. The blue to red color bar describes the vorticity-rate scale $-0.02 \leq \dot{\omega} \leq 0.02$

Figure 5. Schematic illustration of the process of baroclinic vorticity generation. ω_o is the initial vorticity and $\dot{\omega}_b$ the vorticity generation rate. $\nabla \rho$ is the density gradient and $\mathbf{a}$ the material acceleration.

Figure 6. The baroclinicity-only, top, and expansion-only, bottom, cases at $t = 64$ shown in terms of the vortex elements and their relative velocity. The top/bottom number of elements is 9232/3818. Arrows indicate the location of eddies formed at the same time. The lines on the left/right sides of the arrows correspond to the locations of the same eddies in the uniform/variable density cases, shown in figure 1.
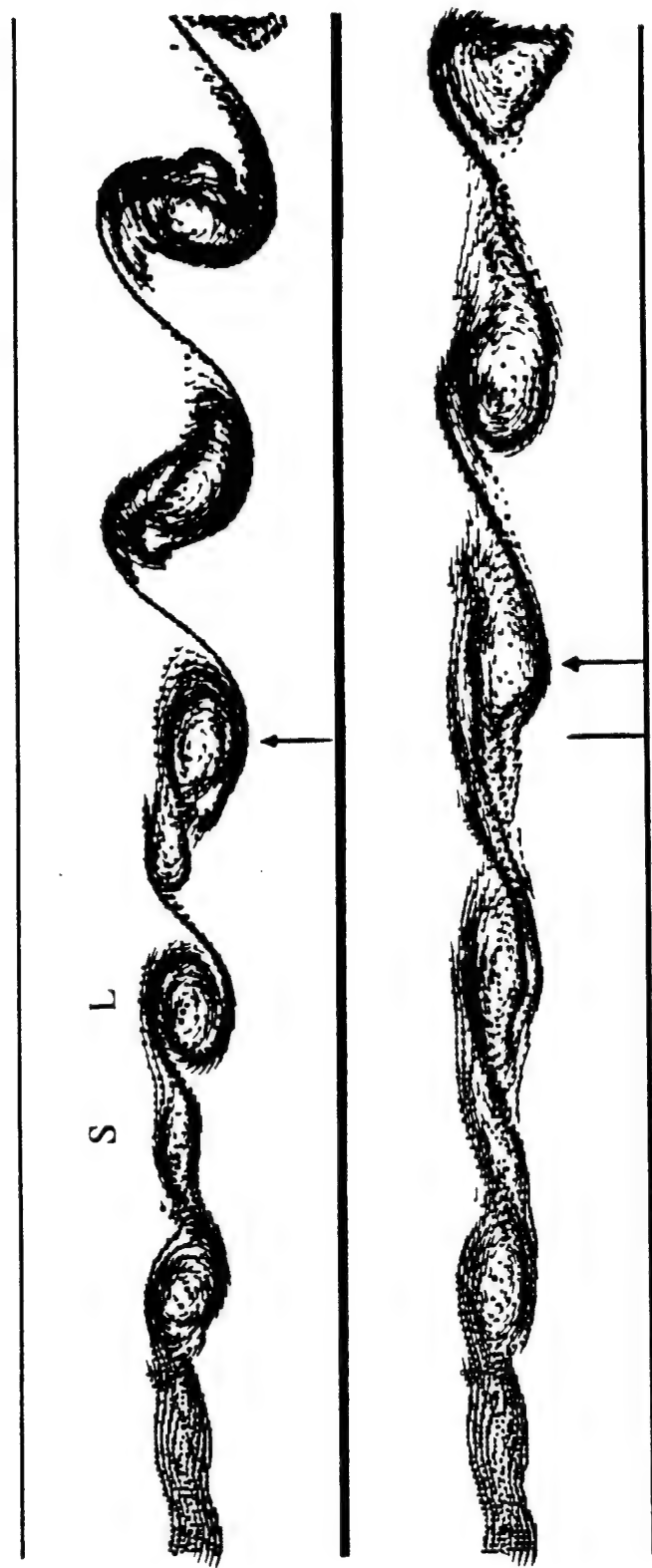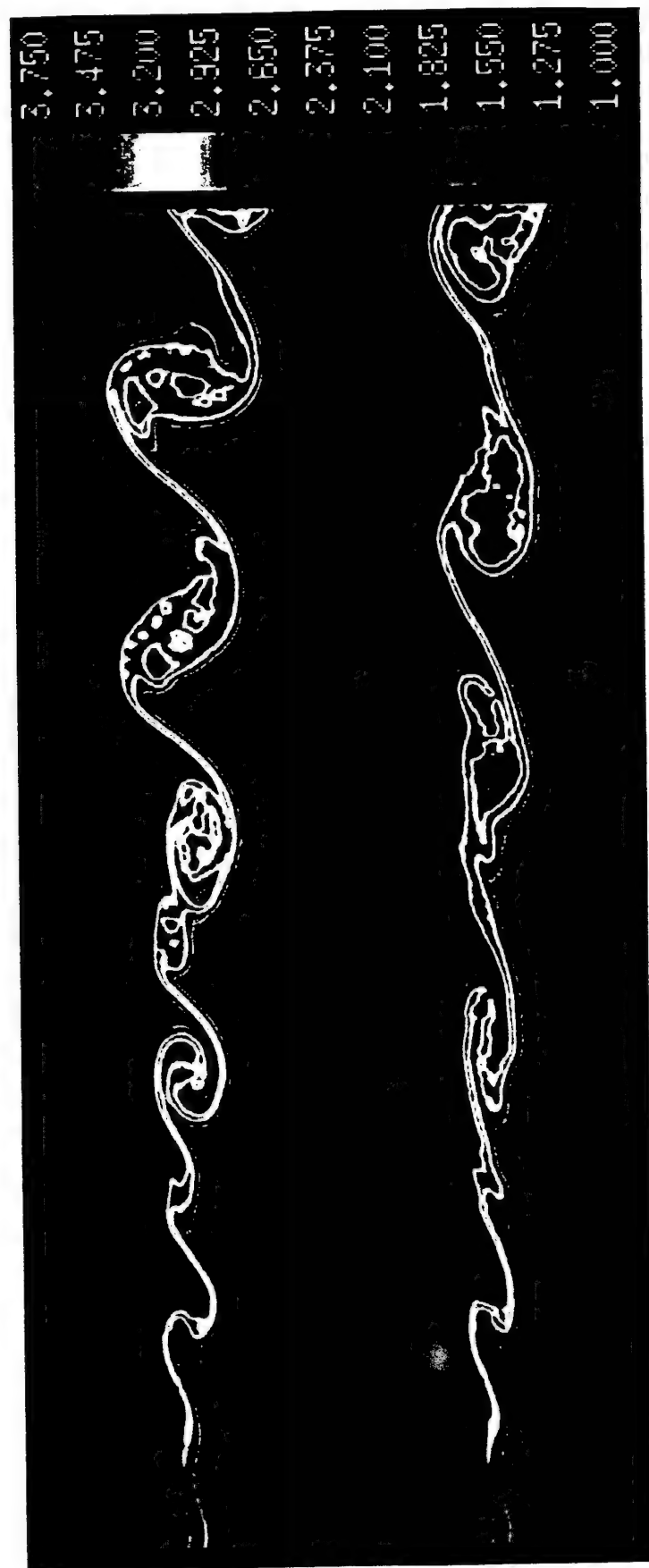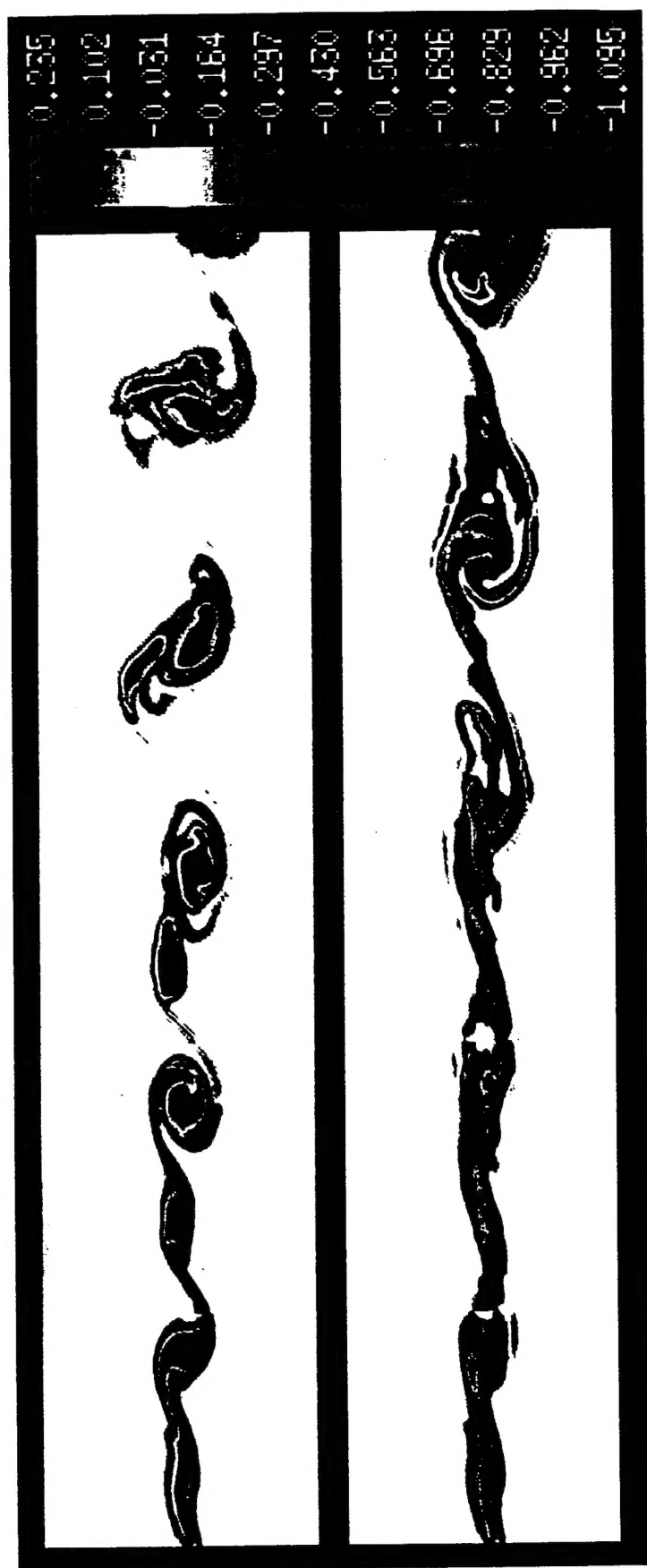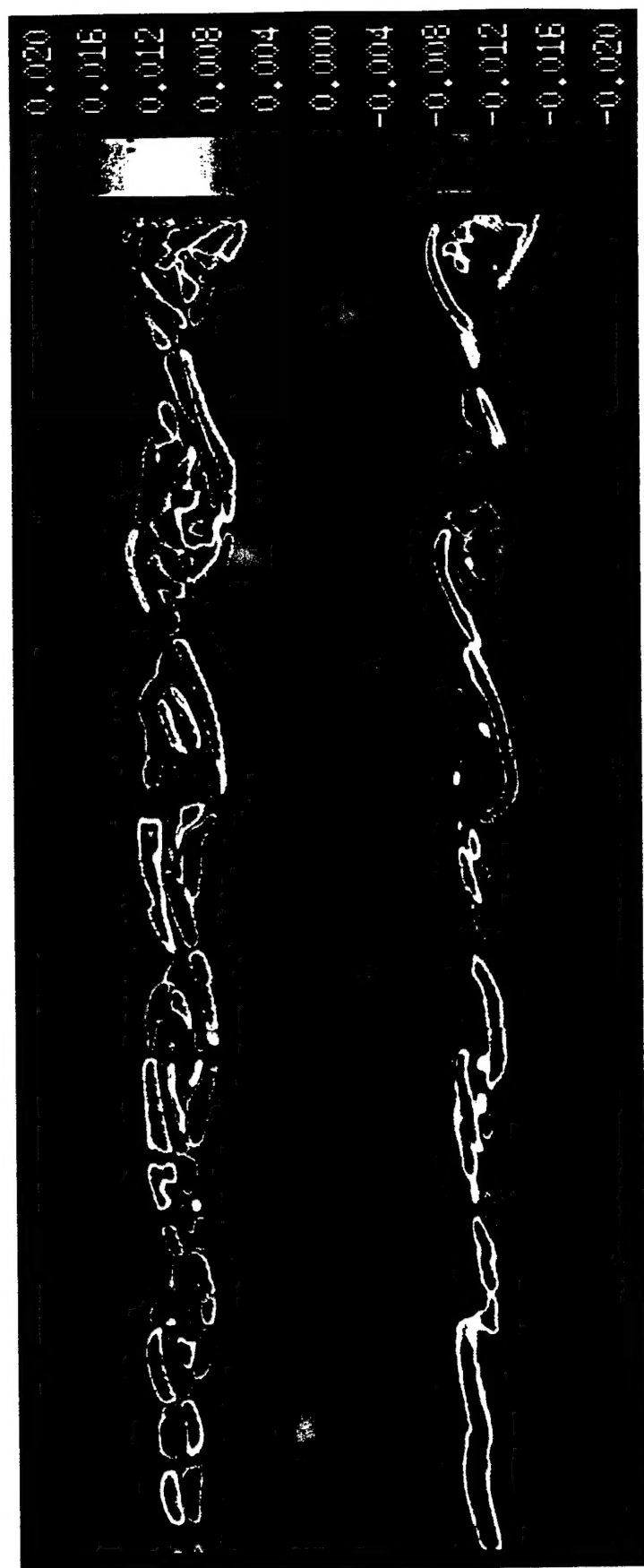
17

FIGURE 1

FIGURE 2

FIGURE 3

FIGURE 4

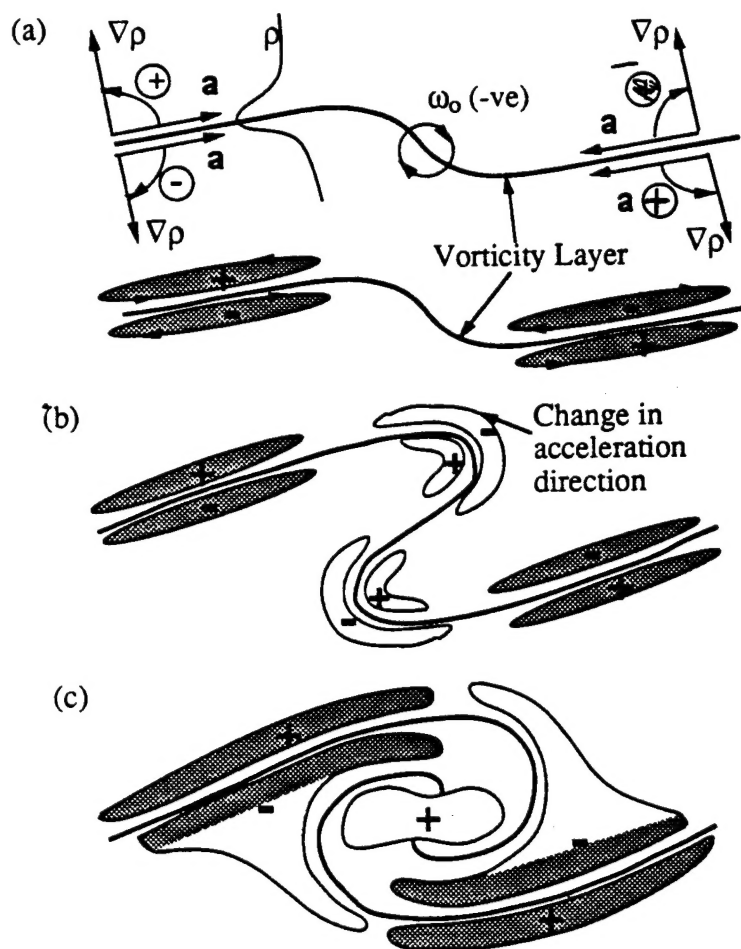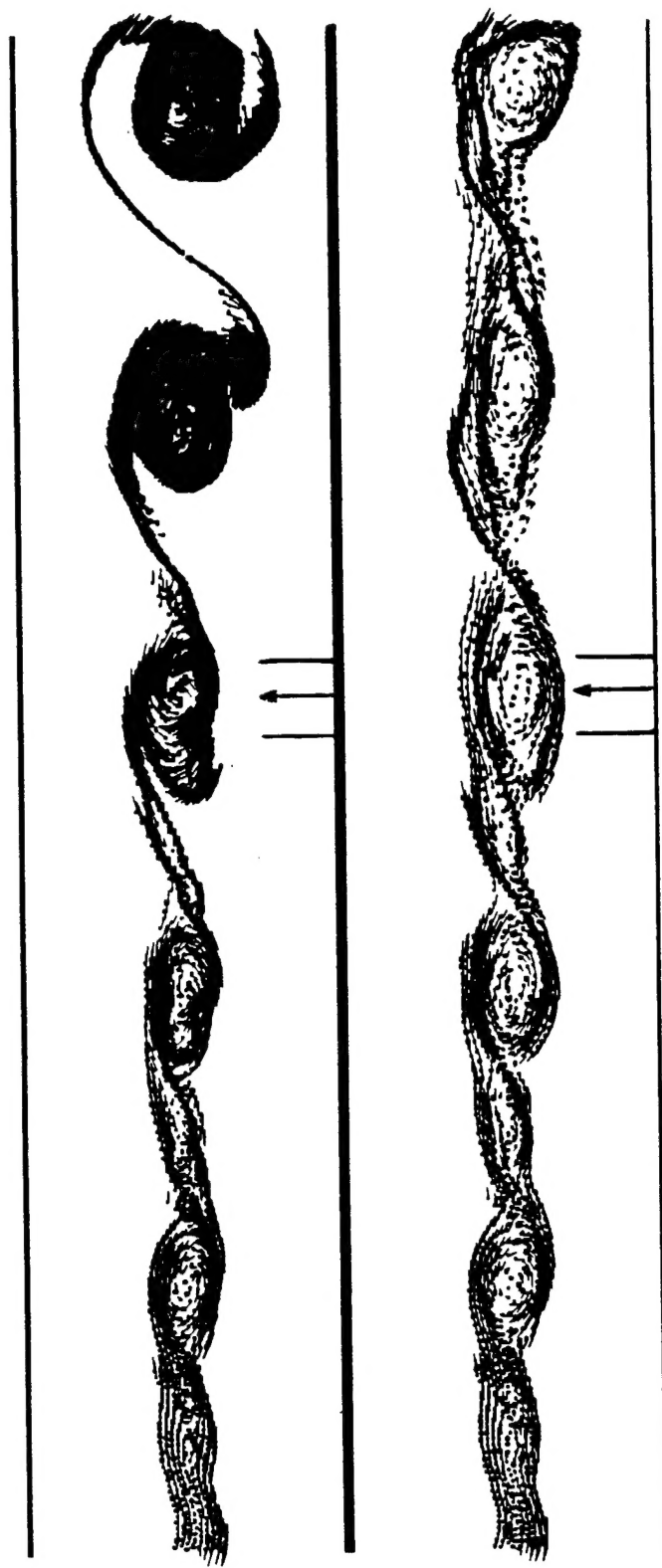$$\dot{\omega}_b = \mathbf{a} \times \frac{\nabla \rho}{\rho}$$

(a)

$\nabla \rho$ ρ

$\oplus$ **a**

ω_o (-ve)

a

$\ominus$

$\nabla \rho$

$\nabla \rho$

$\ominus$

a

a $\oplus$

$\nabla \rho$

Vorticity Layer

(b)

Change in
acceleration
direction

(c)

FIGURE 5

FIGURE 6